

Non-local, local, and extraction spin valves based on ferromagnetic metal/GaAs hybrid structures

Dissertation

zur Erlangung des akademischen Grades

doctor rerum naturalium (Dr. rer. nat.)

im Fach Physik

eingereicht an der

Mathematisch-Naturwissenschaftlichen Fakultät

der Humboldt-Universität zu Berlin

von

Dipl.-Phys. Yori Manzke

Präsident der Humboldt-Universität zu Berlin

Prof. Dr. Jan-Hendrik Olbertz

Dekan der Mathematisch-Naturwissenschaftlichen Fakultät

Prof. Dr. Elmar Kulke

Gutachter/innen:

1. Prof. Dr. Henning Riechert
2. Prof. Dr. Gernot Güntherodt
3. Prof. Dr. Saskia F. Fischer

Tag der mündlichen Prüfung: 3. Juni 2015

Abstract

The efficient electrical generation of a spin accumulation inside a semiconductor (SC) utilizing the interface with a ferromagnetic metal (FM) is essential for the realization of many spintronic device concepts, in which the spin of the electron is exploited in addition to its charge for computational and memory purposes. At FM/*n*-type SC hybrid contacts, the application of a reverse bias leads to the injection of spin-polarized electrons into the SC. Alternatively, an applied forward bias can be used to generate a spin accumulation of opposite sign due to the extraction of electrons with a particular spin orientation. In this work, the electrical generation and detection of a spin accumulation is studied using epitaxial and laterally structured ferromagnetic metal/*n*-type GaAs hybrid systems in various measurement geometries. To achieve a high spin generation efficiency, the spin-independent electrical properties of the contact have to be considered in addition to the choice of the injector material with respect to its degree of spin polarization. Here, it is shown that the current-voltage characteristics can even constitute the dominating design parameter with respect to the spin injection properties. In addition, a novel device concept is presented and studied experimentally. This approach essentially relies on spin extraction as the spin generation process in a local spin valve geometry. In contrast to local spin valves based on spin injection, the presented extraction spin valve can be regarded as a building block of an extended device comprising multiple extraction events along the lateral spin transport channel. It is shown how such multiple extraction spin valves allow for an intriguing functionality, which can be used, for example, for the read-out of data in magnetic memory applications.

Keywords: spintronics, III-V semiconductors, magnetism, spin valves, extraction spin valve

Zusammenfassung

Im Gebiet der Spin-Elektronik wird der Spin des Elektrons zusätzlich zu seiner Ladung für Bauelementkonzepte ausgenutzt. Hierbei ist die effiziente elektrische Erzeugung einer Spinakkumulation in einem halbleitenden Material von großer Bedeutung. Die Erzeugung der Spinakkumulation kann mithilfe eines ferromagnetischen Metall-Kontaktes erfolgen. Wird eine elektrische Spannung an die Grenzfläche zwischen dem ferromagnetischen Metall und dem Halbleiter so angelegt, dass spinpolarisierte Elektronen vom Metall in den Halbleiter fließen, spricht man von elektrischer Spininjektion. Bei einer Umkehrung der Spannung werden bevorzugt Elektronen der entgegengesetzten Spinorientierung aus dem halbleitenden Material entfernt. Dieser Prozess wird als Spinextraktion bezeichnet. In dieser Arbeit wird die elektrische Erzeugung einer Spinakkumulation in lateral strukturierten, epitaktischen Hybridstrukturen bestehend aus ferromagnetischen Metallkontakten auf n -dotiertem GaAs untersucht. Allgemein ist neben der Spinpolarisation im Ferromagneten auch die spinunabhängige elektrische Charakteristik eines Kontaktes von zentraler Bedeutung für die effiziente Spinerzeugung. Hier wird gezeigt, dass die gewöhnlichen Strom-Spannungs-Kennlinien die Spininjektionseigenschaften dominieren können. Außerdem wird ein neuartiges Bauelementkonzept vorgestellt und experimentell untersucht. Hierbei handelt es sich um ein lokales Spin-Ventil, welches Spinextraktion statt Spininjektion als Spinerzeugungsprozess verwendet. Im Gegensatz zum gewöhnlichen lokalen Spin-Ventil kann ein solches Extraktions-Spin-Ventil als Baustein eines erweiterten Bauelements angesehen werden, welches auf mehreren, aufeinanderfolgenden Extraktionsprozessen beruht. Die Eigenschaften des Extraktions-Spin-Ventils werden diskutiert und es wird gezeigt, wie seine Funktionalität beispielsweise für das Auslesen der Daten in magnetischen Speichern angewendet werden kann.

Schlagwörter: Spintronik, III-V-Halbleiter, Magnetismus, Spin-Ventile, Extraktions-Spin-Ventil

Contents

1	Introduction	1
2	Background	5
2.1	Electrical spin injection and extraction	5
2.2	Spin transport	9
2.2.1	Spin relaxation in n -type GaAs	9
2.2.2	Hanle effect	11
2.3	Electrical detection of a spin accumulation	12
2.3.1	Three-terminal spin detection	12
2.3.2	Non-local spin valve	16
2.3.3	Local spin valve	18
2.3.4	Extraction spin valve	21
3	Experimental	23
3.1	Sample preparation	23
3.1.1	Sample growth	23
3.1.2	Sample processing	25
3.2	Experimental setup for spin transport measurements	27
4	Electrical spin generation in ferromagnet/n-GaAs hybrid structures	29
4.1	Introduction	30
4.2	Experimental	31
4.3	Ferromagnetic metal/ n -GaAs contacts	33
4.3.1	Potential distribution below the contact	33
4.3.2	Current-voltage characteristics	35

Contents

4.4	Non-local spin valve	40
4.4.1	Non-local detection of a spin accumulation	40
4.4.2	Hanle curves	44
4.4.3	Bias dependence of electrical spin generation	46
4.4.4	Influence of contact area	51
4.5	Detection of a spin accumulation in the three-terminal geometry . .	53
4.6	Local spin valve	60
4.7	Discussion	65
4.8	Outlook	67
5	Extraction spin valves	69
5.1	Introduction	70
5.2	Experimental	71
5.3	Extraction spin valve	72
5.4	Double extraction spin valve	78
5.5	Spin transport model	85
5.5.1	Generalized form for multiple ferromagnetic contacts	85
5.5.2	Three ferromagnetic contacts (double extraction spin valve)	87
5.6	Application examples	87
5.6.1	Multiple extraction spin valves as spin polarizers	87
5.6.2	Multiple spin extraction for magneto-logic gates	89
5.6.3	Multiple extraction spin valves for memory read-out	91
5.7	Outlook	91
6	Conclusions and outlook	95
	Bibliography	99
	List of figures	117
	List of tables	121

CHAPTER 1

Introduction

The rapid advancement in information technology in the last half of the 20th and the beginning of the 21st century is frequently described with what is referred to as Moore's law,¹ which according to Gordon E. Moore "has come to refer to almost anything related to the semiconductor industry that when plotted on semi-log paper approximates a straight line."² In essence, Moore's law relates to the observation that technological key figures, such as the integration density or the performance of electronic components in integrated circuits, increase exponentially at a given rate (e.g., a doubling of the economically viable transistor density on a microchip every two years). The accompanying enhancement of the computing power is driven by technological innovation. For example, the advances in lithography have stimulated a decrease of typical feature sizes (like the gate length of a transistor) from a few micrometers³ in the 1970s to less than 20 nm today.⁴ However, it is frequently argued that the downscaling of the metal oxide semiconductor field-effect transistor (MOSFET), which has been at the heart of the development strategy of the semiconductor industry for more than 30 years, has already reached its physical limitations.³ Limits to transistor scaling are set by current leakage as a consequence of quantum mechanical tunneling and the capability to remove the Joule heat generated by an increased power density.⁵

Because the strategy of shrinkage cannot be pursued indefinitely, novel ap-

Chapter 1 Introduction

proaches are investigated, which focus on new geometries⁶ or an increase in functionality to maintain the rate of progress in computational devices. A promising route to increase the functionality of electronic components is the use of the electron spin in addition to its charge. The corresponding field of research is called spintronics and has already led to remarkable progress in storage technology. The observation that the electrical resistance of all-metallic ferromagnetic/non-magnetic/ferromagnetic stacks depends sensitively on the relative magnetization orientation of the ferromagnetic layers^{7,8} in 1988 (the giant magnetoresistance effect for which A. Fert and P. Grünberg were awarded the Nobel Prize in Physics⁹ in 2007) and the subsequent research conducted by S. Parkin^{10,11} resulted in the rapid implementation of the technology in commercially available storage media as read heads of magnetic hard disk drives. In addition, the efficient control of charge transport by the magnetization directions in magnetic tunnel junctions^{12,13} with a thin tunnel barrier as the non-magnetic spacer material between two ferromagnetic metals has led to another class of non-volatile memory referred to as magnetoresistive random access memory.¹⁴

While the commercial potential of spintronics has been demonstrated for the above-mentioned all-metallic systems, dedicated research is still necessary to pave the way for the introduction of semiconductor-based spintronic devices into broad-scale commercial applications. The promising prospects of the utilization of the spin degree of freedom in semiconductor technology become apparent from the useful properties of semiconducting materials like the control of the charge density using dopants or gate voltages. In addition, semiconductors exhibiting a direct band gap are particularly interesting for spin-based optoelectronic applications. In a proposed spin-based transistor^{15,16} – essentially a metal-oxide-semiconductor field-effect transistor (MOSFET) with ferromagnetic contacts – the on and off states are controlled by changing the spin orientation of a spin-polarized current flowing between the ferromagnetic source and drain contacts. The reversal of the spin direction is achieved via spin-orbit effects induced by the application of an electrical voltage to the gate terminal. The manipulation of the transistor current without a change of the amount of charge in the semiconducting channel opens the potential for a more energy-efficient operation as compared to a conventional charge-based MOSFET.

Key challenges of all-electrical, semiconductor-based spintronic devices are the generation of a spin-polarized current, its transport, manipulation, and detection. Scientific advances have been made including the successful spin injection into various semiconducting materials.¹⁷⁻²⁰ However, it has been pointed out that a high efficiency of electrical spin generation and detection is essential to achieve an acceptable on/off current ratio in a spin-based transistor.²¹

Among the semiconducting materials, GaAs constitutes a particularly interesting candidate for spin-based research and applications due to its long spin lifetime (more than 100 ns at low temperatures²²), which corresponds to a spin transport length on the micrometer scale,²³ exceeding the channel length of modern transistors by several orders of magnitude. Furthermore, due to its direct band gap, GaAs is most suitable for optical spin detection schemes²⁴⁻²⁸ as well as spin-based optoelectronic applications.^{29,30}

The results presented in this thesis focus on the electrical generation, transport, and detection of a non-equilibrium spin density in lateral spin transport structures based on GaAs and epitaxial contacts with ferromagnetic metals. In chapter 2, the basic understanding of electrical spin generation and detection in semiconducting materials is reviewed. In particular, the different measurement geometries employed in this thesis are explained. The sample fabrication method by molecular beam epitaxy and lithography techniques as well as the measurement setup employed for spin transport experiments are described in chapter 3.

In chapter 4, the results of the investigation of the electrical spin generation, transport, and detection using different ferromagnetic metals deposited on *n*-type GaAs are presented. For this study, the non-local, the three-terminal, and the local geometries are used to gain an improved understanding of the spin generation process. It is shown that the current-voltage characteristics of the ferromagnet/semiconductor contacts have a strong influence on the spin signal in all geometries. The implications of these results regarding the engineering strategy for highly efficient spin injector contacts are discussed.

A novel device concept is proposed and experimentally demonstrated in chapter 5. In this approach, spin-polarized currents are generated by spin extraction at one ferromagnetic contact and locally detected at a subsequent ferromagnetic contact. The working principle of such an extraction spin valve is studied in vari-

Chapter 1 Introduction

ous field-dependent measurements. Furthermore, it is shown that the underlying principle of operation can be regarded as a building block of an extended device, which is based on multiple spin extraction and detection events.

Finally, in chapter 6, the results are briefly summarized, and an outlook for future investigations is given.

CHAPTER 2

Background

In this chapter, information is presented with regard to the scientific background of the experimental results described in chapters 4 and 5. Essentially, aspects are compiled from the literature, which are helpful for the understanding of the following chapters. The succession of sections follows the generic sequence of phenomena, which have to be considered when designing all-electrical spin transport experiments or spintronic devices: the generation of a spin accumulation, spin transport, and the detection of a spin accumulation.³¹

2.1 Electrical spin injection and extraction

Electrical spin injection and extraction refer to the generation of a non-equilibrium spin density in a non-magnetic material (NM) by the application of an electrical bias voltage across a shared interface of the NM with a ferromagnetic metal (FM). If spin-polarized charge carriers flow from the FM to the NM, one speaks of spin injection. Alternatively, a reversal of the direction of current flow also induces a non-equilibrium spin density in the NM, and this process is referred to as spin extraction.

A schematic representation of an FM/NM interface is shown in Fig. 2.1(a). The spin-dependent band structure in the ferromagnetic material leads to different re-

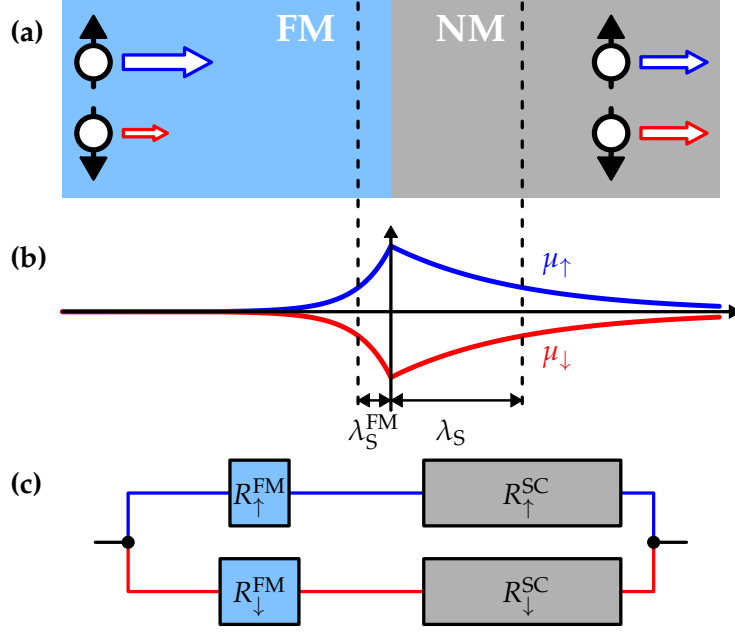


Figure 2.1: (a) Schematic representation of a ferromagnetic metal (FM)/non-magnetic material (NM) contact. The current is spin polarized in the FM and unpolarized in the NM far from the interface. (b) Profile of the electrochemical potential μ_{\uparrow} and μ_{\downarrow} for spin-up and spin-down electrons, respectively (after Ref. 32). λ_S^{FM} denotes the spin diffusion length in the FM, λ_S in the NM. (c) Two-current resistor model (after Ref. 16) with the resistances of spin-up (spin-down) electrons in the FM/semiconductor, $R_{\uparrow}^{FM/SC}$ ($R_{\downarrow}^{FM/SC}$).

sistivities for the two spin orientations (spin up or \uparrow and spin down or \downarrow) and hence the electrical current in such a material is naturally spin polarized so that the current densities of the two spin orientations in this region are generally not equal, e.g., $j_{\uparrow} > j_{\downarrow}$. Upon application of an electrical bias, a spin-polarized current flows across the interface, and an accumulation of spins occurs in the non-magnetic region. This spin accumulation corresponds to a higher density of a particular spin orientation of the conduction electrons with respect to the opposite orientation, and it is described by a difference of the electrochemical potential of spin-up and spin-down electrons,

$$\Delta\mu = \mu_{\uparrow} - \mu_{\downarrow}. \quad (2.1)$$

2.1 Electrical spin injection and extraction

Due to spin diffusion, the spin accumulation is not restricted to the interface, but reaches into the FM and NM regions. A non-zero $\Delta\mu$ corresponds to a non-equilibrium situation, and it is accompanied by spin relaxation processes so that it decays exponentially both in the FM and NM with characteristic lengths, the spin diffusion lengths λ_S^{FM} and λ_S , respectively. This behavior leads to a zone of spin accumulation close to the interface, as it is schematically depicted in Fig. 2.1(b). While the current in the FM far from the interface is spin polarized, the current in the NM is completely unpolarized far from the interface. In the steady state, the out-of-equilibrium spin distribution in the zone of spin accumulation leads to spin flips so that the incoming and outgoing spin currents are balanced.^{32,33}

When the NM is a semiconducting material as it is the case for the investigated structures in this thesis, a peculiarity occurs, which is related to the large resistivity of the semiconductor with respect to the ferromagnetic metal. It has been pointed out^{33–35} that for ohmic contacts with a low specific resistivity efficient spin injection cannot be achieved. This obstacle is referred to as the conductivity mismatch problem. A simplified description can be made using the resistor model shown in Fig. 2.1(c). In a two-current model, i.e., for two parallel conduction channels for the spin-up and spin-down electrons, the resistances for both spin orientations are equal in the semiconductor, $R_{\uparrow}^{\text{SC}} = R_{\downarrow}^{\text{SC}} = R^{\text{SC}}$. In contrast, due to the spin-dependent band structure, the resistances in the ferromagnetic metal are of a different magnitude, e.g., $R_{\uparrow}^{\text{FM}} < R_{\downarrow}^{\text{FM}}$. Since for FM/semiconductor contacts $R^{\text{SC}} \gg R_{\uparrow/\downarrow}^{\text{FM}}$, the total currents are approximately equal for both spin channels so that the spin injection is inefficient.¹⁶

When spin relaxation is taken into account, it is found³³ that not only the resistances but also the spin diffusion lengths in the two materials are important. For transparent[†] contacts, which are characterized by a low specific contact resistivity, the efficient spin injection is prevented, if the spin resistance, i.e., the product of the

[†] Strictly speaking, the condition of a transparent contact (specific contact resistivity $\rho_c \ll r_{\text{FM}}, r_{\text{SC}}$) to any semiconducting material is difficult if not impossible to fulfill experimentally as pointed out in Ref. 36. For example, the specific resistivity of a metal contact to *n*-type GaAs amounts to at least $10^{-11} \Omega\text{m}^2$, even if it is specifically designed as a low-resistance ohmic contact.³⁷ (Schottky and oxide barrier contacts are more resistive.) This value is significantly larger than a typical r_{FM} of $10^{-14} \Omega\text{m}^2$ (e.g., Ref. 38) so that such a contact cannot be considered transparent in an actual experimental situation. However, similar to the conductivity mismatch argument, a small injection efficiency is predicted for the regime $r_{\text{FM}} < \rho_c < r_{\text{SC}}$, which is sometimes referred to as the back flow or feedback regime.³⁶

Chapter 2 Background

resistivity and the spin diffusion length, of the non-magnetic material $r_{SC} = \rho_N \lambda_S$ drastically exceeds the spin resistance of the ferromagnetic metal $r_{FM} = \rho_{FM} \lambda_S^{FM}$. Here, ρ_N and ρ_{FM} denote the resistivities of the non-magnetic material and the ferromagnetic material, respectively.

Suggested ways to circumvent the conductivity mismatch problem are the use of a spin-dependent interface resistance between the ferromagnetic metal and the semiconductor,³⁹ the injection of hot electrons,⁴⁰ or the injection from a ferromagnetic half metal,³⁴ which constitutes a fully spin-polarized material. Following the theoretical descriptions of the spin injection problem, successful spin injection from ferromagnetic metals into semiconducting materials has been achieved experimentally using different solutions to the conductivity mismatch problem, such as spin injection through a Schottky tunnel barrier contact,^{17,41} an oxide barrier between the ferromagnetic metal and the semiconductor,⁴² an Esaki tunnel contact with a ferromagnetic semiconductor,⁴³ or hot-electron spin injection.⁴⁴

The samples investigated in this thesis consist of ferromagnetic metal/Schottky tunnel barrier contacts to *n*-type GaAs, for which the specific contact resistivity ρ_c significantly exceeds both r_{SC} and r_{FM} so that the conductivity mismatch does not impede the efficient spin injection. For this situation, the standard theory of spin injection^{16,32,36} predicts a magnitude of the spin accumulation in the semiconductor right at the interface of

$$\Delta\mu = 2P_G r_{SC} j = 2P_G \rho_N \lambda_S j, \quad (2.2)$$

with the spin polarization of the tunnel conductance denoted by $P_G = (G_{\uparrow} - G_{\downarrow})/G$, where $G = G_{\uparrow} + G_{\downarrow}$ is the total tunnel conductance, while $G_{\uparrow/\downarrow}$ are the tunnel conductances of spin-up and spin-down electrons, respectively. $j = j_{\uparrow} + j_{\downarrow}$ denotes the current density. When additional influences on the efficiency of spin generation are considered, P_G will be substituted by the effective spin generation efficiency P_{gen} , as it will be explained in more detail in section 4.4.3. Importantly, for tunnel contacts to the semiconductor, the generated spin accumulation is expected to be proportional to the current density as well as the spin resistance of the semiconductor.

2.2 Spin transport

A spin accumulation in a non-magnetic material is a non-equilibrium property and consequently subject to spin relaxation processes. In the following, this issue is explained for the case of the semiconducting materials with a focus on the material used in the experiments of this study, *n*-type GaAs. In addition, the spin manipulation during transport using a perpendicular magnetic field is described, which is referred to as the Hanle effect.

2.2.1 Spin relaxation in *n*-type GaAs

An imbalance of spin-up and spin-down electrons in a non-magnetic semiconductor constitutes a non-equilibrium situation. Without a persistent spin generation process, the spin accumulation therefore decays. This relaxation occurs through different processes, but can be described using a characteristic time scale, the spin lifetime τ_S .

Within the framework of the Bloch equations,³¹ a distinction is commonly made between the spin relaxation time T_1 , which corresponds to the decay time of the spin component along the direction of a static external magnetic field, and the spin dephasing time T_2 . The latter is related to the dephasing of a spin ensemble due to different precession frequencies of the individual spins in a perpendicular magnetic field. However, in this thesis, no distinction is made between T_1 and T_2 , and the decay of a spin accumulation is described using only a single characteristic time τ_S .

Four mechanisms have been identified to be the most important causes of spin relaxation of conduction electrons in non-magnetic semiconductors.³¹ First, the Elliot-Yafet mechanism plays an important role in systems with structural inversion symmetry such as Si or Ge. Here, the spin-orbit coupling leads to a certain spin flip probability during momentum scattering events. Second, the Bir-Aronov-Pikus mechanism describes the spin relaxation due to the exchange interaction with the spins of holes. This mechanism is important for photoexcited electrons in *p*-doped semiconductors.

In the samples based on bulk *n*-type GaAs channels which are investigated in this thesis, other mechanisms dominate the spin relaxation. The dependence of the

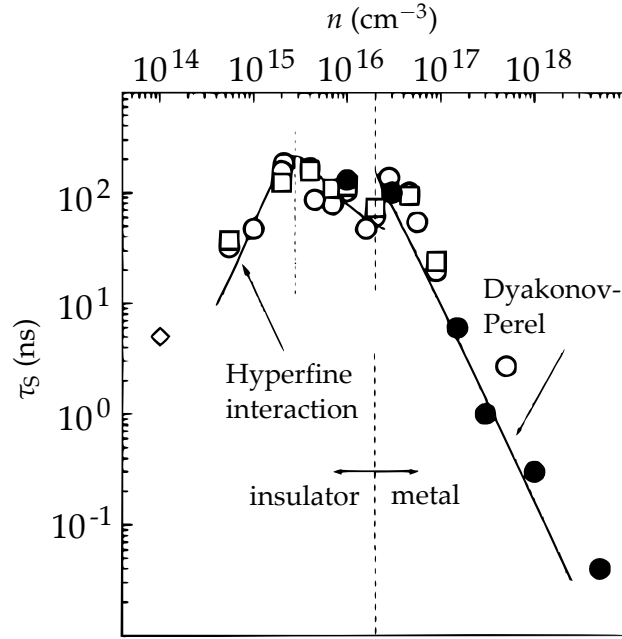


Figure 2.2: Spin relaxation time τ_S as a function of the donor concentration in GaAs at low temperatures (from Ref. 45).

spin lifetime on the doping density in n -type GaAs at low temperatures is shown in Fig. 2.2. The largest lifetimes exceeding 100 ns are observed for donor concentrations n close to the metal-insulator transition at $2 \times 10^{16} \text{ cm}^{-3}$. For lower doping densities, the spin lifetime is limited by hyperfine interaction, where donor-bound electrons interact with randomly oriented nuclear spins. To obtain long spin lifetimes, a nominal doping density of $5 \times 10^{16} \text{ cm}^{-3}$ is used for the spin transport channels in the experiments described in this thesis. In the region above the metal-insulator transition, the Dyakonov-Perel mechanism is the dominant cause of spin relaxation.

The Dyakonov-Perel mechanism occurs in semiconductors without inversion symmetry such as GaAs. In this case, a momentum-dependent spin-orbit splitting of the conduction band occurs. The individual electron spins precess in the effective spin-orbit field, which changes its sign and/or magnitude after every momentum scattering event. As a consequence and in contrast to the Elliott-Yafet mechanism, for the Dyakonov-Perel mechanism the dephasing of the spin ensemble takes place between the momentum scattering events. In addition, while the

2.2 Spin transport

Elliott-Yafet mechanism becomes more effective with stronger momentum scattering, the Dyakonov-Perel mechanism leads to an increase of τ_S in this situation.³¹

2.2.2 Hanle effect

The Hanle effect results from the spin dynamics in a magnetic field, which is not directed along the orientation of the electron spins. The spin drift-diffusion equation¹⁶ takes into account spin precession, spin diffusion, spin drift, and spin relaxation so that the time evolution of a spin density \mathbf{s} in a magnetic field H is given by

$$\frac{\partial \mathbf{s}}{\partial t} = \mathbf{s} \times \Omega_L + D \nabla^2 \mathbf{s} - v_d \nabla \mathbf{s} + \frac{\mathbf{s}}{\tau_S}. \quad (2.3)$$

Here, t denotes the time, $\Omega_L = g\mu_B\mu_0 H/\hbar$ the Larmor precession frequency, with the g -factor g , the Bohr magneton μ_B , the vacuum permeability μ_0 , and the reduced Planck constant \hbar . v_d is the electron drift velocity and D the spin diffusion coefficient, which is related to the spin lifetime τ_S via the spin diffusion length λ_S as

$$\lambda_S = \sqrt{D\tau_S}. \quad (2.4)$$

Note that the spin diffusion length λ_S determines the spatial profile of the spin accumulation for the case of pure diffusion. If electric fields are present, however, the characteristic length scale determining the spatial distribution of the spin accumulation can be enhanced along the direction of electron flow. In this case, one speaks more generally of the spin drift length, while the term spin relaxation length generally refers to both cases.¹⁶

The solution to equation 2.3 can be given for the experimentally relevant situation of a one-dimensional spin transport geometry, where a spin accumulation is generated at point 0 and is detected at a point x . During transport, this spin accumulation is subject to a magnetic field applied along the z -direction, i.e., perpendicular to the orientation of the spins. Due to diffusive transport, the spins reach x via many different paths so that they exhibit a wide range of flight times during which they precess and relax. Therefore, the integration over all transit times t is necessary so that all electrons reaching x on their diffusive paths are taken into account. The y component of the spin density at x can then be written

as¹⁶

$$s_y(x) \propto \int_0^\infty \frac{1}{\sqrt{4\pi Dt}} e^{-(x-v_d t)^2/(4Dt)} e^{-t/\tau_s} \cos(\Omega_L t) dt. \quad (2.5)$$

Due to diffusive motion, the distribution of the transit times is determined by the diffusion coefficient D . The second exponential term represents spin relaxation during transport, while the cosine function describes the spin precession with the Larmor frequency.

Equation 2.5 can be numerically integrated to obtain fit curves for magnetic-field dependent voltages generated by a spin accumulation in one of the electrical detection schemes described in the next section. As a consequence, the occurrence of Hanle curves can be regarded as a proof of successful spin injection. In addition, Hanle curves can be used to determine the spin lifetime in the non-magnetic material.

2.3 Electrical detection of a spin accumulation

An overview of the electrical spin detection schemes used in this study is shown in Fig. 2.3. First, an established method is the three-terminal spin detection (3T), which uses only one ferromagnetic contact and is shown in Fig. 2.3(a). Second, the non-local spin valve (NLSV) demands two ferromagnetic contacts and is characterized by a separation into a charge transport and spin generation region on the left-hand side of Fig. 2.3(b) as well as a region of purely diffusive spin transport on the right-hand side, where the detection occurs. Furthermore, in the local spin valve (LSV) arrangement of Fig. 2.3(c), the local resistance is measured between two ferromagnetic contacts. This LSV essentially constitutes an FM/NM/FM structure. Finally, Fig. 2.3(d) shows the extraction spin valve (ESV), which has not been previously described in the literature. In the following, the corresponding measurement geometries will be explained in more detail.

2.3.1 Three-terminal spin detection

The three-terminal method of Fig. 2.3(a), i.e., using a single ferromagnetic contact for both the spin generation and spin detection, has the advantage that it does not necessitate small structures on the micrometer scale as it is the case for the NLSV,

2.3 Electrical detection of a spin accumulation

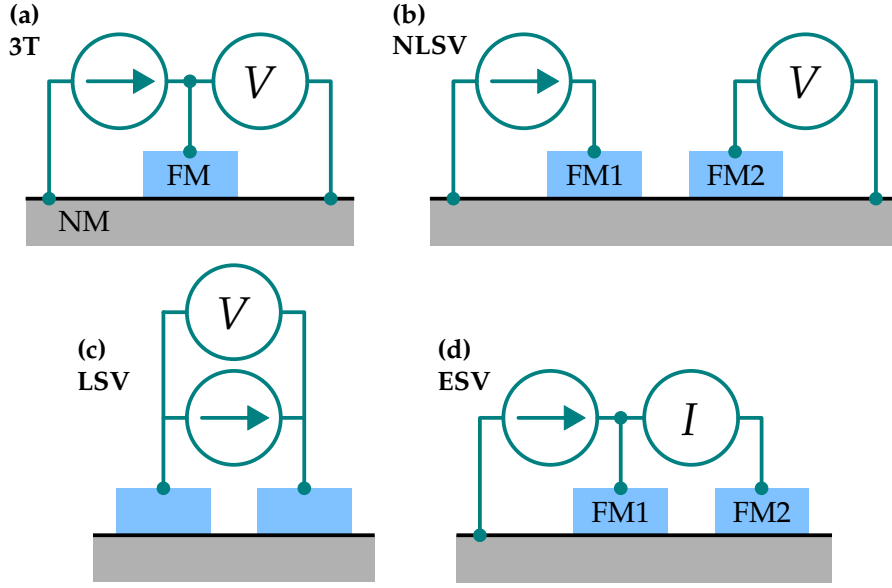


Figure 2.3: Measurement geometries for spin transport experiments on structures consisting of ferromagnetic metal (FM) contacts on a non-magnetic (NM) channel. **(a)** Three-terminal (3T), **(b)** non-local spin valve (NLSV), **(c)** local spin valve (LSV), and **(d)** extraction spin valve (ESV) geometry. Sources of constant current are depicted as circled arrows. V and I indicate voltage and current measurements, respectively.

LSV, and ESV, where spin relaxation during spin transport from the generation to the detection point demands a close proximity of the ferromagnetic contacts. For the same reason, the measured signals using the three-terminal scheme are comparatively large so that this method constitutes a very useful technique for the study of spin injection and spin extraction. It has been applied to various ferromagnet/semiconductor combinations, where a spin accumulation has been detected in GaAs,^{46–48} Si,^{19,49–51} and Ge.^{52,53} However, an important disadvantage of this method is the fact that, since the measurement scheme does not require spin transport in the semiconducting channel, one cannot be certain from 3T data alone that the generated spin polarization is located in the conduction band of the semiconductor, which is important for practical application and constitutes an important requirement for proposed spin-manipulation schemes.¹⁵ In this context, spin accumulation values which drastically exceed the theoretical expectation have been found in many experiments.^{19,47,49,50,54,55} This spin accumulation has

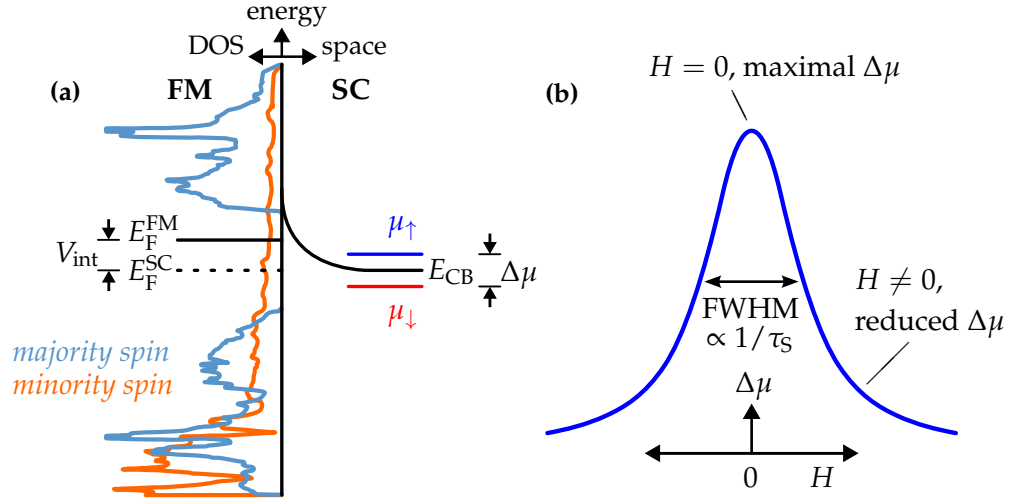


Figure 2.4: **(a)** Schematic representation of a ferromagnetic metal (FM)/*n*-type semiconductor (SC) Schottky contact. Depicted is the spin-dependent density of states (DOS) of the Heusler alloy Co_2FeSi . The application of a bias voltage $V_{int} = E_F^{FM} - E_F^{SC}$ (with E_F^{FM} and E_F^{SC} describing the Fermi levels in the FM and the SC, respectively) induces a splitting of the electrochemical potentials for spin-up and spin-down electrons (μ_{\uparrow} and μ_{\downarrow} , respectively) in the SC close to the interface. E_{CB} denotes the bottom edge of the semiconductor conduction band. **(b)** The application of a perpendicular magnetic field H induces a spin precession and spin dephasing, leading to a Lorentzian field-dependence of $\Delta\mu$ according to equation 2.11, with a full width at half maximum (FWHM), which is inversely proportional to the spin lifetime τ_S [(b) is adapted from Ref. 19].

been attributed to localized interface states rather than the conduction band of the semiconductor.⁴⁷

To explain the measurement principle, a ferromagnet/semiconductor (SC) Schottky contact is schematically depicted in Fig. 2.4(a). The density of states is shown for the ferromagnetic Heusler alloy Co_2FeSi , which exhibits a band gap for minority spins according to the calculation presented in Ref. 56. Upon application of an electrical voltage V_{int} , the spin-dependent tunneling across the interface leads to the generation of a spin accumulation in the conduction band of the semiconductor as described by the difference of the electrochemical potentials μ_{\uparrow} and μ_{\downarrow} .

2.3 Electrical detection of a spin accumulation

Following the argument made in Ref. 36, the tunnel currents of spin-up (I_{\uparrow}) and spin-down (I_{\downarrow}) electrons are

$$I_{\uparrow} = G_{\uparrow}(V_{\text{int}} - \Delta\mu/2), \quad (2.6)$$

$$I_{\downarrow} = G_{\downarrow}(V_{\text{int}} + \Delta\mu/2). \quad (2.7)$$

The corresponding charge and spin currents are then given by

$$I = I_{\uparrow} + I_{\downarrow} = GV_{\text{int}} - P_G G \Delta\mu/2, \quad (2.8)$$

$$I_S = I_{\uparrow} - I_{\downarrow} = P_G G V_{\text{int}} - G \Delta\mu/2. \quad (2.9)$$

Equation 2.8 can be rewritten as

$$V_{\text{int}} = \frac{\rho_c}{A} I + P_G \Delta\mu/2, \quad (2.10)$$

with the area of the contact A . From this expression, it is seen that the spin accumulation $\Delta\mu$ can be detected as an additional, spin-induced voltage drop across the contact.

To separate the relatively small spin-induced signal (second term on the right-hand side of equation 2.10) from the conventional charge resistance term (first term), $\Delta\mu$ is commonly modulated via the Hanle effect. As explained in section 2.2.2, the Hanle effect is observed when a magnetic field is applied perpendicular to the spin orientation. The resulting decay of the spin accumulation with increasing magnetic field H due to spin precession and dephasing is schematically depicted in Fig. 2.4(b). As pointed out in the supplemental material of Ref. 19, equation 2.5 reduces to a Lorentzian curve for one ferromagnetic detection contact after integration over the contact area, and the magnetic-field dependence of the spin accumulation is given by

$$\Delta\mu(H) = \frac{\Delta\mu(H=0)}{1 + (\Omega_L \tau_S)^2}. \quad (2.11)$$

Importantly, the width of the Hanle curve is inversely proportional to the spin lifetime τ_S .

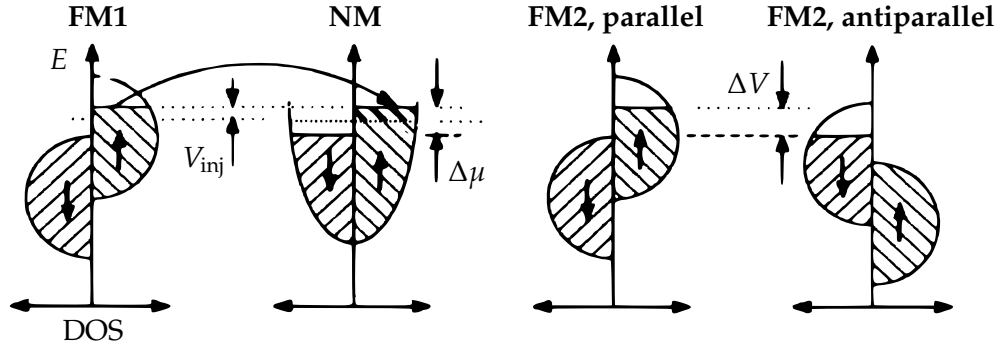


Figure 2.5: Schematic representation of the density of states (DOS) as a function of energy E for the ferromagnetic injector contact FM1, the non-magnetic channel (NM), and the ferromagnetic detector contact FM2 in the non-local spin valve geometry of Fig. 2.3(b). A voltage V_{inj} is applied to FM1 leading to spin injection and hence a spin accumulation $\Delta\mu$ builds up in NM. This spin accumulation is detected (neglecting spin relaxation in NM) at FM2 and results in a voltage change ΔV upon magnetization reversal (from Ref. 58).

2.3.2 Non-local spin valve

In the non-local spin valve geometry, the spin and charge currents are separated as depicted in Fig. 2.3(b). The left ferromagnetic contact FM1 carries a current, which results in the electrical generation of a spin accumulation in the semiconducting channel. On the left-hand side, where the charge current flows, the spin accumulation is subject to both drift and diffusion. To the right of the spin generating contact, however, the spin transport is purely diffusive, and the spin accumulation decays exponentially with distance from the spin generating contact. The spin accumulation is detected by the open circuit on the right-hand side, where Johnson-Silsbee spin-charge coupling^{16,57} induces measurable potential drops across the right ferromagnetic contact FM2. This detection scheme has been first applied to all-metallic spin valves^{57–61} and is also an established tool for the study of spin transport in ferromagnet/semiconductor systems.^{62–64}

To illustrate the working principle of the NLSV, the spin injection as well as the detection mechanisms are schematically presented in Fig. 2.5 in terms of simplified band structure diagrams. The density of states in the ferromagnetic metals FM1 and FM2 is spin-dependent (shown is the particular case of a fully spin po-

2.3 Electrical detection of a spin accumulation

larized material). As a consequence, the application of an electrical bias V_{inj} across the FM1/NM interface leads to a spin-polarized current and induces a spin accumulation $\Delta\mu$ in the non-magnetic channel as indicated by the higher filling of the spin-up band. After spin diffusion toward FM2, the spin accumulation forces the electrochemical potential of this floating electrode to adjust according to the prerequisite of no charge flow into FM2 in the steady state. This mechanism results in the appearance of a spin-induced non-local voltage.

Because background signals occur even in the non-local geometry, the spin-dependent signal is frequently modulated by the application of an external magnetic field to separate it from spurious signals. The spin valve measurement makes use of a magnetic field applied along the easy axis of magnetization of the ferromagnetic contacts so that the change in the non-local voltage is observed upon a switching between a parallel and an antiparallel magnetization configuration. As seen from Fig. 2.5, when spin relaxation during the diffusive transport between FM1 and FM2 is neglected, the reversal of the magnetization direction of one ferromagnetic contact leads to a change of the non-local voltage by $\Delta V = \Delta\mu$, if FM2 is fully spin polarized. Otherwise, a spin detection efficiency of less than unity has to be taken into account. Alternatively, the spin transport can be studied using the manipulation of the spin accumulation during transport in the NM via the Hanle effect as it was the case for the three-terminal detection and according to equation 2.5.

Essentially, the change in the non-local voltage upon magnetization reversal can be deduced from equations 2.2 and 2.10 for $I = 0$ (i.e., no current flow across the detecting contact) and by taking into account the exponential decay of the spin accumulation with distance d between the generation and detection points,

$$\Delta V = P_G \Delta\mu \exp(-d/\lambda_S) = (P_G)^2 \rho_N \lambda_S j \exp(-d/\lambda_S). \quad (2.12)$$

For the interpretation of the data presented in chapter 4, additional geometrical factors will be considered.^{16,60,65} Furthermore, a distinction will be made between the efficiency of spin generation P_{gen} and the efficiency of spin detection P_{det} . This discrimination proves convenient, because the bias conditions of FM1 and FM2 are in general very different.

2.3.3 Local spin valve

The local spin valve geometry is depicted in Fig. 2.3(c). This FM/NM/FM structure constitutes a technologically relevant arrangement, because its two-terminal resistance can be modulated by the relative orientation of the magnetizations of the ferromagnetic contacts. With metallic materials as the NM spacer, the local spin-valve scheme and the giant magnetoresistance effect^{7,8} are used for the read-out of magnetic data in hard disk drives allowing for a high areal recording density. In addition, FM/NM/FM structures – in particular in the form of magnetic tunnel junctions,¹² in which the NM is a thin, insulating barrier – find application as the memory cells in magnetoresistive random access memories.¹⁴

Local spin valves using semiconductors as the NM are particularly interesting as several proposed spin manipulation schemes in spin-based transistor concepts rely on the semiconducting properties of the channel.^{15,31,66} Aside from the manipulation mechanism used during spin transport, these device concepts demand the efficient spin injection, transport, and detection in the local, lateral geometry of Fig. 2.3(c). The important figure of merit is the magnetoresistance ratio $MR = \Delta R / R_p$, where $\Delta R = R_{ap} - R_p$, with R_{ap} (R_p) denoting the resistance in the antiparallel (parallel) magnetization configuration.

In contrast to the non-local spin generation and detection, the experimental demonstration of the local spin valve operation is challenging and has been shown in rare cases only.^{64,67–69} The reasons lie in the occurrence of strong electrical background signals unrelated to the spin accumulation as well as the difficulty to fulfill the theoretically formulated requirements,³³ which are sometimes referred to as Fert's criterion and are discussed below. In addition and compared to the non-local geometry, the local spin valve is more prone to spurious signals, because the spin and charge currents are no longer separated. Physical effects, which can make the interpretation of LSV resistances difficult, include the local Hall effect,^{70,71} where the magnetic stray fields generated by the ferromagnetic contacts lead to a spurious Hall voltage. Furthermore, lateral currents in the ferromagnetic contacts can generate unwanted anisotropic magnetoresistance signals, which also lead to magnetization-dependent voltage changes. In addition, tunneling anisotropic magnetoresistance⁷² can induce spin-valve like signals if multiple-step magnetization reversal processes occur in the FM. The signatures of these phenomena can

2.3 Electrical detection of a spin accumulation

be similar to that of the desired local spin valve measurement so that these spurious signals can be difficult to separate from the true local spin valve signals. However, spatially dependent measurements yielding an exponential decay of the signal with the spin drift length taken together with Hanle measurements, where the local spin valve voltage is measured as a function of a perpendicular magnetic field, allow for a high degree of confidence that the measured signal indeed originates from a true spin-valve effect. Spatially-dependent measurements on samples similar to those investigated in this thesis are found in Ref. 73. In addition, local Hanle effect measurements are presented in section 5.4.

In addition to the conductivity mismatch problem, which demands a lower limit of the interface resistance between the ferromagnetic contact and the semiconductor for efficient spin injection, the operation in the local spin valve geometry further necessitates an upper limit of the interface resistance. The latter constraint is related to the average time that an electron spends in the channel with respect to its spin relaxation time.

The magnetoresistance ratio in FM/NM/FM structures can be quantified as shown by the calculations in Ref. 33, and the result is depicted in Fig. 2.6 for an FM/SC/FM structure in a current-perpendicular-to-plane geometry. For the observation of a maximal magnetoresistance signal, the specific contact resistivity has to lie in a relatively narrow range, which is determined by the ratio of the specific contact resistivity and the spin resistance of the semiconducting channel. In addition, the maximal MR of $P_{\text{gen}}^2 / (1 - P_{\text{gen}}^2)$ is reached only if the transport length is significantly shorter than the spin relaxation length.

Geometrical corrections apply for a lateral geometry as in Fig. 2.3(c), and the Fert condition for an appreciable magnetoresistance is^{32,64}

$$\frac{d}{\lambda_S} \ll \frac{w}{W} \frac{\rho_c}{\rho_N \lambda_S} \ll 1, \quad (2.13)$$

where w denotes the thickness of the channel and W the width of the contacts. The left inequality relates to the conductivity mismatch problem. The inequality on the right can be expressed in terms of the dwell time of the electrons in the channel,³² which may not exceed the spin lifetime when a large MR is desired.

Some strategies for the improvement of the performance of FM/NM/FM de-

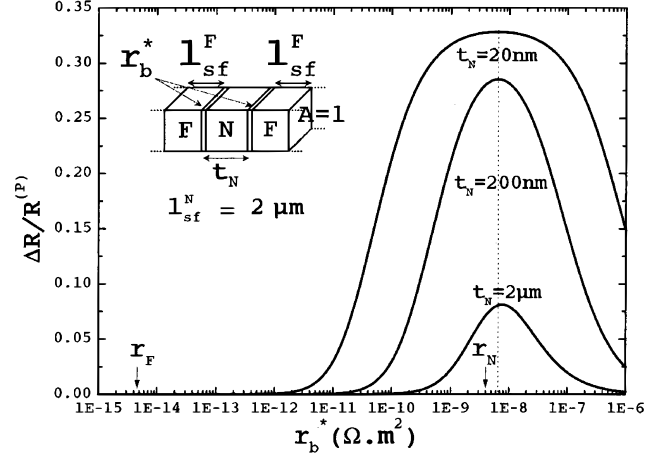


Figure 2.6: Calculated magnetoresistance ratio $\Delta R/R^{(P)} = \text{MR}$ of a ferromagnetic metal (F)/tunnel barrier (I)/semiconductor (N)/I/F structure (shown in the inset) with the spin diffusion lengths in the F, $l_{sf}^F = \lambda_S^{\text{FM}} = 60 \text{ nm}$, and in the N, $l_{sf}^N = \lambda_S$. $t_N = d$ denotes the spin transport length, $r_b^* = \rho_c$ is the specific contact resistivity of the tunnel barrier, and $r_F = r_{\text{FM}}$ and $r_N = r_{\text{SC}}$ are the spin resistances of the ferromagnetic metal and the semiconductor, respectively. The calculation was performed with a spin generation efficiency P_{gen} of 50% (from Ref. 33).

vices can be discussed based on equation 2.13. For a reduction of the left term, it is clear that the transport length d should be small with respect to the spin relaxation length λ_S . The latter can be increased by using a different non-magnetic channel material, but only few materials with a spin diffusion length exceeding that of GaAs with an optimized doping density according to Fig. 2.2 have been reported (including graphene with λ_S of more than $100 \mu\text{m}$ ⁷⁴). A decrease of d can be achieved by using electron-beam lithography for smaller feature sizes (the samples investigated in this thesis are fabricated by standard photolithography methods). Alternatively, using a vertical (current-perpendicular-to-plane) instead of the lateral geometry could allow for a drastic reduction of the spin transport length. For example, the epitaxial growth of vertical Fe_3Si /semiconductor/ Fe_3Si structures has been demonstrated,⁷⁵ but it has to be kept in mind that the vertical geometry may not be suitable for electrical spin manipulation schemes.¹⁵

Note that the specific contact resistivities ρ_c of the samples investigated in this thesis are too high to fulfill the right inequality of equation 2.13. Consequently,

2.3 Electrical detection of a spin accumulation

the term in the center has to be reduced to obtain an increase in the MR. An analysis focusing on the reduction of ρ_c is performed in section 4.8. Apart from an optimization of ρ_c , ρ_N , and λ_S , the ratio w/W can be reduced in the lateral geometry. However, an increase of the contact width W demands an increase of the center-to-center spacing between the detection and generation points, which would make the left inequality more difficult to satisfy. A decrease in the channel thickness w constitutes the most promising approach and suggests the use of a two-dimensional electron gas³⁸ or graphene⁷⁴ as the NM.

2.3.4 Extraction spin valve

While the above-mentioned measurement geometries constitute well-established tools for the study of all electrical spin transport, a novel approach is introduced in this thesis. The arrangement is depicted in Fig. 2.3(d) and is referred to as an extraction spin valve. As for the NLSV and LSV, spin-valve and Hanle signals are the signatures of spin transport in the ESV geometry. The working principle of the ESV is essentially described by a local spin valve, which uses spin extraction instead of spin injection for the generation of the spin accumulation in the non-magnetic channel. In a current divider arrangement, an unpolarized drift current becomes spin-polarized by spin extraction at FM1 in Fig. 2.3(d). Then, this spin-polarization is detected using the spin-dependent transmission at FM2. As a consequence, the distribution of currents among the two output leads depends on the relative magnetization orientation of FM1 and FM2 as explained in detail in chapter 5.

Interestingly and in contrast to the three other spin detection schemes, the extraction spin valve can be extended to lateral devices comprising multiple spin generation events. This will be explained in more detail in sections 5.4 and 5.6.

CHAPTER 3

Experimental

In this chapter, the experimental techniques that are used to obtain the results in the following two chapters are described including the fabrication of spin transport devices using the growth by molecular beam epitaxy and the processing by optical lithography. Furthermore, the setup used to perform the spin transport measurements is discussed.

3.1 Sample preparation

3.1.1 Sample growth

The samples investigated in this work were fully grown by molecular beam epitaxy (MBE) in a multiple-chamber system. The apparatus comprises a chamber for the growth of semiconductor materials (based on GaAs, Ge, and Si) interconnected under ultra-high vacuum (UHV) conditions with a chamber for the deposition of elementary metals (e.g., Co, Fe, and Al) and their alloys (in particular Fe_3Si , Co_2Fe , and Co_2FeSi). The semiconducting part is nominally the same for all investigated samples, and the growth sequence from bottom to top is as follows (summarized in Fig. 3.1). First, a semi-insulating GaAs(001) substrate is loaded into the MBE system and heated to a substrate temperature T_S of about 580 °C under

10 nm	Ferromagnetic metal	
15 nm	GaAs:Si ($n_{\text{interface}} = 5 \times 10^{18} \text{ cm}^{-3}$)	
15 nm	GaAs:Si ($n_{\text{channel}} \rightarrow n_{\text{interface}}$)	
1500 nm	GaAs:Si ($n_{\text{channel}} = 5 \times 10^{16} \text{ cm}^{-3}$)	
5 nm	GaAs	} 50×
5 nm	Al _{0.33} Ga _{0.67} As	
300 nm	GaAs	
GaAs(001) semi-insulating substrate		

Figure 3.1: Layer sequence of the spin transport devices grown by molecular beam epitaxy (system operated by J. Herfort and C. Herrmann).

UHV conditions for oxide desorption. Next, an approximately 300-nm-thick and not intentionally doped GaAs buffer layer is grown to obtain a flat and clean surface. Furthermore, a subsequently grown $50 \times \text{Al}_{0.33}\text{Ga}_{0.67}\text{As}(5 \text{ nm})/\text{GaAs}(5 \text{ nm})$ ($T_S = 610 \text{ }^\circ\text{C}$) superlattice structure is intended to further capture impurities and enable a higher-quality active region. Afterward, an n -type (silicon-doped) GaAs layer with a thickness of $1.5 \text{ }\mu\text{m}$ is grown at $T_S = 580 \text{ }^\circ\text{C}$ to act as the conductive semiconducting channel in the spin transport experiments. The nominal donor density of $n_{\text{channel}} = 5 \times 10^{16} \text{ cm}^{-3}$ is chosen to be close to the metal-insulator transition in GaAs with the intent to achieve long spin lifetimes.⁴⁵ Then, a layer with a thickness of 15 nm and a linearly increasing doping density ranging from n_{channel} to $n_{\text{interface}} = 5 \times 10^{18} \text{ cm}^{-3}$ is grown followed by the 15-nm-thick top-most heavily doped ($n_{\text{interface}}$) GaAs layer. The high level of doping near the interface with the ferromagnetic metal yields a narrow Schottky barrier, which can be overcome by the conduction electrons via tunneling. Hereafter, the samples are transferred under UHV into the growth chamber for metals, where approximately 10-nm-thick layers of the ferromagnetic metals Fe₃Si, Co₂Fe (both chapter 4), and Co₂FeSi (chapter 5) are deposited. The growth of these alloys on GaAs(001) is well-established and details can be found, e.g., in Refs. 76–79.

3.1 Sample preparation

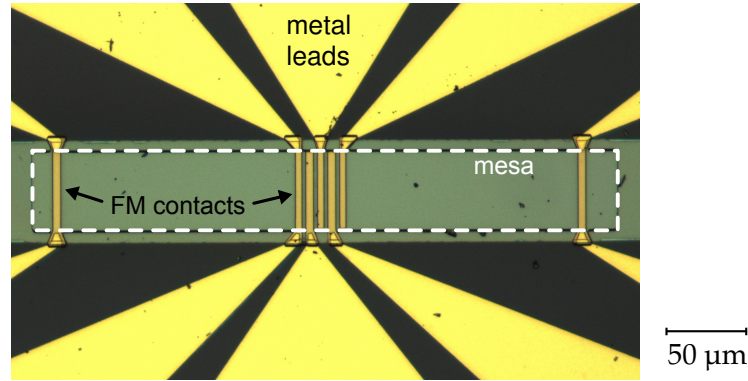


Figure 3.2: Sample surface showing the arrangement of the ferromagnetic metal (FM) contacts on the conducting n -type GaAs mesa region.

3.1.2 Sample processing

After the growth, lithography steps are necessary to process the samples into lateral spin transport devices. An optical micrograph of the fully processed sample surface showing the arrangement of ferromagnetic contacts on a semiconducting mesa region is presented in Fig. 3.2. To obtain the desired structures, standard photolithography techniques are used. During one processing run, several devices (with different geometries) are simultaneously fabricated on a piece with a typical size of $1 \times 1 \text{ cm}^2$ cleaved from an MBE-grown quarter of a 2-inch wafer. The processing sequence is described in the following.

First, Ti (thickness 10 nm) and Au (120 nm) layers are evaporated in a stripe pattern, which serves as an etch mask to define the shape of the ferromagnetic stripe contacts. The orientation of the long side of the stripes is chosen to coincide with the magnetic easy axis of the ferromagnetic metal for the samples which exhibit a pronounced magnetic anisotropy. Then, dry etching of the ferromagnetic metal layers, the heavily-doped interfacial region, and the upper region of the channel with a total depth of about 100 nm ensures that spin and charge transport between the stripes occurs in the channel region doped with n_{channel} . Next, a wet etching step with a depth of at least 1500 nm is performed to define a conductive mesa region with an area of $54 \times 400 \text{ μm}^2$. Afterward, the sputter deposition of a 150-nm-thick SiO_2 layer ensures the electrical insulation of the semiconducting channel from the metallic contact leads, which are deposited in the final process-

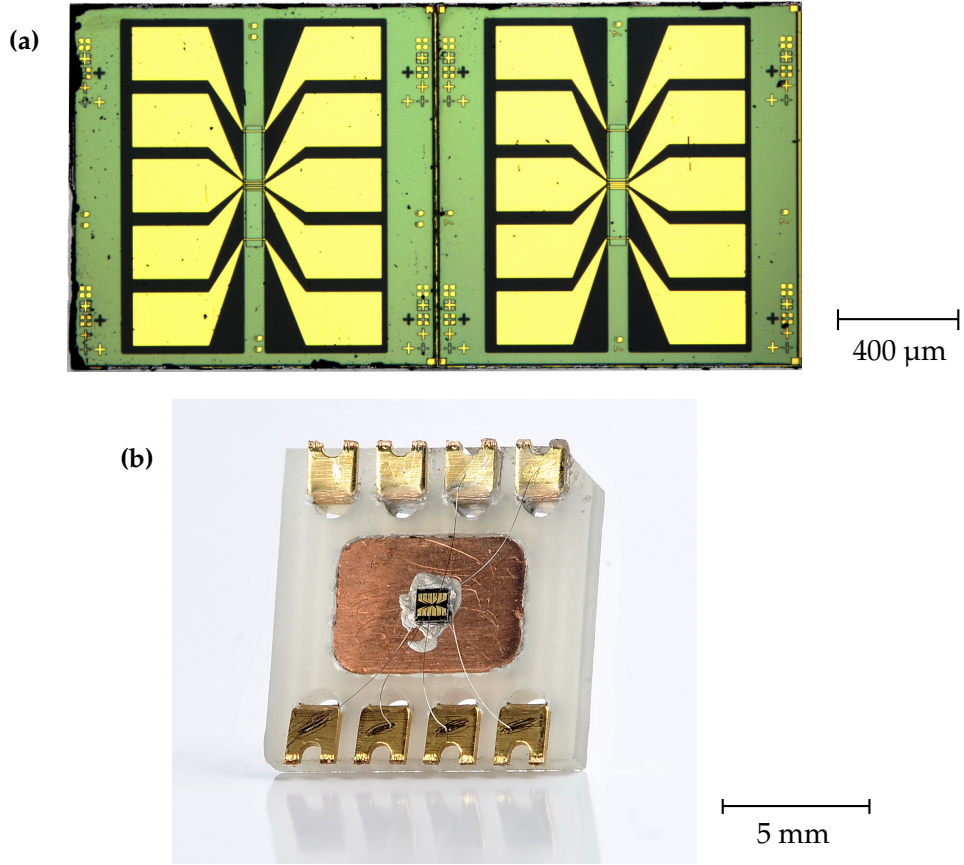


Figure 3.3: (a) Optical micrograph of processed sample pieces. (b) Wire-bonded sample on an eight-pin chip carrier.

ing step. These metal leads and the accompanying bond pads provide the electrical contact to the ferromagnetic stripes and consist of evaporated Ti (thickness 10 nm) and Au (150 nm) layers. In addition, during the processing procedure of the spin transport devices, sample pieces with AuGe contacts on Hall bars are fabricated for conventional carrier density and mobility measurements. The mask was designed together with P. Bruski, and the processing steps were performed by W. Anders. More detailed information about the processing of spin transport structures can be found in Ref. 73.

After the lithographic processing, the sample is mounted onto an eight-pin chip carrier and wire-bonded. As examples, optical images of two of the total 64 de-

3.2 Experimental setup for spin transport measurements

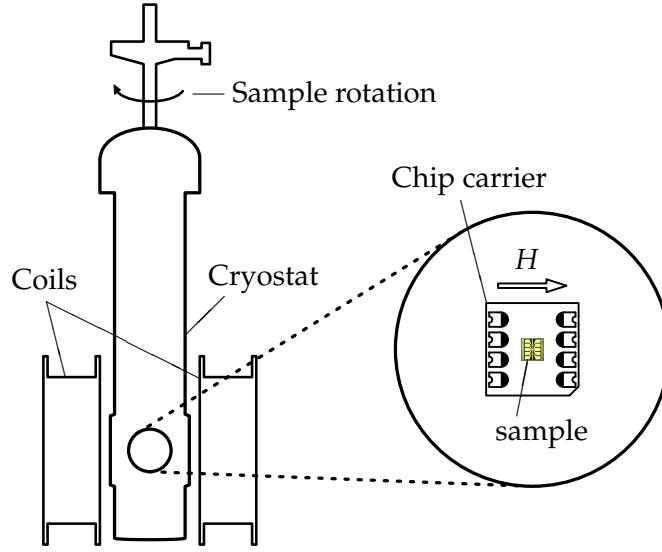


Figure 3.4: Schematic diagram of the setup used for spin transport measurements. H denotes the orientation of the magnetic field.

vices, which are fabricated in one processing run, as well as a sample on a chip carrier are presented in Fig. 3.3.

3.2 Experimental setup for spin transport measurements

The experimental setup used for the electrical generation and detection of a spin accumulation in the GaAs channel is schematically shown in Fig. 3.4. The chip carrier is placed inside a He exchange gas cryostat (Oxford Instruments), which allows for the cooling of the sample down to a minimal temperature between 4 and 5 K. The temperature is adjusted by means of an Oxford ITC 4 temperature controller system. A manipulator is used to set the desired orientation of the sample with respect to a magnetic field, which is applied using current-carrying Helmholtz coils in close proximity to the cryostat. The coils are positioned so that the sample is centered with respect to them. Their current is supplied by a Kepco bipolar operational power supply, which facilitates a maximal current of about 7 A corresponding to a magnetic field with $\mu_0 H = 20$ mT at the position of the sample. The accuracy of $\mu_0 H$ amounts to about ± 0.03 mT.

Chapter 3 Experimental

In addition, wire connections leading into the sample space enable the application of direct currents to the spin transport structures using a Keithley 236 source measure unit. Alternating currents are supplied by a Keithley 6221 current source. Furthermore, a nanovoltmeter (Keithley 2182A) measures constant voltages, and a Stanford SR850 lock-in amplifier is used for phase-sensitive detection.

During a typical measurement procedure, an electric current is applied to specified terminals of the spin transport structure, while a voltage is read-out between these or different terminals as a magnetic field is applied. Automated control of field sweeps, data acquisition, and instrument control are performed using a computer program written in National Instruments LabVIEW.

CHAPTER 4

Electrical spin generation in ferromagnet/*n*-GaAs hybrid structures

This chapter deals with experiments performed on lateral spin transport devices based on *n*-type GaAs channels with different ferromagnetic injector metals. The central results are:

- Fe₃Si/*n*-GaAs is a suitable hybrid system for the study of all-electrical spin generation, transport, and detection in the non-local, three-terminal, and local geometries.
- The efficiency of spin generation from Fe₃Si layers into *n*-GaAs decays with interface bias, which limits the operational conditions of spin transport devices, especially those relying on spin injection.
- Comparable spin generation efficiencies of different contacts yield drastically different spin signals depending on the spin-independent current-voltage characteristics.
- Spin-induced signals in the three-terminal geometry are consistent with standard theory as well as results obtained from non-local measurements and hence originate from a spin accumulation in the conduction band of GaAs rather than from interface states.

4.1 Introduction

Numerous spintronic device concepts rely on the efficient electrical generation of a spin accumulation inside a semiconductor (SC) using the interface with a ferromagnetic metal (FM). As explained in chapter 2, the application of a reverse bias to an FM/*n*-type SC hybrid contact leads to the injection of spin-polarized electrons into the SC. Alternatively, an applied forward bias can be used to generate a spin accumulation of opposite sign⁸⁰ due to the extraction of electrons with a particular spin orientation. Frequently employed all-electrical spin generation and detection schemes make use of a lateral semiconductor channel with multiple ferromagnetic contacts. Typical geometric arrangements include the non-local and the three-terminal geometries, in which successful spin injection and detection have been reported for GaAs,^{46,62,64} Si,^{19,81} and Ge^{20,50} channels, amongst others using the ferromagnetic metals Fe₃Si on *n*-Si⁸² as well as CoFe on *n*-GaAs⁸³ and *n*-Si.⁸⁴ In addition, spin transport in the technologically more relevant two-terminal arrangement of the local spin valve has been demonstrated.^{64,67–69} However, unambiguous reports of local spin valve operation are scarce due to the presence of large spin-independent background signals and the difficulty to fulfill the requirements of the dwell time and feedback problems³³ (cf. section 2.1). For the same reason, only small magnetoresistance ratios are observed.

The efficiency of the spin generation process has been found to depend sensitively on the choice of the FM, as it has been observed in studies using spin light-emitting diodes (LEDs) based on GaAs, where the injection efficiency was found to be significantly higher for Co₂FeSi⁸⁵ as compared to Fe,¹⁷ MnAs,⁸⁶ and Fe₃Si⁸⁷ injectors. This increase in efficiency has been attributed to the spin-dependent band structure of Co₂FeSi. The results of this chapter emphasize that the spin-independent current-voltage characteristics also have a strong influence on the spin injection properties of a contact. Lateral spin valve structures with an *n*-type GaAs channel and different FM contacts are studied. The investigation focuses on Fe₃Si contacts, but also results obtained using a Co₂Fe spin source are presented for comparison. Spin transport measurements in the non-local, three-terminal, and local geometries show that the electrical properties of the contacts even constitute the dominating design parameter regarding spin injection in these samples.

Table 4.1: Parameters of the samples used in this chapter. FM denotes the ferromagnetic material and T_S is the substrate temperature during growth of the ferromagnetic metal layer. d is the center-to-center spacing between the central contacts, and W_1, W_2, \dots are their widths.

Sample	FM	T_S (°C)	d (μm)	W_1, W_2, \dots (μm)
A1	Fe ₃ Si	50	11.5	5, 5, 5
A2	Fe ₃ Si	50	7.5	4, 5, 4, 5, 4
A3	Fe ₃ Si	50	18.5	22, 9
B	Fe ₃ Si	200	18.5	22, 9
C	Co ₂ Fe	50	7.5	4, 5, 4

4.2 Experimental

The samples were grown and processed as explained in chapter 3. A total of five samples are investigated in this chapter, all consisting of ferromagnetic metal layers with a thickness of approximately 10 nm grown epitaxially on an n -type GaAs channel with a thickness w of 1.5 μm. While the semiconducting part is nominally the same for all samples, the samples feature different ferromagnetic materials or contact geometries. Their contact materials as well as the growth temperatures and some important geometrical properties are summarized in Table 4.1.

Three of the samples are cleaved from the same wafer and are referred to as A1, A2, and A3. All of these devices contain an Fe₃Si contact layer grown at a substrate temperature T_S of 50 °C as the ferromagnetic spin generator. For this growth temperature, the ferromagnetic metal layer is amorphous as seen from the lack of interference fringes in the x-ray diffraction curves of Fig. 4.1. The amorphous growth of Fe₃Si at low temperatures has previously been ascribed to a low adatom mobility.⁷⁶ The widths and the spacings of the ferromagnetic contacts differ among samples A1–A3 as explained in the next paragraph. Sample B also makes use of Fe₃Si as the ferromagnetic metal. However, in contrast to samples A1–A3, the substrate temperature during growth is 200 °C, which yields a crystalline ordering of the film. Detailed information about the epitaxial growth of Fe₃Si on GaAs(001) can be found in the literature.^{76,77} For sample C, a crystalline

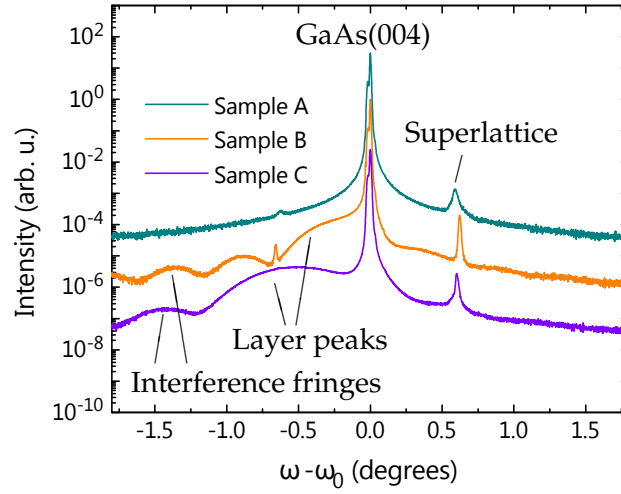


Figure 4.1: $\omega - 2\theta$ x-ray diffraction curves around the GaAs(004) reflection (strong line at $\omega - \omega_0 = 0^\circ$, $\omega_0 = 33^\circ$) for the unprocessed samples A, B, and C. The other sharp lines stem from the $50 \times (\text{Al}_{0.33}\text{Ga}_{0.67}\text{As}/\text{GaAs})$ superlattice. Diffraction peaks and thickness interference fringes originating from the ferromagnetic layers are observed for samples B and C (data acquired by J. Herfort).

Co_2Fe film grown at 50°C acts as the FM spin source.

The ferromagnetic contacts are arranged on the conductive GaAs mesa region with an area of $54 \times 400 \mu\text{m}^2$ as schematically shown in Fig. 4.2. The spacing between the outer contacts (labeled L and R) and the central contacts (labeled 1, 2, 3, ...) amounts to more than $150 \mu\text{m}$, which exceeds the spin relaxation length in the semiconducting channel by more than one order of magnitude. As a consequence, L and R serve as sources of unpolarized electrons or reference potential probes.

All measurements in this chapter are performed using a steady-state technique with a nanovoltmeter for the detection of potential drops, except for the Hanle curves presented in section 4.4.2, which are measured using a lock-in amplifier in conjunction with alternating currents. The measurements are conducted at a temperature of 20 K unless otherwise indicated.

4.3 Ferromagnetic metal/*n*-GaAs contacts

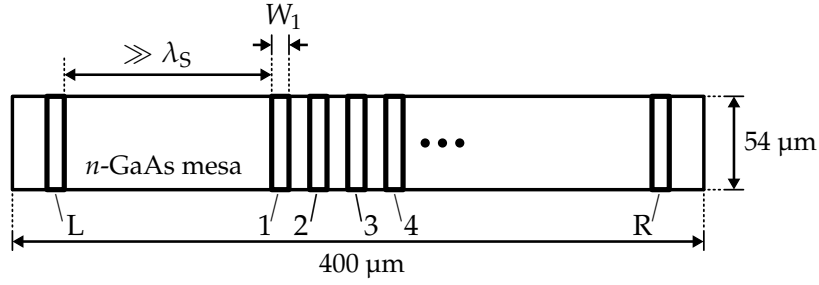


Figure 4.2: Schematic diagram of a spin transport device. W_1 is the width of the ferromagnetic contact 1. The spacing between the outer (L and R) and inner (1, 2, 3, 4, ...) contacts is much larger than the spin relaxation length λ_S . The number of inner contacts varies between the samples.

4.3 Ferromagnetic metal/*n*-GaAs contacts

In this section, it is demonstrated that the current flow into and out of the investigated ferromagnet/semiconductor contacts is laterally homogeneous, which is a prerequisite for the adequacy of the method used afterwards to determine interface voltages. In addition, it is shown that the current-voltage characteristics can be understood in the framework of the standard theory of field emission, and it is concluded that the overall behavior of the contacts is in accordance with the design of the structures.

4.3.1 Potential distribution below the contact

For the electrical characterization of the metal/semiconductor contacts, the three-terminal arrangement of Fig. 4.3(a) is used. Compared to other contact resistance measurement techniques, this method has the advantage that it eliminates backgrounds from the series resistance of the semiconductor and does not necessitate an additional ohmic contact. However, a more thorough investigation of the spatial potential distribution below a biased contact proves worthwhile to confirm that the measured potential originates from a uniform interface voltage. This condition is met if the contact exhibits a large specific contact resistivity $\rho_c = R_c A$ with respect to the sheet resistance of the semiconducting channel R_{sh} .⁸⁸ R_c and A denote the resistance and area of the contact, respectively.

The measurement configuration can be regarded as a contact end resistance

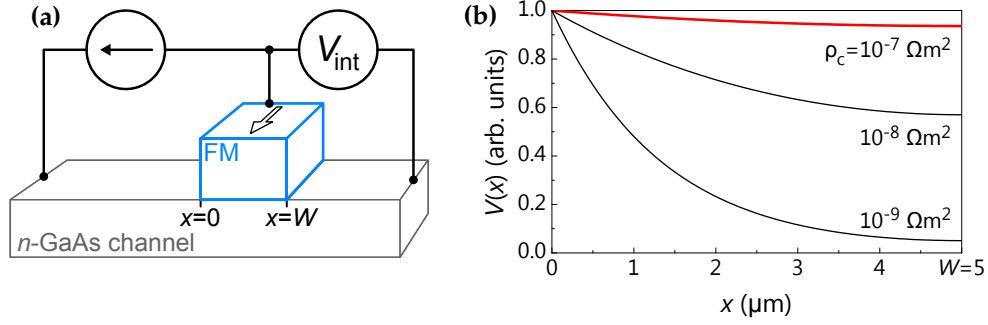


Figure 4.3: (a) Measurement geometry for the determination of the current-voltage characteristics of ferromagnet/semiconductor contacts. (b) Normalized potential distribution for indicated specific contact resistivities ρ_c , contact width $W = 5 \mu\text{m}$, and sheet resistance $R_{\text{sh}} = 540 \Omega/\square$.

(CER) test structure.⁸⁸ A detailed analysis has been carried out in Ref. 89 and yields the spatial distribution of the potential under the current-carrying contact,

$$V(x) = \frac{I\sqrt{R_{\text{sh}}\rho_c}}{W_y} \frac{\cosh[(W-x)/L_T]}{\sinh[W/L_T]}, \quad (4.1)$$

with current I , specific contact resistivity ρ_c , contact width W , contact length W_y , and transfer length⁸⁸

$$L_T = \sqrt{\rho_c/R_{\text{sh}}}. \quad (4.2)$$

For further analysis, it is useful to estimate the minimal contact resistance ρ_c of all investigated samples in the bias range of interest. To do so, current-voltage curves are measured in the geometry of Fig. 4.3(a). Note that the investigated Schottky contacts show a rectifying behavior so that ρ_c is a function of the current I . In addition, it is important to point out that the measured voltage in this geometry is determined by the potential at the contact end $V(W)$.⁸⁸ Of all investigated samples, a minimal resistance $V(W)/I$ of 400Ω is found in the forward-biased contacts of sample A1 at a current of $600 \mu\text{A}$. Using $V(W) \leq V(0)$ and the contact width and length for this sample, 5 and $54 \mu\text{m}$, respectively, one can estimate the specific contact resistivity to be at least $10^{-7} \Omega\text{m}^2$.

Note that this consideration neglects the resistance of the metallic layer. This omission constitutes a valid approximation because typical resistivities of epitax-

4.3 Ferromagnetic metal/*n*-GaAs contacts

ial metals are on the order of $\rho_{\text{FM}} = 10^{-7} \Omega\text{m}$ (e.g., Ref. 90) so that for a metal thickness on the order of $t_{\text{FM}} = 10 \text{ nm}$ one obtains $\rho_{\text{FM}} t_{\text{FM}} \ll \rho_{\text{c}}$.

Figure 4.3(b) shows the potential distribution according to equation 4.1 for different specific contact resistivities and a contact width of $5 \mu\text{m}$. The sheet resistance under the contact is approximated by the sheet resistance between the contacts, which is accessible by conventional four-point measurements and has been determined to be about $540 \Omega/\square$ at 20 K for all samples using alloyed ohmic AuGe contacts on a Hall bar structure. Clearly, for the estimated lower bound of $\rho_{\text{c}} = 10^{-7} \Omega\text{m}^2$, the spatial distribution can be considered homogeneous across the contact area. In this case, the transfer length exceeds the contact width, and the CER method yields

$$V_{\text{int}}/I = \rho_{\text{c}}/A \quad (4.3)$$

with a universal interface potential $V_{\text{int}} = V|_{x=W} \cong V|_{x=0}$.

4.3.2 Current-voltage characteristics

Figure 4.4 shows the current density $j = I/A$ as a function of V_{int} measured according to the geometry of Fig. 4.3(a) for samples A1, B, and C. All contacts exhibit a rectifying behavior as expected for metal/semiconductor Schottky contacts. Notably, only sample A1 shows an appreciable current density in the reverse direction. It is shown later that the resistance of the barrier with respect to reverse current flow is of crucial importance for the spin injection properties of the contact.

To gain further insight, the current-voltage characteristics can be analyzed using standard theory. Figure 4.5 shows a schematic diagram of the energy bands at a forward-biased metal/*n*-type semiconductor Schottky contact. Here, ϕ_{B} denotes the Schottky barrier height, V_{int} again describes the voltage applied to the interface, ξ_2 is the Fermi energy of the semiconductor with respect to the bottom of the conduction band, ϕ is the potential energy of the barrier, and E_{m} is the energy of the tunneling electrons.

Depending on the particular barrier shape and temperature of operation, different mechanisms are responsible for the electronic transport. At elevated temperatures, the main contribution to the current is the thermionic emission (TE) of elec-

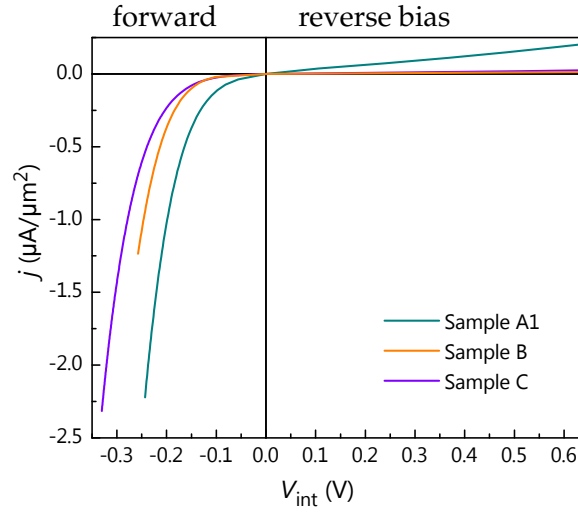


Figure 4.4: Current density j as a function of V_{int} for samples A1, B, and C at 20 K.

trons over the top of the barrier. However, for low temperatures and high doping levels, tunneling through the barrier dominates the transport. Thermionic-field emission (TFE) refers to the tunneling of electrons which upon thermal excitation reach an energy level where the barrier is sufficiently narrow. In degenerate semiconductors, field emission (FE) of electrons near the Fermi energy is a substantial contribution.

A rough criterion^{88,92} to determine the relevant transport mechanism involves a comparison of the thermal energy $k_{\text{B}}T$ to the tunneling parameter E_{00} , which is given by⁹¹

$$E_{00} = \frac{e\hbar}{2} \sqrt{\frac{N}{m^* \epsilon_s}}, \quad (4.4)$$

where e denotes the elementary charge, \hbar the reduced Planck constant, m^* the electron effective mass of the semiconductor, ϵ_s its permittivity, N the doping density close to the interface, k_{B} the Boltzmann constant and T the absolute temperature. The regimes are then defined as: $E_{00} \leq 0.5 k_{\text{B}}T$ for TE, $0.5 k_{\text{B}}T < E_{00} < 5 k_{\text{B}}T$ for TFE, and $E_{00} \geq 5 k_{\text{B}}T$ for FE.

The investigated spin transport structures are designed such that tunneling contributions are dominant in the temperature range of interest. The evaluation of

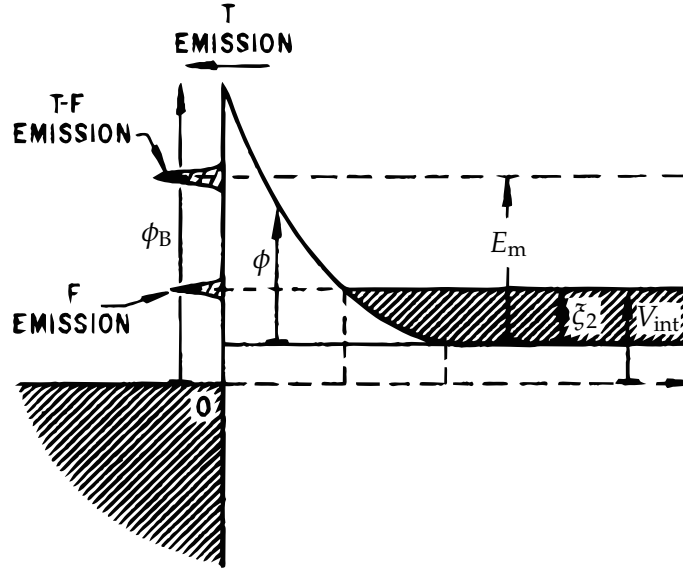


Figure 4.5: Potential energy diagram of a forward-biased Schottky contact with the metal on the left and the degenerately doped *n*-type semiconductor on the right side (from Ref. 91). T emission describes the thermionic emission of electrons over the barrier. F and TF indicate the tunneling contributions to the electronic transport, i.e., field emission and thermionic-field emission, respectively. The other labels are explained in the main text.

equation 4.4 using parameters of GaAs and a density of donors in the highly-doped interface region of $5 \times 10^{18} \text{ cm}^{-3}$ yields

$$E_{00} \cong 44 \text{ meV} ,$$

which is larger than $k_B T$ even at room temperature. As a consequence, in the investigated samples FE is expected to constitute the dominant transport process below about 100 K complemented by TFE for higher temperatures.

Padovani and Stratton⁹¹ derive expressions for the tunneling current contributions, which can be used to fit the current-voltage characteristics as shown in Fig. 4.6. For the forward-biased contact – that is for electron flow from the semiconductor into the metal, which is the relevant configuration for electrical spin

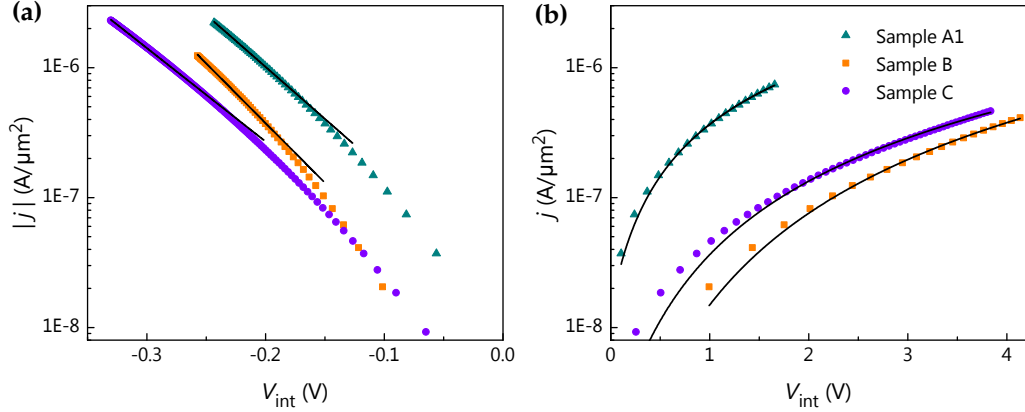


Figure 4.6: (a) Forward and (b) reverse current characteristics for samples A1, B, and C at 20 K. The solid lines are fits according to equations 4.5 and 4.6.

extraction – the current can be written as⁹³

$$j = j_s \exp [eV_{\text{int}} / (nk_B T)] \stackrel{\text{FE}}{=} j_s \exp (eV_{\text{int}} / E_{00}) . \quad (4.5)$$

j_s denotes the saturation current density and n the ideality factor. While the ideality factor generally accounts for all transport mechanisms and deviates from unity in the case of tunneling contributions, the term on the right-hand side constitutes the expression for the limit of pure field emission.⁹¹ As explained above, one can assume pure field emission for the investigated contacts at low temperatures, and the tunneling parameters E_{00} of 54 meV (sample A1), 47 meV (B), and 60 meV (C) obtained from the fitting of the forward-current characteristics at 20 K are all in reasonable agreement with the estimate from equation 4.4. However, a slight enhancement of the tunneling parameters is observed in the experiment as compared to the theoretical estimate, which possibly indicates additional tunneling paths through the barrier due to defect-assisted tunneling.⁹³

Electrical spin injection requires a reverse current, and the corresponding expression from Ref. 91 for low temperatures and $eV_{\text{int}} > \phi_B$ reads

$$j = A^* \left(\frac{E_{00}}{k} \right)^2 \frac{\phi_B - eV_{\text{int}}}{\phi_B} \exp \left(- \frac{2\phi_B^{3/2}}{3E_{00}(\phi_B - eV_{\text{int}})^{1/2}} \right) . \quad (4.6)$$

4.3 Ferromagnetic metal/*n*-GaAs contacts

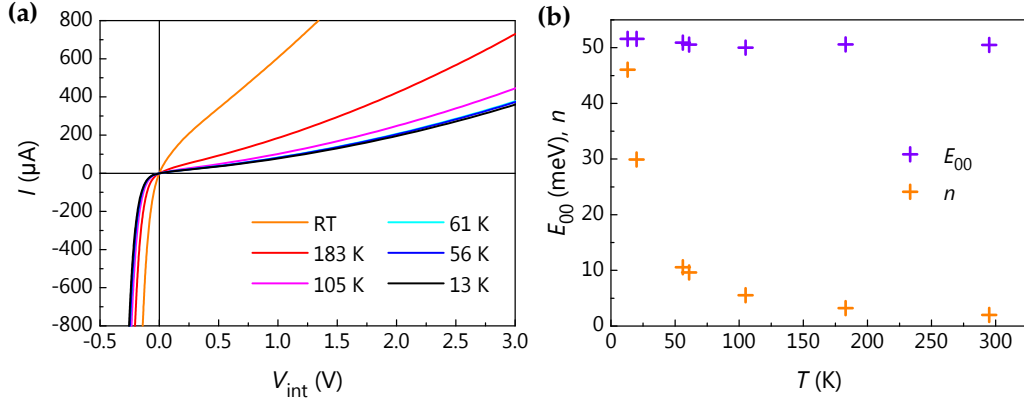


Figure 4.7: Temperature dependence of (a) the current-voltage characteristics and (b) the tunneling parameter E_{00} and ideality factor n extracted from the forward current according to equation 4.5 for sample A2. RT denotes room temperature.

By taking the value of E_{00} deduced above and treating the effective Schottky barrier height ϕ_B and the effective Richardson constant of the metal A^* as fit parameters, one obtains a satisfactory agreement with the experimental reverse-current density as shown in Fig. 4.6(b). From the fitting procedure, ϕ_B is determined to be 0.26 eV (sample A1), 0.61 eV (B), and 0.56 eV (C). The high leakage current in the reverse direction for sample A1 in comparison with samples B and C is directly reflected in the smaller effective Schottky barrier height, which will be shown to be advantageous for the spin injection properties of the contact. The origin of a reduction in ϕ_B can lie in an increased density of defects at the metal/semiconductor interface.⁹⁴

The temperature dependent current-voltage characteristics of sample A2 presented in Fig. 4.7(a) further support that field emission is the dominant transport mechanism in the devices. As seen from Fig. 4.7(b), the tunneling parameter deduced from the forward current according to equation 4.5 is essentially independent of temperature up to room temperature, which indicates that transport processes other than field emission are not relevant in this regime.^{91,93}

4.4 Non-local spin valve

In this section, the electrical spin generation and subsequent non-local detection of a spin accumulation in the semiconductor is discussed. The spin-induced voltages are investigated as a function of transport length, current, and perpendicular magnetic field. From this analysis, important sample properties such as the spin diffusion length and the spin lifetime of the channel are deduced. Furthermore, it is shown that the spin generation efficiency decreases with increasing interface bias, and possible physical origins of this decay are discussed. A consequence of this bias dependence is the fact that a larger area of the injector contact can lead to an enhanced range of operational currents for spin injection.

4.4.1 Non-local detection of a spin accumulation

To find evidence for electrical spin generation and detection in the investigated material system, measurements are carried out in the non-local spin valve configuration of Fig. 4.8(a). As explained in section 2.3.2, in this geometry an electrical current is driven across the interface between the left ferromagnetic contact and the semiconducting channel. Depending on the direction of current flow, spin injection or extraction occurs underneath this contact. The generated spin accumulation diffuses into all directions, and it is sensed non-locally by the right contact. The measured voltage depends on the relative magnetization orientation of the generating and detecting contacts.

Figure 4.8(b) shows the non-local voltage for sample A2 with a magnetic field applied along the easy axis of magnetization of the contacts. The measurement signal exhibits a transition between the parallel and antiparallel magnetization configuration, because the coercive fields of the two contacts are slightly different. The coercive fields can be determined from such curves and are found to be (2.1 ± 0.3) mT for sample A1, (3.2 ± 1.2) mT for sample A2, (1.9 ± 0.4) mT for sample B, and (11.9 ± 1.6) mT for sample C.

The peak at zero magnetic field is typically attributed to dynamic nuclear polarization (DNP),^{95–100} which occurs in GaAs at low temperatures. The spins of the nuclei can be oriented by the spin-polarized electrons, which exist in the semiconducting region due to the electrical spin generation. The strong magnetic field of

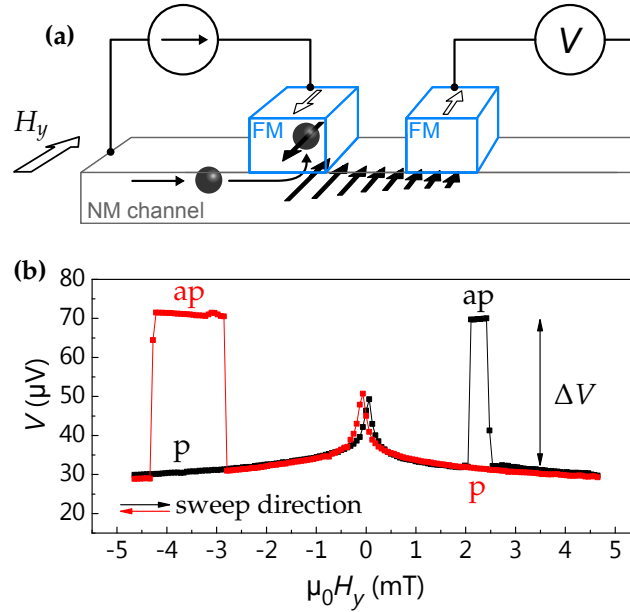


Figure 4.8: (a) Schematic representation of a non-local spin valve arrangement and (b) non-local voltage as a function of the magnetic field $\mu_0 H_y$ for sample A2 and a current of $-100 \mu\text{A}$ (spin extraction) at 20 K. ΔV denotes the voltage difference between the antiparallel (ap) and the parallel (p) magnetization configuration.

the spin-polarized nuclei, which is in general not parallel to the external magnetic field, in turn leads to a dephasing of the spins of the conduction electrons and hence to a peak in the non-local voltage when no field is applied. Upon application of the field along the easy axis of magnetization of the contacts, the precession axis of the electron spins is forced along the total magnetic field, which is a superposition of the nuclear and the external magnetic field. It follows that for large external fields the DNP effect is suppressed. In addition, an effective magnetic field induced by a finite roughness of the ferromagnet/semiconductor interface can also lead to spin dephasing when no external magnetic field is applied.¹⁰¹ The latter effect is closely related to the three-terminal inverted Hanle curves discussed in section 4.5.

Equation 2.12 presented in section 2.3.2 for the non-local voltage can be extended to account for geometrical corrections, which yields an expression for the spin-induced voltage $\Delta V = V_{\text{ap}} - V_{\text{p}}$ detected at a distance d from the spin gener-

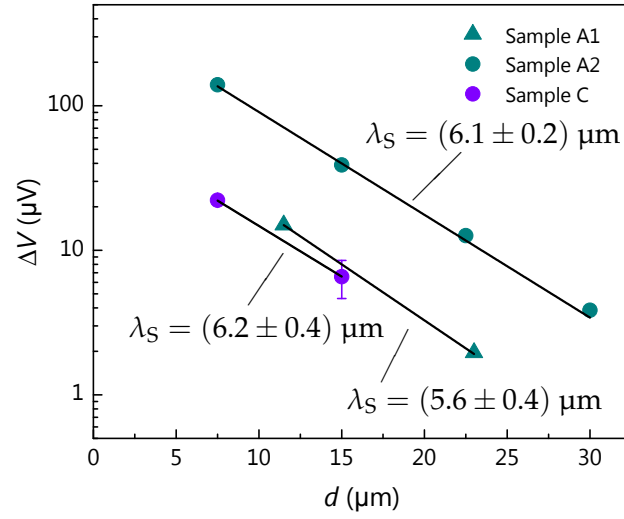


Figure 4.9: Spin-induced voltage ΔV as a function of center-to-center separation d between spin generation and spin detection. The measurement was performed at 20 K for spin extraction conditions with $I = -100 \mu\text{A}$ (sample A1), $-500 \mu\text{A}$ (A2), and $-200 \mu\text{A}$ (C). The solid lines represent the exponential decay according to equation 4.7.

ation point^{63–65}

$$\Delta V = -\frac{P_{\text{gen}}P_{\text{det}}\lambda_S\rho_N I}{S} \exp(-d/\lambda_S), \quad (4.7)$$

and describes the exponential decay of the spin accumulation with the characteristic length scale λ_S , which is the spin diffusion length. Furthermore, P_{gen} and P_{det} are the spin generation and spin detection efficiencies, respectively, and ρ_N and S are the bulk resistivity and the cross-sectional area of the semiconducting channel, respectively. V_p (V_{ap}) is the potential measured for the parallel (antiparallel) magnetization configuration.

λ_S can be determined from measurements using different contact separations as shown in Fig. 4.9. Because spin relaxation occurs in the semiconducting part of the structures, which is nominally the same for all samples, the values of λ_S are expected to agree, which is manifested in similar slopes for the samples in the representation of Fig. 4.9. The spin diffusion length at 20 K is found to be $(5.6 \pm 0.4) \mu\text{m}$ for sample A1, $(6.1 \pm 0.2) \mu\text{m}$ for sample A2, and $(6.2 \pm 0.4) \mu\text{m}$ for sample C. These results are in good agreement with reports of spin diffusion

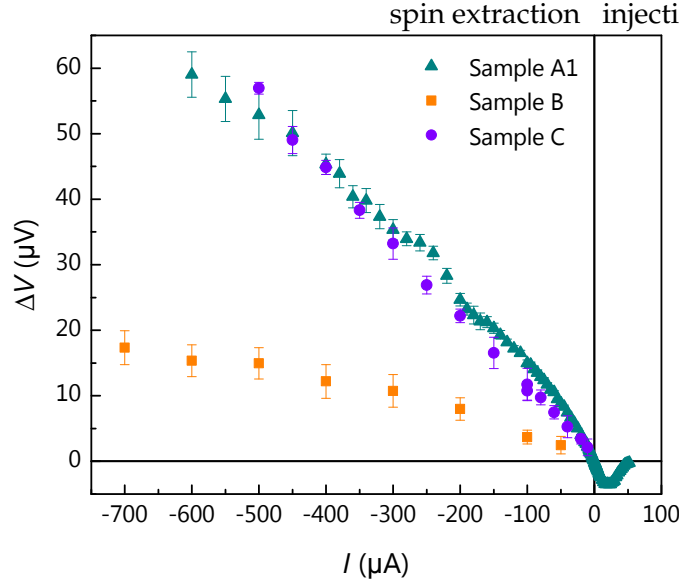


Figure 4.10: Non-local spin valve signal ΔV as a function of current for samples A1, B, and C at 20 K.

lengths in *n*-type GaAs channels with similar doping densities.^{62,64,102} Note that for sample B no device with varying contact separations was available.

The dependence of the non-local spin valve signal ΔV on the applied current is depicted in Fig. 4.10. Negative (forward) currents denote spin extraction conditions, while positive (reverse) currents correspond to spin injection. Notably, spin extraction is observed for all samples, but only sample A1 shows an appreciable spin-induced voltage for spin injection conditions. As expected, this spin signal exhibits an opposite sign as compared to the negative current region, indicating that the generated spin polarization for spin injection is the opposite of that for spin extraction. Also confirming one's intuition, the spin extraction signal increases with current in all three samples. Note that the similarity of the behavior of samples A1 and C is coincidental, which becomes clear when one considers that the spin transport lengths are different for all samples. More importantly, the spin injection signal for sample A1 does not behave monotonically, exhibiting a peak of roughly $-4 \mu\text{V}$ for $20 \mu\text{A}$. This finding is explained below by considering the current-voltage characteristics of the contact.

4.4.2 Hanle curves

The most straightforward way to manipulate the spin polarization during transport between the generating and detecting electrodes uses an external magnetic field, which is oriented perpendicular to the direction of the spin polarization. While this manipulation scheme is not practical for devices, it is widely regarded as a robust proof of spin transport. Due to the magnetic anisotropy, the in-plane magnetization of the ferromagnetic stripes is not affected for small fields applied perpendicular to the sample plane. However, a spin precession and dephasing of the conduction electrons in the semiconductor is induced. The resulting dependence of the non-local voltage on the out-of-plane magnetic field is referred to as a Hanle curve as explained in section 2.2.2.

Typically, Hanle curves are analyzed using the one-dimensional drift-diffusion model^{46,57,60,62,64} (see section 2.2.2), which yields the spin-induced non-local voltage

$$V = V_0 \int_0^\infty dt \frac{1}{\sqrt{4\pi Dt}} e^{-(d-v_d t)^2/(4Dt)} e^{-t/\tau_S} \cos(\Omega_L t), \quad (4.8)$$

with $V_0 = (\pm P_{\text{gen}} P_{\text{det}} I \lambda_S \rho_N / S)(\lambda_S / \tau_S)$, the Larmor precession frequency $\Omega_L = g \mu_B \mu_0 H_z / \hbar$, the spin diffusion coefficient D , the spin lifetime τ_S , and the g -factor for GaAs, $g = -0.44$. Because the detecting contact is located in the region of pure spin diffusion, the drift velocity v_d is set to zero for the non-local configuration. The plus (minus) sign corresponds to the parallel (antiparallel) magnetization configuration.

Figure 4.11 shows non-local Hanle curves for sample A2 using a parallel magnetization configuration and two different center-to-center contact spacings ($d = 7.5$ and $22.5 \mu\text{m}$). For this measurement, a lock-in technique is used, in which the forward current is modulated with a square waveform between 0 and $-100 \mu\text{A}$ at a modulation frequency of 137 Hz. The maximal spin signal is found at zero field, while for fields exceeding 20 mT the spin polarization at the detecting contact disappears. The fit lines are based on equation 4.8 and the relation

$$\lambda_S = \sqrt{D\tau_S} \quad (4.9)$$

as well as the known value for λ_S (Fig. 4.9). The best agreement with the exper-

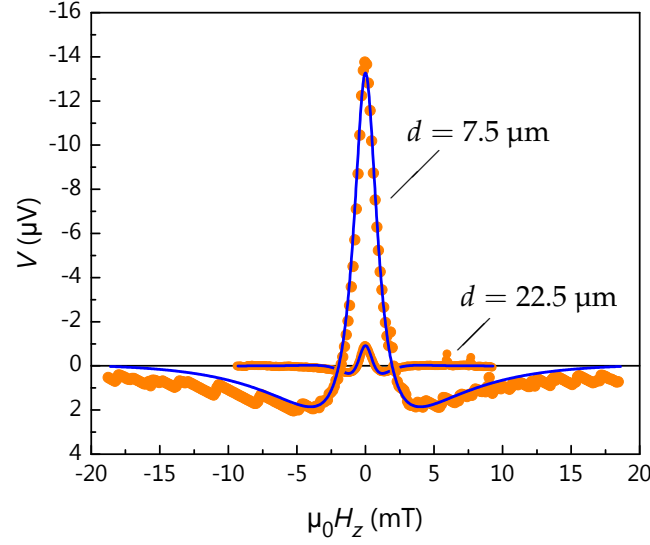


Figure 4.11: Non-local spin signal as a function of the out-of-plane magnetic field $\mu_0 H_z$ for spin extraction conditions and a parallel magnetization configuration (sample A2 at 20 K). The data are presented for two different contact spacings d . The blue fits are calculated according to equation 4.8 with $\tau_S = 28$ ns. Note that a linear background has been subtracted from the data.

imental data is achieved using a spin lifetime τ_S of 28 ns. This value falls into the range of previously reported spin lifetimes in n -type GaAs, which have been found to lie between 2 and 64 ns for a similar doping density at low temperatures.^{62–64,102–104}

From the spin lifetime, the spin diffusion coefficient can be calculated to be $13 \times 10^{-4} \text{ m}^2/\text{s}$, which is more than a factor of two larger than the charge diffusion coefficient $D_e = \mu k_B T / e$ of about $6 \times 10^{-4} \text{ m}^2/\text{s}$, as determined from Hall measurements at 20 K, where μ denotes the Hall mobility. On the one hand, differences between the spin and charge diffusivity have been previously reported.^{105–107} On the other hand, with the extent of ambiguity taken into account when spin lifetimes are determined from Hanle curves, the agreement is quite satisfactory. Some of the potential sources of error shall be discussed in the following. First, it is found that the estimation of the spin lifetime sensitively depends on the subtraction of the spin-independent background, which contributes to the raw measure-

ment data due to thermal drift. In fact, spin lifetimes between 20 and 30 ns are found in consecutive runs with similar initial conditions. Furthermore, it is known that other mechanisms can have an influence on the Hanle lineshape, such as a deviation from a perfectly perpendicular orientation of the field with respect to the spin polarization or a magnetic domain structure of the ferromagnetic contacts.⁹⁵ In addition, dynamic nuclear polarization^{95,96,100} as well as stray fields resulting from an interfacial roughness¹⁰¹ (cf. section 4.5) dephase the injected spin polarization. Finally, the extension from the one-dimensional to a two-dimensional drift-diffusion model was shown to yield a higher consistency of the measured spin lifetimes.¹⁰⁸

Altogether, the estimated spin lifetime of 28 ns is not to be treated as a precise value. However, the consistency with literature reports and qualitative agreement with the one-dimensional spin drift-diffusion model corroborates that the observed signals originate from the transport of spin-polarized electrons in the semiconductor.

4.4.3 Bias dependence of electrical spin generation

In this section, the knowledge of the contact $j(V_{\text{int}})$ -characteristics is brought together with the current dependence of the electrical spin generation to elucidate the bias dependence of spin generation.

Importantly, in the current dependence of the spin-induced voltage in the non-local configuration (cf. Fig. 4.10) a deviation of the spin signal from a linear behavior is observed. For further analysis, it is instructive to investigate the spin signal in terms of its bias dependence. Rewriting equation 4.7 yields

$$\left. \frac{\Delta V}{I} \right|_{V_{\text{int}}} = P_{\text{gen}}(V_{\text{int}}) \frac{P_{\text{det}} \lambda_S \rho_N}{S} \exp(-d/\lambda_S). \quad (4.10)$$

The term on the left-hand side is sometimes referred to as the non-local resistance. Note that the detecting contact is unbiased in the non-local arrangement so that P_{det} is constant. Thus, the bias dependence of the measurement signal reflects the bias dependence of the spin generation efficiency P_{gen} . λ_S was determined in section 4.4.1, and the other parameters can be inferred from conventional transport measurements (ρ_N) or are known geometrical factors according to the sample de-

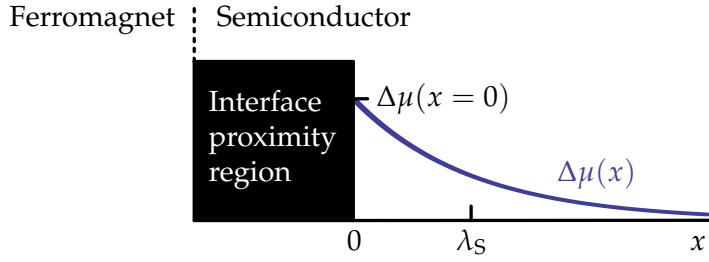


Figure 4.12: Schematic diagram showing a ferromagnet/semiconductor interface, where an electrically generated spin accumulation is reduced by initial processes inside an interface proximity region (represented by the black box), before the spin accumulation value $\Delta\mu(x)$ reaches the value given by the effective generation efficiency P_{gen} , $\Delta\mu(x = 0) = 2P_{\text{gen}}\rho_N\lambda_S j$ according to equation 2.2, and decays exponentially in space with the characteristic length λ_S .

sign (d and S).

In equation 4.10, P_{gen} is to be understood as the effective injection or extraction efficiency, which corresponds to the spin accumulation value $\Delta\mu(x = 0)$ before the occurrence of the purely diffusive lateral spin transport to the detecting contact. After $\Delta\mu(x = 0) = 2P_{\text{gen}}\rho_N\lambda_S j$ is reached, the spin accumulation value decays exponentially with a well-defined decay length λ_S . This concept is schematically shown in Fig. 4.12. In the one-dimensional framework, a spin accumulation is generated by spin injection or spin extraction at the ferromagnet/semiconductor interface. This spin accumulation is then reduced by spin relaxation processes inside an interface proximity region with an output spin accumulation value of $\Delta\mu(x = 0)$. Possible mechanisms that reduce the spin polarization in the proximity of the generating contact are explained below.

Figure 4.13 shows $P_{\text{gen}}P_{\text{det}}$ as a function of V_{int} for samples A1, B, and C. The values are obtained from equation 4.10 using the measured non-local resistances and a semiconductor bulk resistivity ρ_N of $8.4 \times 10^{-4} \Omega\text{m}$ deduced from conventional four-point conductivity measurements with alloyed ohmic AuGe contacts on a Hall bar structure at 20 K. For samples A1 and C, λ_S is taken from Fig. 4.9, while the spin diffusion length is assumed to be $6 \mu\text{m}$ for sample B, which is the average value of the other three samples. The cross-sectional area of the non-magnetic channel S is $81 \mu\text{m}^2$, and d is the known center-to-center spacing between the con-

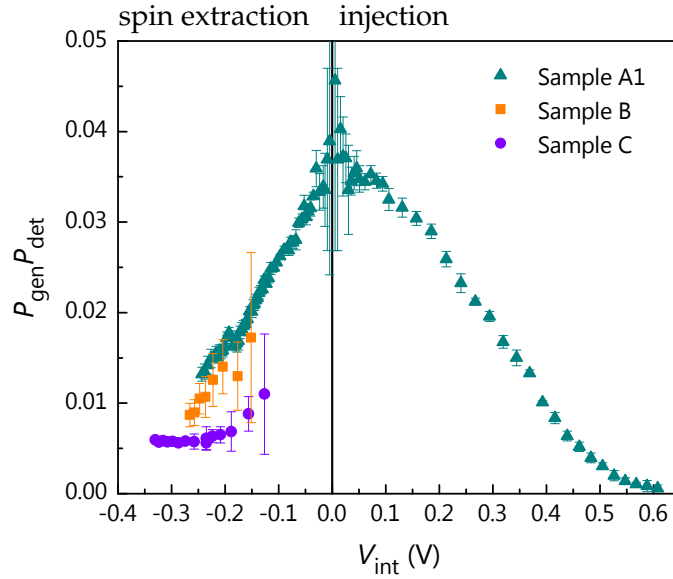


Figure 4.13: Interface-bias dependence of the product of the spin generation and spin detection efficiency for samples A1, B, and C at 20 K according to equation 4.10.

tacts.

From this consideration, a low-bias estimate of the spin injection efficiency can be given for sample A1. It is assumed that for zero bias P_{det} is equal to P_{gen} . Then the spin injection efficiency is estimated to be about 19.5%. This value roughly accords with previously reported values in non-local spin transport devices using similar Schottky contacts to *n*-type GaAs. At low temperatures, an injection efficiency of 16% has been obtained for Co_2FeSi ⁶⁴ and Fe ⁶² contacts, while 20% has been observed for CoFe contacts.¹⁰³

Values of the effective injection efficiency are available for interface biases ranging from spin extraction to spin injection conditions for sample A1. Note that a constant injection efficiency would imply that the induced spin polarization scales linearly with the applied current. However, P_{gen} is seen to decay both with forward and reverse bias. While the low-bias value is approximately equal for spin injection and extraction, the decay is more rapid for extraction. In the experimental situation, the interface bias applicable in the forward direction is limited by the height of the Schottky barrier. With a vanishing height of the effective energy

4.4 Non-local spin valve

barrier, other circuit elements dominate the series resistances and voltage drops so that high and potentially damaging currents would be necessary to reach a higher V_{int} in the forward direction than shown. In the reverse direction, P_{gen} can be observed to be reduced to less than 10% for a bias of 0.5 V. All in all, efficient electrical spin generation is limited to small interface biases.

A bias dependence of the spin injection efficiency has been presented in the literature for spin LEDs^{109,110} and for spin injection experiments both in the three-terminal^{19,50,54} and non-local geometries, including reports of a sublinear increase of the spin-induced non-local voltage with current^{83,111,112} or a decay of P_{gen} with increasing forward and reverse bias.^{63,103,113,114} However, the reasons for this behavior have not always been unambiguously identified. In the following, physical mechanisms that are potentially responsible for the decay of P_{gen} with bias are discussed. These can be grouped into processes which have an influence on the actual polarization of the tunneling current across the Schottky barrier on the one hand and spin relaxation mechanisms in the semiconductor on the other hand. The latter essentially occur in the interface proximity region of Fig. 4.12.

Naturally, the spin polarization of the tunneling current depends on the spin-dependent band structure of the ferromagnet.^{115,116} For a forward-biased contact, electrons can tunnel from the semiconductor into excited states of the ferromagnet. Then, the energy dependence of the spin-dependent density of states above the Fermi level generally leads to an increase or decrease of the spin extraction efficiency with bias. In fact, a decay of the spin polarization in Fe₃Si with increasing energy can be found by comparing the calculated density of states for the two spin channels presented in Ref. 117. Consequently, the influence of the band structure on the spin extraction process can be identified as the likely cause for the decay of the extraction efficiency with increasing forward bias. However, for reverse bias, the spin polarization at the Fermi energy should dominate the spin injection process due to the increasing thickness of the Schottky barrier with lower energy. Even when contributions from the spin polarization below the Fermi energy are assumed to be relevant, the strong decay of the injection efficiency with reverse bias cannot be explained.

Furthermore, it has been pointed out that the bias dependence of the contact resistivity has to be considered for non-ohmic contacts. For a rectifying Schot-

tky contact, the specific contact resistivity decreases with forward bias due to a decrease in the barrier height and a narrowing of the space-charge region. A decrease of the barrier resistance has been identified to lead to a decrease in the spin injection efficiency because of the feedback (cf. section 2.1) of the spin accumulation on the spin current.^{36,118,119} However, the investigated contacts in this thesis are too resistive to be affected by the feedback problem as addressed in section 4.6.

In addition, spin relaxation processes in the interface proximity region shown in Fig. 4.12 can lead to a reduction of the effective injection efficiency. The contact is electrically biased so that the injected electrons have to traverse a region of electric fields. One possible reason for the decay of P_{gen} with bias is the stronger Dyakonov-Perel spin relaxation for larger k vectors.^{120,121} This effect has been identified as the reason for a reduction of the electroluminescence polarization in spin LEDs with increasing reverse bias.^{122,123}

It has also been discussed that for a high reverse bias electrons can tunnel from the ferromagnet into bands other than the Γ -valley of GaAs, namely the L - and X -valleys, which exhibit short spin lifetimes.^{118,124} In fact, as pointed out in Ref. 83, the spin injection efficiency is expected to decay for interface voltages beyond 300 mV.

Finally, Joule heating of the semiconductor in the region of current flow can lead to a reduction of the spin lifetime. The spin lifetime is expected to decrease with temperature.^{31,108} This effect is asymmetric with interface bias due to the rectifying behavior of the contact so that the dissipated electrical power is smaller for a given positive V_{int} than for $-V_{\text{int}}$. A decay of P_{gen} can be expected for forward and reverse bias, and Joule heating would be in accordance with the experimental observation of a faster decay for spin extraction as compared to the decay for spin injection in Fig. 4.13. This mechanism would lead to a reduction of the spin lifetime with increasing interface bias, which will be ruled out experimentally in section 4.5.

The representation of Fig. 4.13 is useful for a comparison of the extraction efficiencies of the different samples. For example, one can conclude that, regardless of the degree of crystal ordering, Fe_3Si yields a higher value of $P_{\text{gen}}P_{\text{det}}$ than Co_2Fe for a given interface bias. However, in terms of the detectability of the signal, it is desirable to obtain a large absolute signal ΔV for a given current I in the repre-

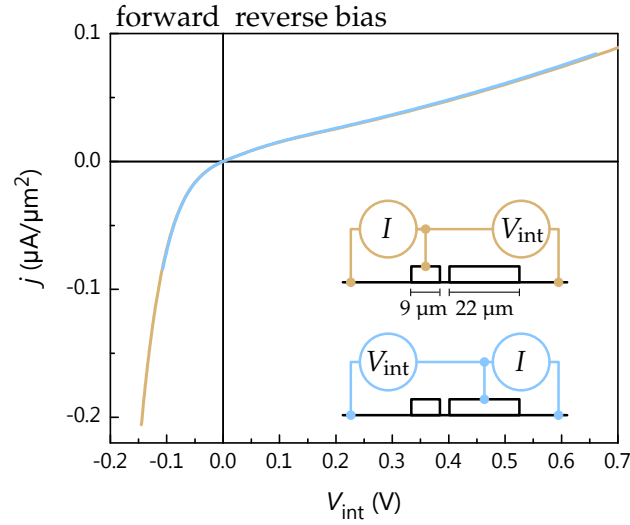


Figure 4.14: Current density as a function of interface voltage for sample A3 at 20 K and the geometries shown in the inset.

sensation of Fig. 4.10. For a given bias-dependent generation efficiency, the ΔV - I relationship can on the one hand be tuned by a modification of the geometrical factors such as the spacing between the contacts according to equation 4.10. On the other hand and more importantly, a modification of the current-voltage characteristics can lead to an improvement of the ΔV - I characteristic. In the following section, it will be shown that increasing the contact area constitutes a feasible way to tune the current-voltage characteristics in order to obtain larger spin-induced voltages for a given current.

4.4.4 Influence of contact area

The above results have important implications concerning the spatial dimensions of the spin injector and their influence on the operation of spin valve devices. Since the injection efficiency strongly decays with increasing reverse bias (see data for sample A1 in Fig. 4.13), the operation at small V_{int} is a prerequisite for the observation of large spin-induced signals. However, ΔV is proportional to the current I (cf. equation 4.10). Consequently, a contact with a larger area A – providing a higher current for moderate potential drops across the interface – should allow for the observation of spin injection over a wider current range. This hypothesis is

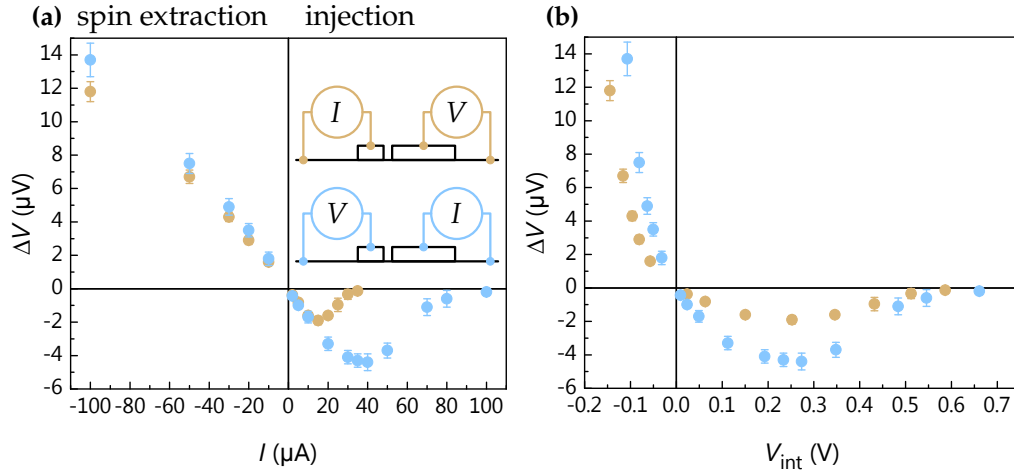


Figure 4.15: (a) Current and (b) interface bias dependence of non-local spin valve signal for sample A3 at 20 K for the geometries depicted in the inset.

experimentally confirmed in this section.

The investigated sample is a device from the same wafer as samples A1 and A2 and is in the following referred to as sample A3 (see Table 4.1). It comprises two Fe_3Si contacts in close proximity, one 9 μm , the other 22 μm wide as shown in the inset of Fig. 4.14. Except for their widths, the two contacts are nominally the same by design. As expected, the $j(V_{int})$ -characteristics are nearly identical, which confirms that the electrically active area of the contact coincides with the geometrical contact area, in accordance with the estimate made in section 4.3.1.

The non-local spin valve signal ΔV is shown as a function of applied current in Fig. 4.15(a) for the geometries depicted in the inset. Clearly, the performance is improved for spin generation with a larger contact area, which yields signals of an increased magnitude and spin injection over a wider current range. In particular, the maximum of the spin injection signal is shifted from about 15 μA for the small contact to about 40 μA for the large contact.

Figure 4.15(b) displays the same measurement signal as a function of interface voltage V_{int} across the biased contact, as inferred from Fig. 4.14. Note that the maximum of the spin injection signal is observed at the same interface bias of about 200 to 300 mV for both measurement geometries. This finding corroborates that V_{int} rather than I is the crucial parameter when physical mechanisms related

4.5 Detection of a spin accumulation in the three-terminal geometry

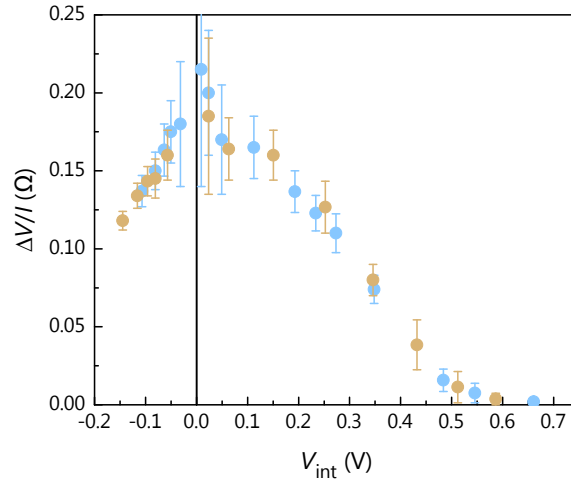


Figure 4.16: $\Delta V/I$ as a function of interface bias for the geometries shown in the inset of Fig. 4.15(a).

to the spin generation efficiency are studied.

The non-local resistance $\Delta V/I$, which is proportional to the effective injection efficiency according to equation 4.10, is shown in Fig. 4.16 as a function of interface bias. It is expected that the injection efficiency, being independent of the contact size, coincides, because the contacts differ only in their widths. Indeed, the same behavior is found for both measurement geometries. This finding clearly shows that, for a given injection efficiency, larger non-local spin valve signals can be obtained by increasing the size of the spin generating contact.

4.5 Detection of a spin accumulation in the three-terminal geometry

This section deals with the all-electrical generation and detection of a spin accumulation in the three-terminal geometry. The intention behind these measurements is to gain more insight into the bias-dependence of the spin generation efficiency and spin relaxation processes close to the interface. As explained in section 2.3.1 and in contrast to the non-local geometry, the spin accumulation value right at the ferromagnet/semiconductor interface¹⁰¹ and in interface states⁴⁷ is accessible by

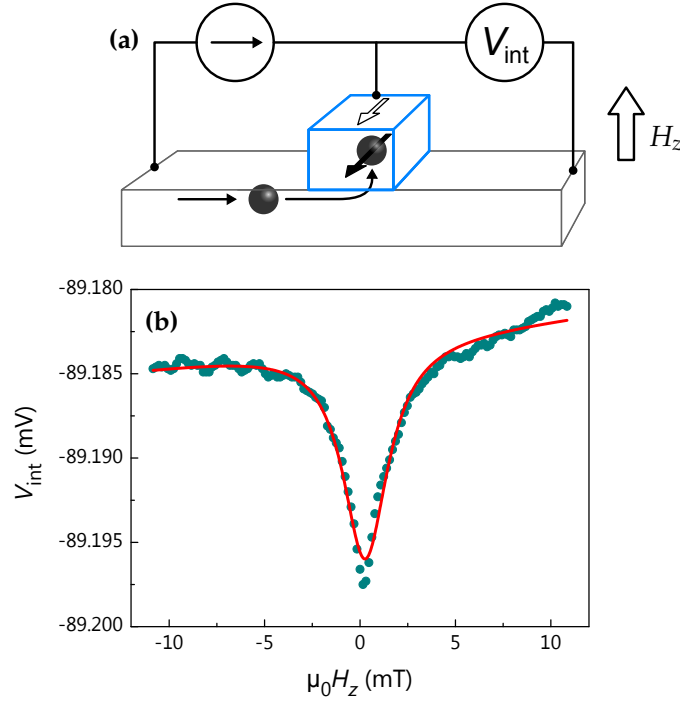


Figure 4.17: **(a)** Schematic representation of the measurement geometry used for three-terminal spin generation and detection. **(b)** Interface voltage as a function of the out-of-plane magnetic field $\mu_0 H_z$ for sample A2 at 20 K and spin extraction conditions with a current of $-30 \mu\text{A}$. The spin accumulation leads to a Hanle voltage with a field dependence which can be approximated by a Lorentzian curve (red) according to equation 4.11.

three-terminal measurements. Hanle curves are obtained for spin extraction conditions, and the inferred bias dependencies of the spin lifetime and the magnitude of the spin signal are investigated. In addition, the results are compared to the expectation from theory.

The measurement geometry for the three-terminal generation and detection of a spin accumulation is shown in Fig. 4.17(a) and coincides with the arrangement used for the determination of the $j(V_{\text{int}})$ -characteristics in section 4.3.2. The same ferromagnetic contact is used for the generation and for the detection of the electrically generated spin accumulation so that this geometry can be regarded as the limiting case of the non-local arrangement with zero separation between the spin generating and detecting contacts ($d = 0$). The current flow leads to a spin accu-

4.5 Detection of a spin accumulation in the three-terminal geometry

mulation underneath the ferromagnetic contact. A perpendicular magnetic field induces a spin precession and dephasing, which is manifested in a decrease of the interface voltage with increasing magnetic field. In contrast to the non-local Hanle measurements presented in section 4.4.2, the perpendicular field does not lead to a sign reversal of the ensemble-averaged spin polarization, because no defined average distance between the points of spin generation and spin detection exists.

As described in section 2.3.1, the reduction of the chemical potential splitting as a function of field leads to an approximately Lorentzian line shape given by¹⁹ (see equation 2.11)

$$\Delta\mu(H_z) = \frac{\Delta\mu(H_z = 0)}{1 + (\Omega_L \tau_S)^2}, \quad (4.11)$$

where $\Delta\mu(H_z)$ and $\Delta\mu(H_z = 0)$ are the spin accumulations with and without an applied magnetic field, respectively, and Ω_L again denotes the Larmor precession frequency, $\Omega_L = g\mu_B\mu_0 H_z/\hbar$. As shown in equation 2.10, $\Delta\mu(H_z = 0)$ is related to the spin-induced part of the interface voltage as¹⁹

$$\Delta\mu(H_z = 0) = \frac{2\Delta V_{\text{int}}}{P_G} \quad (4.12)$$

with the tunnel spin polarization P_G .

A measurement of V_{int} as a function of the out-of-plane magnetic field is shown in Fig. 4.17(b) for sample A2 and spin extraction conditions. The solid line represents a Lorentzian fit, which allows for a linear background. From the fitting procedure, ΔV_{int} as well as τ_S can be obtained and are shown in Fig. 4.18.

The spin resistance-area product (spin-RA) $\Delta V_{\text{int}}/j$ is presented in Fig. 4.18(a) and is seen to decrease with forward bias. In contrast to the non-local geometry the detecting contact is biased in the three-terminal geometry. Consequently, the results in Fig. 4.18(a) reflect the bias dependencies of the efficiencies of spin generation as well as spin detection. For small bias, the decay of the spin signal is faster than in the non-local geometry (cf. Fig. 4.13). This is expected, if the efficiency of the detection also decreases with bias. However, in the higher forward bias region ($V_{\text{int}} \lesssim -0.2$ V), the spin-RA depends only weakly on bias.

In contrast to the non-local geometry, no spin-induced signals could be observed for the three-terminal geometry using spin injection conditions. The reasons are twofold: First, the absolute signals are small for spin injection, because efficient

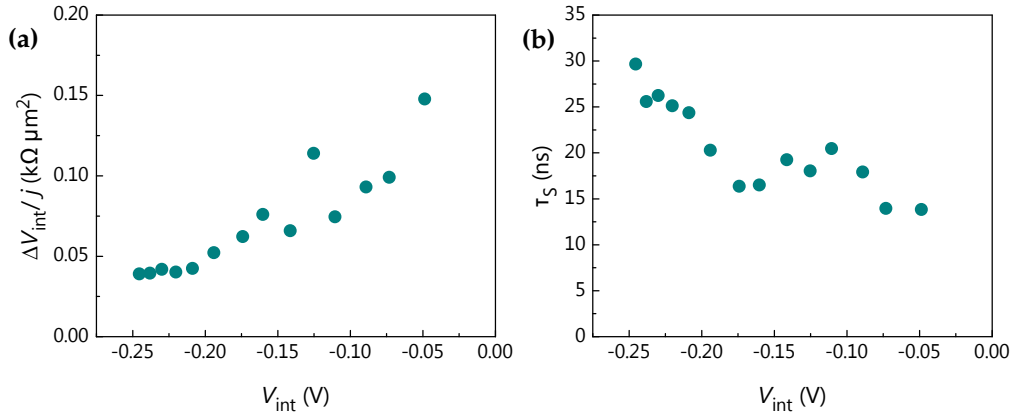


Figure 4.18: (a) Three-terminal spin signal and (b) spin lifetime versus interface bias for sample A2 derived from Lorentzian fits according to equation 4.11.

spin injection is limited to the small forward bias region only (cf. Fig. 4.10), and second, the large contact resistance of the reverse-biased Schottky contact leads to a large background signal in the interface voltage. Therefore, the absolute voltage noise is substantially stronger in the positive voltage range, preventing the observation of Hanle curves.

From the Hanle curves, the spin lifetime can be extracted. As seen from equation 4.11, the width of the Hanle curve is inversely proportional to τ_s . Figure 4.18(b) shows the spin lifetime as a function of the interface bias. The measured spin lifetime is found to lie between 13 and 30 ns, depending on the bias conditions. These values agree well with the lifetime of 28 ns estimated from the non-local spin valve measurements in section 4.4.2, especially when one considers that some ambiguity¹⁹ exists when lifetimes are determined from three-terminal Hanle curves.

Due to the fact that the spin lifetime is not found to decrease with forward bias, Joule heating can be ruled out as the cause of the decay of the spin generation efficiency with bias (see discussion in section 4.4.3). In addition, the agreement of the spin lifetimes deduced from the three-terminal and non-local measurements is in accordance with the previous assumption that the decay of the spin generation efficiency with forward bias (spin extraction) is not related to spin relaxation processes in the interface proximity region, as opposed to the proposed mechanisms

4.5 Detection of a spin accumulation in the three-terminal geometry

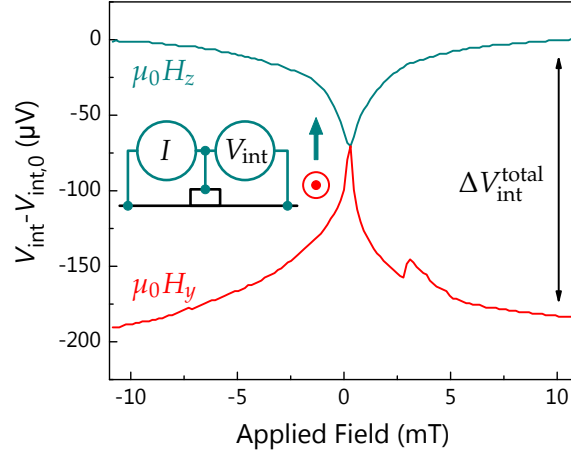


Figure 4.19: Three-terminal Hanle and inverted Hanle curves with a magnetic field applied perpendicular to the sample plane ($\mu_0 H_z$) and along the easy axis of magnetization ($\mu_0 H_y$), respectively, for sample A2, a current of $-200 \mu\text{A}$, and a temperature of 20 K. A constant background voltage $V_{\text{int},0}$ has been subtracted. $\Delta V_{\text{int}}^{\text{total}}$ denotes the maximal spin-induced voltage and amounts to $183 \mu\text{V}$.

leading to the decay of P_{gen} for injection conditions. Rather, the decay of the extraction efficiency is likely related to a true decay of the tunnel spin polarization P_G due to a reduction of the band structure polarization within the ferromagnetic metal.

Various articles report on a bias dependence of the spin lifetime in the proximity of an interface with a ferromagnetic metal, including reports of a slight increase with forward voltages,^{51,125} similar to the observation of Fig. 4.18(b). A possible explanation is given in Ref. 51, which is related to the conduction band edge variation with bias. More precisely, a forward bias reduces the height of the Schottky barrier and the strength of the electric field close to the interface. As a consequence, the Dyakonov-Perel spin relaxation mechanism becomes less effective, which results in an increased spin lifetime.

Figure 4.19 shows a comparison of V_{int} for different magnetic field directions. As before, a field sweep in the out-of-plane direction results in a dip in the interface voltage at zero field. A sweep in the in-plane direction along the easy axis of magnetization also results in a strong field dependence. However, the sign of the

field dependence is inverted. Hanle curves for in-plane field sweeps have been frequently reported for three-terminal measurements^{50,53,101,126} and are referred to as inverted Hanle curves.

The occurrence of an inverted Hanle curve has been explained by a finite roughness of the interface between the ferromagnetic metal and the adjacent non-magnetic layer.¹⁰¹ This roughness leads to magnetic fringe fields in the semiconductor, which decay with distance from the interface. If a spin accumulation exists close to the interface, spin precession in the fringe fields results in spin dephasing. As a consequence, even the spin signal which is measured at zero field is reduced. Upon application of a magnetic field along the easy axis of magnetization, however, the precession axis is forced along that direction, and the effect of the rough interface is suppressed.

Another possible reason for the apparent dephasing at zero field is the precession of the electron spins in the magnetic field of polarized nuclei. As discussed before, this is the effect that a peak at zero magnetic field in non-local spin valve measurements in GaAs at low temperatures is typically ascribed to^{62,63} (section 4.4.1). In addition, a combination of the two effects is possible.

Looking at Fig. 4.19, one finds that the dephasing is substantial. At large $\mu_0 H_y$, the spin accumulation reaches its maximal value, and it is reduced to little more than one third of this value for zero field. The difference between the high-field values of the Hanle and the inverted Hanle curve labeled $\Delta V_{\text{int}}^{\text{total}}$ is the value that should be compared to the standard theory,¹⁶ which does not take the described additional spin dephasing processes into account.

The expected spin signal in the three-terminal configuration according to the standard theory can be deduced by combining equations 2.2 and 2.10, and is written as

$$\Delta V_{\text{int}}/j = (P_G)^2 \rho_N \lambda_S . \quad (4.13)$$

In addition, a geometrical correction applies for situations other than $\lambda_S \gg (W, w)$, that is, for a spin diffusion length which is larger than the contact dimensions. Taking the geometrical correction for thin channels into account,³³ one obtains

$$\Delta V_{\text{int}}/j = (P_G)^2 \rho_N \lambda_S W/w , \quad (4.14)$$

4.5 Detection of a spin accumulation in the three-terminal geometry

with w denoting the channel thickness and W the contact width. Note that this expression is equivalent to equation 4.7 for the spin signal in the non-local case. In this sense, the three-terminal spin detection scheme constitutes the limiting case of the NLSV with a contact separation which goes to zero.

Taking the low-bias value of $P_{\text{gen}}P_{\text{det}}$ from Fig. 4.13 for $(P_G)^2$, one can estimate the expected spin signal in the three-terminal geometry as $\Delta V_{\text{int}}/j \cong 0.5 \text{ k}\Omega/\mu\text{m}^2$ using equation 4.14. This estimated value is larger than the measured $\Delta V_{\text{int}}^{\text{total}}/j$ of $0.2 \text{ k}\Omega/\mu\text{m}^2$ as seen from Fig. 4.19, and the discrepancy can be attributed to the bias dependence of the extraction efficiency. This overall consistency between the measured and estimated values is in contrast to many previous reports of spin generation experiments in the three-terminal geometry. Frequently, an enhancement of the measurement signal with respect to the theoretical estimate based on equation 4.13 of several orders of magnitude is observed.^{19,47,49,50,54,55} An explanation is given in the form of a two-step tunneling process via localized interface states close to interface between the tunnel barrier and the semiconductor^{47,127,128} or by an underestimation of the electrically active area of the contact.¹⁹

Since in this work experiments in different geometries are performed on a single device, a direct confirmation that the spin signals observed in the three-terminal geometry originate from a spin accumulation in the conduction band of GaAs and not from interface states can be achieved by comparing the three-terminal signal with the non-local signal. The non-local geometry requires spin transport via itinerant electrons between the generating and the detecting contacts so that a spin accumulation in localized states is not relevant. For a contact spacing d of $7.5 \mu\text{m}$ and a current of $-200 \mu\text{A}$, a non-local voltage of $56 \mu\text{V}$ is measured for sample A2 (measurement not shown), which can be extrapolated to the three-terminal limit by multiplication with the factor $\exp(d/\lambda_S)$. This procedure yields an expected three-terminal signal (due purely to a spin accumulation in the conduction band) of $191 \mu\text{V}$, which agrees well with the measured three-terminal signal $\Delta V_{\text{int}}^{\text{total}} = 183 \mu\text{V}$ from Fig. 4.19. Furthermore, this agreement shows once more that, for the used bias and magnetic field conditions, the effective spin generation efficiency P_{gen} is approximately equal to the tunnel spin polarization P_G so that spin relaxation processes in the interface proximity region of Fig. 4.12 are of minor importance.

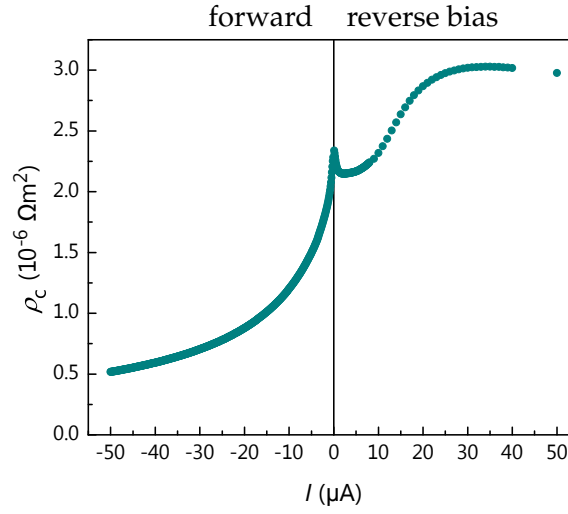


Figure 4.20: Specific contact resistivity ρ_c as a function of current applied to the ferromagnet/semiconductor junction of sample A2 at 20 K.

All in all, one can be confident that in the presented three-terminal measurements the spin voltage truly stems from a spin accumulation of the conduction band electrons rather than from a spin accumulation in localized interface states. This conclusion is drawn from a comparison of the spin lifetimes and the magnitudes of the spin signals in the non-local geometry with measurements in the three-terminal geometry.

4.6 Local spin valve

In this section, the all-electrical spin injection and detection in the local spin valve arrangement is discussed. It is shown that the results of the previous sections have implications for the operation in this technologically relevant geometry, which is characterized by two back-to-back Schottky contacts. To emphasize the importance of the spin injecting contact, Fig. 4.20 depicts the specific contact resistivity measured in the three-terminal geometry according to equation 4.3 as a function of current for sample A2. The rectifying behavior of the contacts is seen from the asymmetry with respect to the direction of electron flow. Therefore, the series resistance of the local spin valve circuit is dominated by the reverse-biased con-

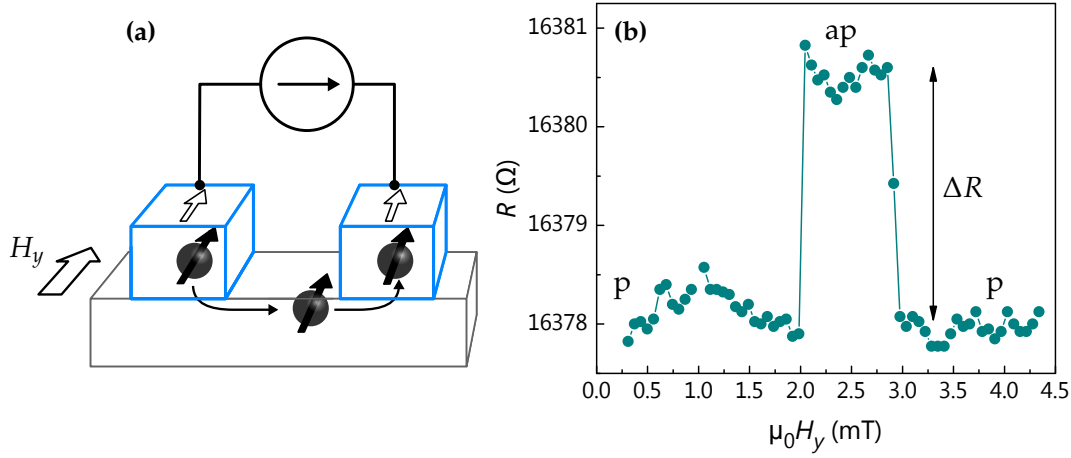


Figure 4.21: (a) Schematic diagram of a local spin valve arrangement and (b) local resistance as a function of magnetic field $\mu_0 H_y$ for sample A2 and a constant applied current of 4 μA at 20 K. ΔR denotes the difference in resistance between the antiparallel (ap) and the parallel (p) magnetization configuration.

tact, which can result in adverse bias conditions for spin injection as the injection efficiency decreases with interface bias (cf. section 4.4.3). As shown below, the resulting current window for local spin valve operation can be directly inferred from the bias dependence of the spin injection efficiency.

The local spin valve geometry is depicted in Fig. 4.21(a). A measure of the spin signal in this configuration is the magnetoresistance ratio $\text{MR} = \Delta R / R_p$, with $\Delta R = R_{\text{ap}} - R_p$ and R_{ap} (R_p) denoting the resistance in the antiparallel (parallel) magnetization configuration. As pointed out in section 2.3.3, the interface resistances play a major role for the performance of such a device. On the one hand, a sizable interface resistance is needed to overcome the conductivity mismatch or feedback problem. On the other hand, if the interface resistance is too large, the dwell time of the electrons in the channel becomes comparable to the spin relaxation time, and the magnetoresistance signal is small.

As explained in section 2.3.3, an expression of the MR is given in Ref. 33 for a local spin valve in a current-perpendicular-to-plane geometry. This geometry differs from the geometry used in the investigated lateral spin transport structures. Nonetheless, it is instructive to make use of this formula to gain insight into the

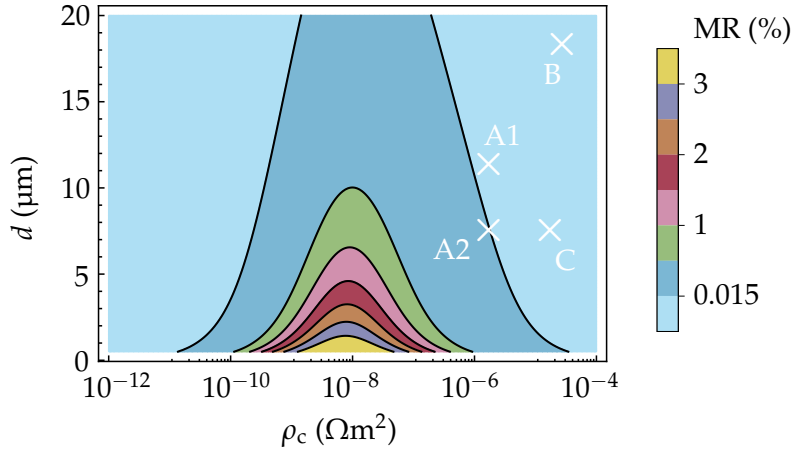


Figure 4.22: Visualization of the magnetoresistance for a local spin valve structure operated in the current-perpendicular-to-plane geometry according to the equations given in Ref. 33 with the known parameters for sample A2: $P_{\text{gen}} = 0.2$, $\lambda_S = 6.1 \times 10^{-6} \mu\text{m}$, and $\rho_N = 8.4 \times 10^{-4} \Omega\text{m}$. The crosses mark the conditions corresponding to the investigated samples, as indicated.

expected performance of these devices. Taking the values $2.3 \times 10^{-6} \Omega\text{m}^2$ for ρ_c as seen from Fig. 4.20 and the spin diffusion length $\lambda_S = 6.1 \mu\text{m}$ as the value of the spin drift length as well as a spin injection efficiency P_{gen} of 20% (all values obtained in the previous sections at low bias for sample A2), one can plot the expected MR as a function of the specific contact resistivity and the transport length as shown in Fig. 4.22.

The magnetoresistance ratio is seen to increase with smaller transport length, and an optimum of the specific contact resistivity is found at about $10^{-8} \Omega\text{m}^2$. For larger values of ρ_c , the MR decays rapidly. The maximal magnetoresistance ratio of $P_{\text{gen}}^2 / (1 - P_{\text{gen}}^2) \approx 4\%$ is expected for transport lengths below a few hundred nanometers. The conditions for the actual samples (specific contact resistivity at low bias and transport length d) are visualized in the form of crosses in Fig. 4.22. Clearly, the contacts of all samples are found to be too resistive to yield an optimal spin signal in the local configuration. Nonetheless, a small but detectable MR of 0.015% is expected for sample A2.

The lateral transport geometry of Fig. 4.21(a) requires a geometric correction,^{32,33} which leads to a shift in the window of appreciable magnetoresistance (see equa-

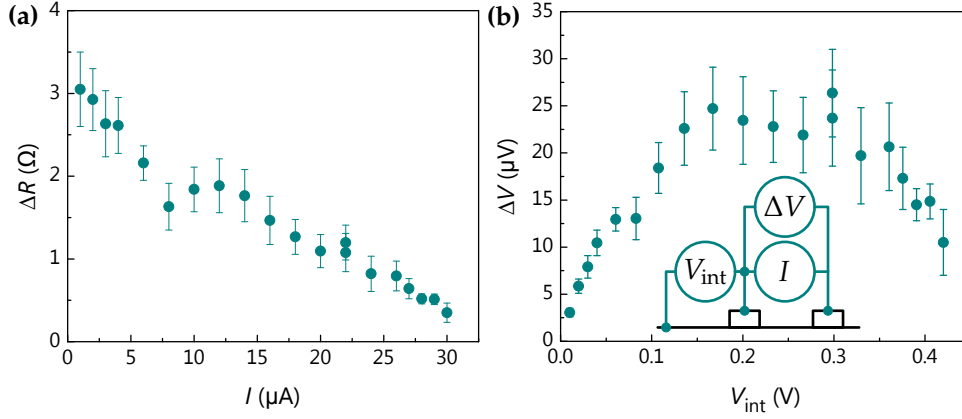


Figure 4.23: (a) Change in local spin valve resistance $\Delta R = R_{ap} - R_p$ as a function of the applied current I and (b) interface-bias dependence of $\Delta V = V_{ap} - V_p$. The inset shows the measurement geometry for the determination of V_{int} , which is the voltage drop across the reverse-biased Schottky contact.

tion 2.13), and the resulting condition is explicitly given in Ref. 64 as

$$\underbrace{\frac{d}{\lambda_S}}_{1.2} \ll \underbrace{\frac{w}{W} \frac{\rho_c}{\rho_N \lambda_S}}_{150} \ll 1, \quad (4.15)$$

with W denoting the average contact width, w the channel thickness, and inserting the parameters of sample A2. Clearly, the maximal value of MR is not reached if the transport length exceeds the spin relaxation length ($d/\lambda_S > 1$). However, in a biased device, the spin relaxation length typically exceeds the spin diffusion length due to the drift induced by the electric field,^{64,129,130} which could potentially lead to increased signals. More importantly, as it was the case without the geometric correction, the investigated samples are not expected to fall into the window of a substantial magnetoresistance. Specifically, the interface resistance is too large by more than two orders of magnitude for the condition to hold.

Nonetheless, MR signals, albeit small, can be observed as shown in Fig. 4.21(b) for a field sweep along the easy axis of magnetization. The resistance of the device is increased for an antiparallel magnetization configuration, and the MR ratio is found to be 0.016% for an applied current of 4 μA . The analysis above (Fig. 4.22)

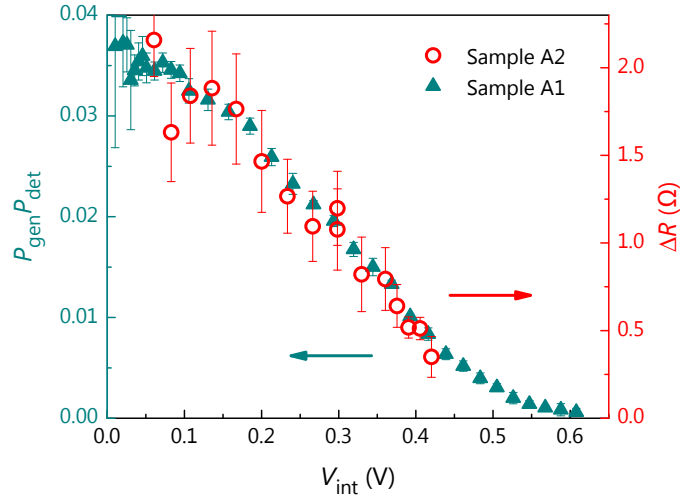


Figure 4.24: Comparison of the local spin valve resistance changes $\Delta R = R_{\text{ap}} - R_{\text{p}}$ for sample A2 with $P_{\text{gen}}P_{\text{det}}$ as deduced from the non-local spin valve signals for sample A1 under spin injection conditions as a function of interface voltage.

predicted a magnetoresistance ratio of 0.015% for sample A2, which is in surprisingly good agreement with the measured value considering the different geometry as well as the uncertainty of all parameters.

Since the local spin valve is a device which relies on the efficient injection of a spin-polarized current, the magnetoresistance signal is expected to decay with an increasing interface potential across the reverse-biased Schottky contact. Figure 4.23(a) shows ΔR as a function of the applied current. As expected, the magnetoresistance signal is maximal for small currents and decays rapidly, and no difference in resistance between the parallel and antiparallel configurations is observed beyond about 30 μA .

For further comparison the interface bias dependence of the magnetoresistance signal is addressed in Fig. 4.23(b). The figure depicts the voltage difference $\Delta V = V_{\text{ap}} - V_{\text{p}}$ as a function of the interface potential measured across the spin injecting contact while a local spin valve current I is applied as shown in the inset. ΔV is seen to increase with V_{int} and forms a peak between 200 and 300 meV, which agrees very well with the interface-bias dependence of the non-local spin valve signal of Fig. 4.15(b).

To further strengthen the hypothesis that the operation of the local spin valve is limited by the bias dependence of the spin injection efficiency, Fig. 4.24 combines the local magnetoresistance for sample A2 and the decay of the non-local spin valve signal for sample A1 (same data as in Fig. 4.13) in one plot. The data points of ΔR are seen to track the decay of the non-local spin valve signal, which indicates that both local and non-local spin valves are limited by the same mechanism, which is the decay of the spin injection efficiency with increasing interface bias.

4.7 Discussion

In this section, a few aspects and consequences of the above-mentioned results are discussed. Generally speaking, the findings emphasize that in addition to the magnetic properties of the contacts, such as the Curie temperature or the energy-dependent spin polarization of the conduction electrons around the Fermi energy of the ferromagnetic metal, also the current-voltage characteristics have to be considered when engineering contacts for the efficient electrical spin injection. The importance of the contact resistivity has been pointed out in the literature in terms of the conductivity mismatch problem and the feedback problem for small contact resistivities (cf. chapter 2). In addition, for contact resistivities which are too large, the dwell time problem limits the magnetoresistance in local spin valve structures. These considerations are manifested in equation 4.15. In this respect, the reported results of this chapter can be regarded as an investigation of an additional constraint that limits the electrically generated spin accumulation in the semiconductor. That is, if the spin generation efficiency decays with bias for a given contact, the contact resistance must be sufficiently small to allow for an appreciable current at a small interface bias. This aspect has to be kept in mind when designing spin injection experiments.

For rectifying Schottky contacts that are biased in the reverse direction, the consequences are particularly drastic as can be seen from the presented comparison of the samples A, B, and C. Consider the forward direction in Fig. 4.13, which is the relevant condition for spin extraction. Importantly, the efficiency of spin generation is found to be comparable for all three samples, at least judging from the

available bias range. Nonetheless, the performance of the samples is fundamentally different in that samples B and C neither allow for the detection of non-local voltages for spin injection conditions nor do they show a measurable magnetoresistance in the local spin valve configuration. This behavior of samples B and C is explained by a high contact resistivity in the reverse direction in combination with an assumed decay of the injection efficiency with increasing reverse bias.

These conclusions are actually found to be of a more universal relevance, when one considers that a decay of the spin generation efficiency or a sublinear increase of the spin signal with applied current has been reported for various spin injector systems other than the Fe₃Si/*n*-GaAs contacts investigated in this study, including contacts of ferromagnetic metals with *n*-type GaAs,^{28,63,103,111–114,131,132} *n*-type and *p*-type Si,^{19,50,54,84,133} and *n*-type Ge.¹¹⁹ Such a behavior probably originates from a combination of the above-mentioned mechanisms (cf. section 4.4.3). Even if the detailed origins are not fully understood, a decay of the bias dependence of the injection efficiency is a regularly observed behavior.

In particular, the described behavior demands close attention to be paid to the bias conditions when the performance of different injector materials in spin light-emitting diodes is evaluated. As briefly described in section 4.1, the spin injection efficiency in GaAs-based spin LEDs has been found to depend sensitively on the choice of the injector metal. While for Fe, MnAs, and Fe₃Si ($T_S = 200$ °C) spin injection efficiencies of 5%,^{17,134} 6%,⁸⁶ and 10%⁸⁷ have been observed, respectively, the spin injection efficiency was found to be 50% for a Co₂FeSi injector.⁸⁵ This leap in efficiency has been attributed to the spin-dependent band structure of Co₂FeSi, which is predicted to be a ferromagnetic half metal.¹³⁵ However, a more than five-fold increase cannot be solely explained by the assumed high spin polarization of the conduction electrons in the ferromagnet, considering that the spin polarization of Fe, MnAs, and Fe₃Si is about 45%.^{136–138} Rather, the voltage drop across the Schottky contact has to be taken into account.

The optical detection of the injected spin accumulation demands light emission and thus a forward bias across the *p-n* junction on the order of the built-in potential. In that situation, the ferromagnet/*n*-type GaAs contact is reverse biased, which can result in substantial interface voltages across the Schottky barrier. In fact, with respect to Fe₃Si, Co₂FeSi forms a contact with *n*-GaAs that yields rela-

tively high leakage currents in the reverse direction.¹³⁹ Although the mechanism of this leakage is not known at present, it allows for the operation of Co₂FeSi-based spin LEDs at a smaller interface potential across the Schottky barrier. This circumstance is likely to enable operating conditions with a larger injection efficiency. In other words, it is probable that the more resistive contacts of spin LEDs using Fe₃Si lead to the determination of the injection efficiency at a substantial interface voltage, which is expected to be lower than its zero-bias value.

As pointed out in section 4.4.4, the size of the contact can be increased to achieve the operation of spin injection devices at small interface biases leading to an improvement of the spin signal. While an increase of the contact length W_y may be practical, an increase of the contact width W is not suitable for most applications. Consider for example a local spin valve in the lateral geometry, where an increase in size of the injector contact would inevitably lead to an increase in the average (center-to-center) spin transport length. This example shows that there is a need for more sophisticated techniques of contact engineering. Some of which will be discussed in the last section of this chapter.

4.8 Outlook

Finally, some strategies for the improvement of the performance of all-electrical spin injection and detection devices are discussed for a given semiconductor material (unaltered λ_S and ρ_N) and aside from a geometrical optimization of the device structure. Clearly, it is of great importance that a reduction of the specific contact resistivity is achieved. The reasons are twofold: First, considering the criterion of equation 4.15, it is clear that a reduction of ρ_c by two orders of magnitude is desirable to overcome the dwell time problem in local spin valves. Second, because the spin injection efficiency is found to decay with increasing reverse bias, a large contact resistance drastically reduces the magnitude of voltages induced by spin injection in all geometries.

A high level of doping in the semiconductor near the interface with the metallic contact leads to a reduction of the Schottky barrier width. Therefore, a larger tunneling probability can in principle be achieved by increasing the donor concentration in that region. However, an increase well beyond the nominal dop-

ing concentration of $5 \times 10^{18} \text{ cm}^{-3}$ is difficult to achieve due to the electrical self-compensation of Si impurities.^{140,141} Another way to reduce the depletion layer width is the use of a thin, delta-doped layer in the semiconductor region close to the contact with the ferromagnet as shown for contacts to silicon.^{84,133} An alternative strategy consists of using a ferromagnetic metal or an additional interfacial layer of a non-magnetic metal with a low work function. It has been shown that a sub-nanometer thin layer of Gd between a ferromagnetic metal and an oxide tunneling barrier leads to a reduction of the height of the Schottky barrier in the semiconductor.¹⁴² This approach is not suitable for direct contacts to GaAs without oxide barriers, however, because metal contacts are known to pin the Fermi level close to mid-gap irrespective of their work function.⁹² Lastly, significantly lower contact resistivities have been reported for devices using oxide or graphene⁵¹ layers as tunneling barriers between the ferromagnetic metal and the semiconductor.

CHAPTER 5

Extraction spin valves

In this chapter, results drawn from the investigation of lateral $\text{Co}_2\text{FeSi}/n\text{-GaAs}$ spin transport structures are presented. The most important aspects are:

- A novel device concept is presented. It consists of a local spin valve, which utilizes spin generation by extraction instead of injection. This device is referred to as an extraction spin valve.
- It is shown experimentally that the extraction spin valve concept can be extended to a device comprising two extraction events.
- The measurements can be understood quantitatively in the framework of a simple spin transport model.
- Extraction spin valves relying on multiple spin extraction events can potentially find application as spin polarizers, magneto-logic gates, or for the read-out of magnetic data.

Most of the results of this chapter have been previously described in Refs. [143–145](#) as well as the publication text of the European patent EP 2 688 072 B1.

5.1 Introduction

As it was the case for the previous chapter, this chapter deals with the generation and detection of a non-equilibrium spin polarization in the n -type GaAs channel of lateral ferromagnet/semiconductor hybrid spin transport structures. As explained earlier, local spin valves constitute an important building block for spintronic device concepts. These devices rely on electrical spin injection and the subsequent local detection of the spin-polarized drift current. However, here the focus will lie on the generation by electrical spin extraction, i.e., upon electron flow from the semiconductor into the ferromagnetic metal.

Applications which utilize spin extraction have so far been considered in theoretical device proposals only.^{146–148} This kind of device benefits from the fact that the Schottky barrier is forward biased, which yields higher currents than in reverse bias. Consequently, for a device relying on spin extraction, a decrease in the efficiency of spin generation with increasing interface bias does not constitute as much of an impediment as it was outlined for the conventional local spin valve in section 4.6.

The Heusler alloy Co_2FeSi is used as the spin generator in this chapter. Compared to the other ferromagnetic metals used in the previous chapter, the current voltage characteristics of the $\text{Co}_2\text{FeSi}/n\text{-GaAs}$ contacts are more symmetric with respect to forward and reverse directions and have the advantage of allowing for a higher current at a given interface bias.^{64,139}

Furthermore, Co_2FeSi is a particularly promising material for spintronic applications due to its high Curie temperature of more than 1000 K¹³⁵ and especially due to its predicted half-metallic character. Calculations using density functional theory have been performed,^{56,135} which show a gap of the minority spin density of states in a region around the Fermi energy for Co_2FeSi in its fully ordered $L2_1$ phase. The close lattice matching with GaAs enables the epitaxial growth of hybrid interfaces with a high degree of perfection, as demonstrated in a series of publications.^{78,79,149} In particular, it was found that the material crystallizes predominantly in the $L2_1$ phase for the growth at substrate temperatures exceeding 200 °C, while it exhibits a partly-disordered $B2$ phase for lower substrate temperatures accompanied by a coexistence of both phases with a vertical¹⁵⁰ and lateral^{151–154} spatial distribution.

The crystallographic ordering of the ferromagnetic layer strongly influences the spin injection properties of $\text{Co}_2\text{FeSi}/n\text{-GaAs}$ contacts in spin light-emitting diodes. Specifically, the sign of the injected spin polarization depends on the dominating phase.⁵⁶ However, while for a high degree of order in the ferromagnetic film a high growth temperature is desirable, it has to be considered that other thermally activated processes such as the diffusion of Co and Fe atoms into the semiconducting part^{85,109,155,156} and the interfacial degradation⁷⁹ adversely affect the spin injection efficiency. An optimal substrate temperature of 280–300 °C has been identified to constitute a compromise between these detrimental effects and the crystallographic disorder and it yielded a spin injection efficiency of about 50% in spin light-emitting diodes.^{56,85}

In addition, the all-electrical spin injection, transport, and detection in lateral transport structures based on the $\text{Co}_2\text{FeSi}/n\text{-GaAs}$ hybrid system has been investigated.⁶⁴ Here, spin valve as well as Hanle signals have been reported in both the non-local and the local configuration. From these measurements, a spin injection efficiency of 16% and a spin drift length of 11 μm were inferred at 40 K.

In this chapter, the extraction spin valve (ESV) is introduced as a new member to the family of spin valve devices in lateral ferromagnet/semiconductor spin transport structures, which includes the well-studied non-local spin valve (NLSV, section 4.4.1) and the less frequently reported local spin valve (LSV, section 4.6). This novel magnetoresistance device is essentially a local spin valve based on spin extraction. It is shown that the extraction spin valve offers intriguing characteristics including the scalability to lateral multiple extraction devices.

5.2 Experimental

The structures investigated in this chapter were grown by MBE and processed using optical lithography according to the description in chapter 3. Two samples are studied, namely sample 1 and sample 2. Both make use of the ferromagnetic Heusler alloy Co_2FeSi grown epitaxially on the n -type GaAs channel at a substrate temperature of 280 °C as the spin generating layer. The thickness of this layer is 16 nm for both samples. Figure 5.1 shows the processed sample 1 with the conductive GaAs mesa region and evaporated Au/Ti contacts. The ferromagnetic

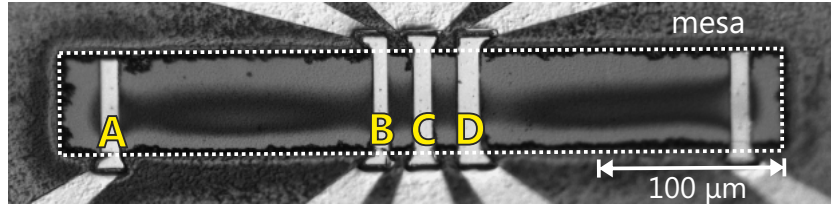


Figure 5.1: Optical micrograph of sample 1 with ferromagnetic contact stripes labeled A, B, C, and D.

contacts are labeled A, B, C, and D with widths 10, 8, 10, and 12 μm , respectively. The edge-to-edge spacing between B and C as well as between C and D is 14 μm (3 μm) for sample 1 (sample 2), while the spatial separation between A and B (about 145 μm) exceeds the spin relaxation length by more than one order of magnitude. Therefore, contact A serves as a source of unpolarized electrons, while contacts B, C, and D are used for extraction and/or detection of electron spins.

The electrical measurements rely on a steady-state method, wherein currents are determined from nanovoltmeter readings of voltage drops across an ohmic resistor with a resistance of 82.4 Ω . All measurements presented in this chapter are performed at a temperature of 40 K.

5.3 Extraction spin valve

In this section, the extraction spin valve is introduced as a novel type of spin transport device. The measurement geometry and principle of operation is explained in detail. Also, it is shown that the underlying mechanism – the generation of a spin-polarized drift current by spin extraction at one ferromagnetic contact and its subsequent detection at another ferromagnetic contact – can be suppressed by an out-of-plane magnetic field via Hanle spin precession and dephasing. Next, the current dependence of the extraction spin valve effect is presented, followed by an estimation of the efficiency of spin extraction by comparison with a local spin valve arrangement.

Spin extraction is the essential physical process necessary for the operation of ESV devices. To demonstrate that spin extraction at a ferromagnetic contact leads to an exploitable polarization for spin valves, the configuration depicted schemat-

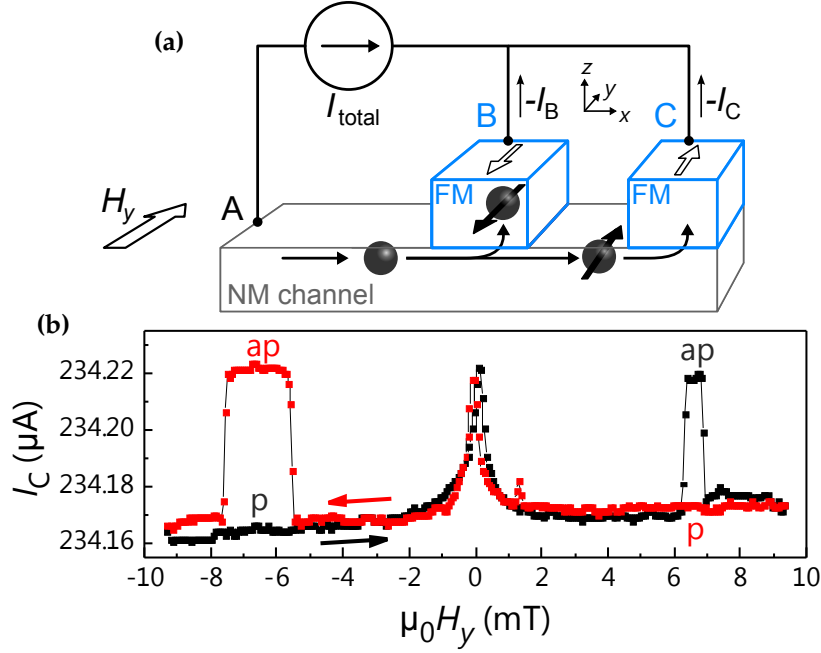


Figure 5.2: (a) Schematic representation of a spin extraction experiment, with ferromagnetic electrodes B and C. Black arrows indicate the direction of net electron flow. (b) Output current I_C as a function of the in-plane magnetic field (applied along the ferromagnetic easy axis) for $I_{\text{total}} = 500 \mu\text{A}$ at 40 K. A higher current level is observed for an antiparallel (ap) as compared to a parallel (p) orientation of the magnetizations of B and C.

ically in Fig. 5.2(a) is utilized. An unpolarized electron current is injected into an *n*-type GaAs channel at stripe A, whereas stripes B and C serve as a pump-and-probe arrangement, i.e., the degree of spin extraction at contact B is detected at stripe C via a spin-dependent contact resistance. In this current divider, a current source supplies a constant I_{total} so that electrons flow into both B and C stripes in a parallel manner. Since the spatial separation between stripes A and B exceeds the spin drift length in GaAs, the electron current is unpolarized when reaching contact B.

The partial current I_C measured in sample 1 is shown in Fig. 5.2(b) as a function of the external magnetic field $\mu_0 H_y$ applied along the easy axis of magnetization of the ferromagnetic stripes. Due to the different coercivities of the FM electrodes, the

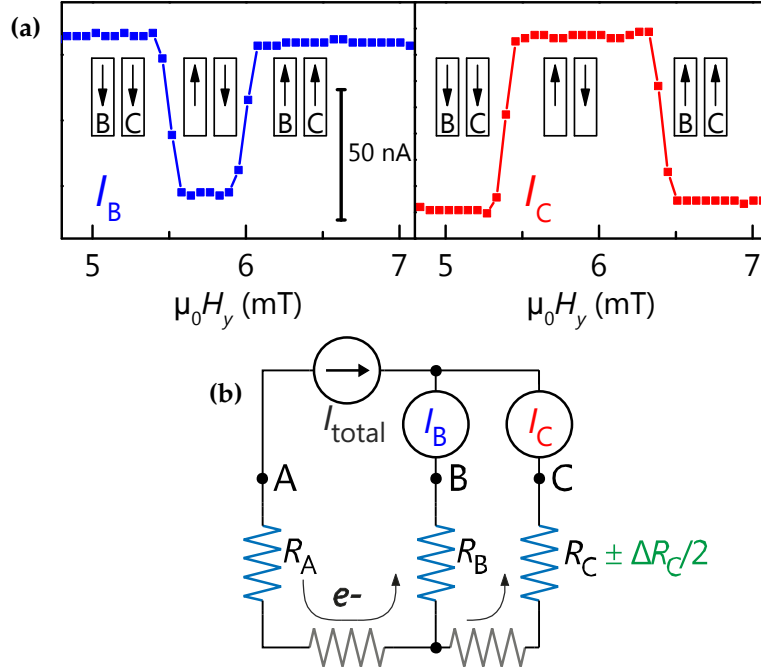


Figure 5.3: (a) Current versus applied field for output leads B (left) and C (right) with $I_{total} = 600 \mu\text{A}$ (sample 1) measured in separate runs. The arrows indicate the parallel and antiparallel magnetization configurations of B and C. (b) Simplified circuit diagram for the measurement of I_C and I_B . The contact resistances are represented by ohmic resistors (blue), and the horizontal resistors (gray) represent the resistance of the semiconductor channel. ΔR_C denotes the spin dependence of the contact resistance, and the black arrows indicate the direction of the net electron flow.

system undergoes a switching sequence from a parallel (p) to an antiparallel (ap) configuration and back to a parallel configuration upon sweeping the field. Correspondingly, the switching of I_C upon magnetization reversal of the FM stripes is observed. Note that the switching field is of a stochastic nature, as seen from the different peak widths for positive and negative fields. Such stochastic behavior has been reported before in non-local spin valve structures.¹⁰² Furthermore, as it was the case for the non-local spin valve in section 4.4.1, the feature at $H_y = 0$ can be attributed to dynamic nuclear polarization¹⁰⁰ or stray fields resulting from a roughness of the ferromagnet/semiconductor interface.¹⁹

The dependence of I_C on the magnetization configuration is an indication of

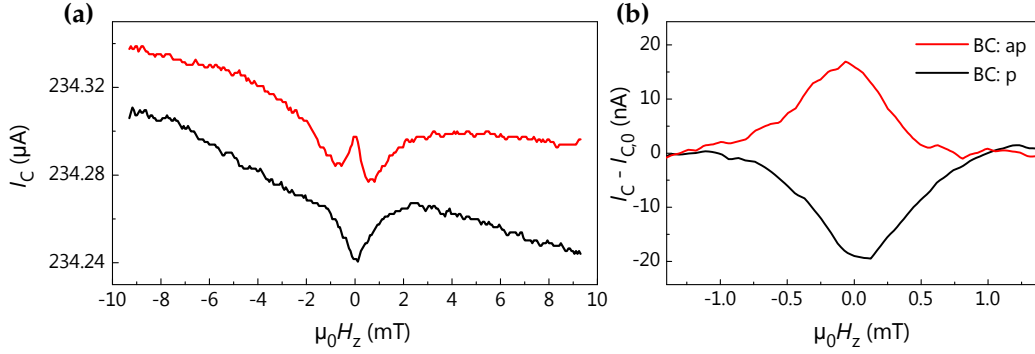


Figure 5.4: Output current I_C of the extraction spin valve as a function of the out-of-plane magnetic field H_z for sample 1 and $I_{\text{total}} = 500 \mu\text{A}$. The red (black) line represents the measurement for an antiparallel (parallel) magnetization configuration of contacts B and C. **(a)** Raw data, **(b)** modified data obtained by subtracting a magnetic field-dependent background $I_{C,0}$.

magnetoresistance mediated by a spin polarization of the conduction electrons inside the semiconductor. The observed behavior is explained by a contact resistance of the probe stripe C which depends on the orientation of this spin polarization relative to the magnetization of stripe C. Obviously, the origin of the electron polarization is a spin generation process at the pump stripe B. In contrast to the case of spin injection at contact B (see comparison with local spin valve experiment below), the resistance at stripe C decreases in the ap configuration, i.e., the spin polarization generated at the forward-biased FM/SC contact of stripe B is antiparallel to that generated by spin injection. This observation identifies spin extraction as the generation process at stripe B.⁸⁰ Altogether, the measurement demonstrates that the electron polarization induced by spin extraction is sufficient to observe a clear local spin valve effect between the ferromagnetic stripes B and C.

A comparison of the field dependence of the output currents through contacts B and C is shown in Fig. 5.3(a) for two separate measurements. While I_C switches to a higher current state for an antiparallel magnetization configuration, I_B is found to be reduced for this configuration. This observation confirms a magnetization-dependent change in contact resistance at C and can be explained by the circuit schematic depicted in Fig. 5.3(b). This model circuit uses an ohmic approxima-

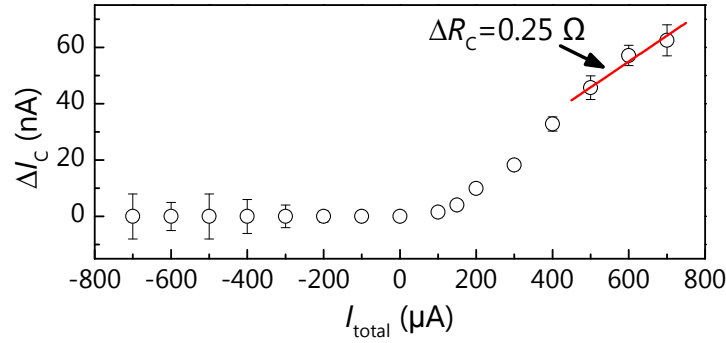


Figure 5.5: Output current changes ΔI_C as a function of the applied current I_{total} (sample 1). The red solid line is the calculated current change resulting from a contact resistance change of $\Delta R_C = 0.25 \Omega$.

tion of all contact resistances. The current is unpolarized prior to the extraction event at contact B and thus experiences no magnetization-dependent resistance at that contact, whereas the polarized current into C leads to a spin-dependent resistance $R_C \pm \Delta R_C/2$. A higher (lower) contact resistance corresponds to the parallel (antiparallel) magnetization configuration of B and C.

To further corroborate that spin transport between the contact stripes is responsible for the magnetization-dependent output signals of the extraction spin valve, spin precession and dephasing in an out-of-plane magnetic field is studied. Figure 5.4(a) shows the measured output current I_C as a function of $\mu_0 H_z$. Different background levels for the two curves arise due to thermal drift.

To illustrate the difference between the curves for the parallel and antiparallel case, the same measurement is shown in Fig. 5.4(b) with a subtracted field-dependent background current $I_{C,0}$, which is approximated by a quadratic polynomial in H_z . The non-linearity of the background signal possibly arises from three-terminal Hanle spin precession, where the spin polarization is generated and detected by the same ferromagnetic contact, similar to the situation described in section 4.5.

The output current shows a peak at zero magnetic field for the antiparallel and a dip for the parallel magnetization configuration. For an increased field strength, the spin polarization is dephased, and both configurations yield the same output current. The difference of the signals at zero field corresponds to the height of the

peaks for the in-plane field sweeps of Fig. 5.2. In addition, the curves in Fig. 5.4(b) can be fitted with reasonable parameters according to the model described in section 4.4.2. All in all, one can be confident that the described observation corresponds to the Hanle effect, and its observation can be regarded as evidence for spin transport in the extraction spin valve.

The dependence of the spin extraction signal on the applied current is depicted in Fig. 5.5. The jumps in current upon magnetization reversal, $\Delta I_C = I_{C,ap} - I_{C,p}$, increase monotonically with I_{total} . When the direction of electron flow is reversed, i.e., for a net electron flow from B and C into the faraway contact A, no spin-dependent signals are observed, which indicates that spin injection at B is not appreciably affected by a spin imbalance in the semiconductor channel. Kirchhoff's rules are analyzed for the simple model circuit of Fig. 5.3(b) to extract the spin-dependent part of the contact resistances ΔR_C from the measured current changes. All resistances in the model circuit are approximated to be ohmic and are estimated from pairwise measurements of current-voltage curves between all contacts of sample 1[‡]. ΔR_C is found to be about 0.25Ω for $500 \mu A \leq I_{total} \leq 700 \mu A$.

To quantify the efficiency of spin generation by extraction, one can compare the spin-dependent contact resistances (ΔR_C) for two cases: spin extraction (ΔR_C^{extr}) and spin injection (ΔR_C^{inj}) at contact B. For the injection, the local magnetoresistance is measured between B and C with all other leads disconnected as shown in Fig. 5.6. Such a local spin valve (LSV) experiences a voltage change for a constant applied current when the magnetization directions of the electrodes undergo a transition between the parallel and antiparallel configurations, analogous to the description in section 4.6. This behavior can be described by a change in contact resistance at contact C due to spin injection at contact B. The magnetoresistance $\Delta R = R_p - R_{ap}$ is then estimated as $\Delta R_C^{inj} = -0.37 \Omega$ for an applied current of $266 \mu A$.

For both the LSV and the ESV (see Figs. 5.2 and 5.6), the spin-dependent resistances can be approximated by

$$\Delta R_C^{extr/inj} = S_C^{extr/inj} \delta = S_B^{extr/inj} e^{-d/\lambda_S} \delta, \quad (5.1)$$

where $S_B^{extr/inj}$ ($S_C^{extr/inj}$) denotes the electron spin polarization arriving at contact B

[‡] $R_B = R_C = 513 \Omega$, GaAs channel resistance between contacts B and C: $R_{Ch} = 75 \Omega$

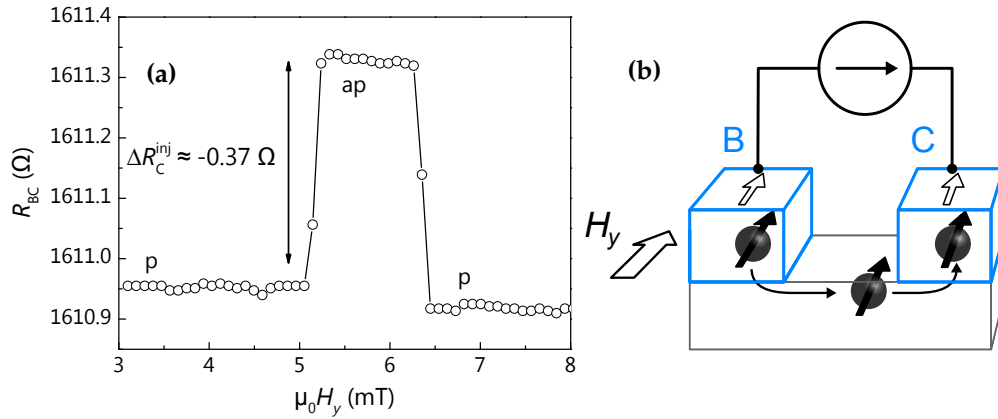


Figure 5.6: (a) Local spin valve resistance R_{BC} as a function of $\mu_0 H_y$ for contacts B and C on sample 1 and an applied current of 266 μA . (b) Corresponding schematic diagram.

(C) generated by extraction or injection, λ_S the spin drift length in the SC, and d the separation between contacts B and C. δ is a quantity proportional to the detection efficiency. Since the detection mechanism is the same for the LSV and the ESV, the spin generation efficiencies $\eta^{\text{extr/inj}} \propto S_B^{\text{extr/inj}}$ can be compared:

$$\eta^{\text{extr}} / \eta^{\text{inj}} = \Delta R_C^{\text{extr}} / \Delta R_C^{\text{inj}} \cong -0.7.$$

From this estimate, two important results can be deduced: First, the non-equilibrium resulting from a forward bias across the Schottky contact exhibits an opposite sign compared to a reverse bias, which confirms the expectation.⁸⁰ Second, the spin generation by extraction is of a comparable efficiency as the spin generation by spin injection. However, both spin injection and extraction are expected to exhibit a strong bias dependence (cf. section 4.4.3), which should be taken into account for a more rigorous comparison.

5.4 Double extraction spin valve

The spin extraction experiment depicted above can be regarded as a building block of an extended device with a more complex functionality, which will be referred to as a double extraction spin valve (DESV). The corresponding current divider

5.4 Double extraction spin valve

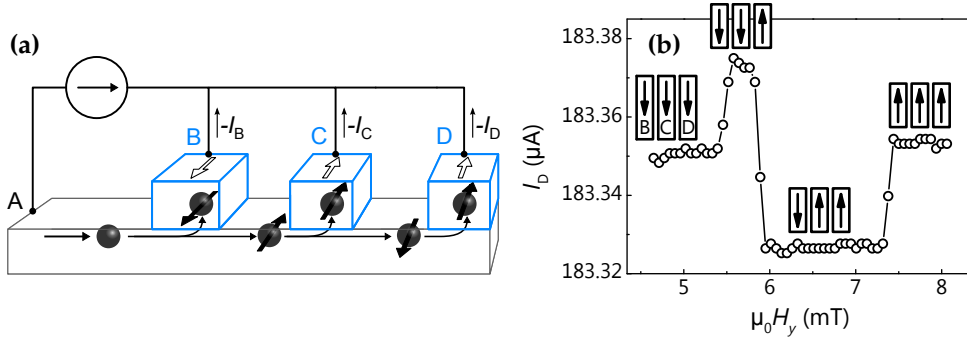


Figure 5.7: Double extraction spin valve. A circuit schematic is shown in (a). The output current I_D as a function of the in-plane field H_y is displayed in (b) for sample 1.

circuit comprising three output leads is shown in Fig. 5.7(a). Here, the electrical current flows from the remote contact A into the contacts B, C, and D in a parallel manner. As for the ESV, the extracted spin information from contact B is sensed by contact C. Furthermore, an additional contact D detects the extracted spins from both B and C.

The measured output current I_D exhibits three different levels upon sweeping the in-plane magnetic field as shown in Fig. 5.7(b). These levels correspond to particular magnetization configurations of the ferromagnetic electrodes B, C, and D, as indicated by the arrows. Note that the labeling of the intermediate configurations $\downarrow\downarrow\uparrow$ (BCD) and $\downarrow\uparrow\uparrow$ is not obvious at this point. However, the magnetization configurations can be determined experimentally using Hanle measurements in the local geometry or, alternatively, theoretically deduced after consideration of a model for spin transport (both explained below in this and the following sections).

For further investigations, a slightly more sophisticated circuit is employed, which includes a second current source as illustrated in Fig. 5.8(a). Note that this modification with respect to the circuit in Fig. 5.7(a) leaves the direction of net electron flow in the device unchanged. However, the measurement of V_{CD} across the additional current source I_2 has the advantage of a higher sensitivity to spin-dependent changes in resistance at contacts C and D and yields a lower noise level in the experiments. For further analysis sample 2 is used, which has the benefit of a smaller contact spacing so that larger spin-induced signals are obtained.

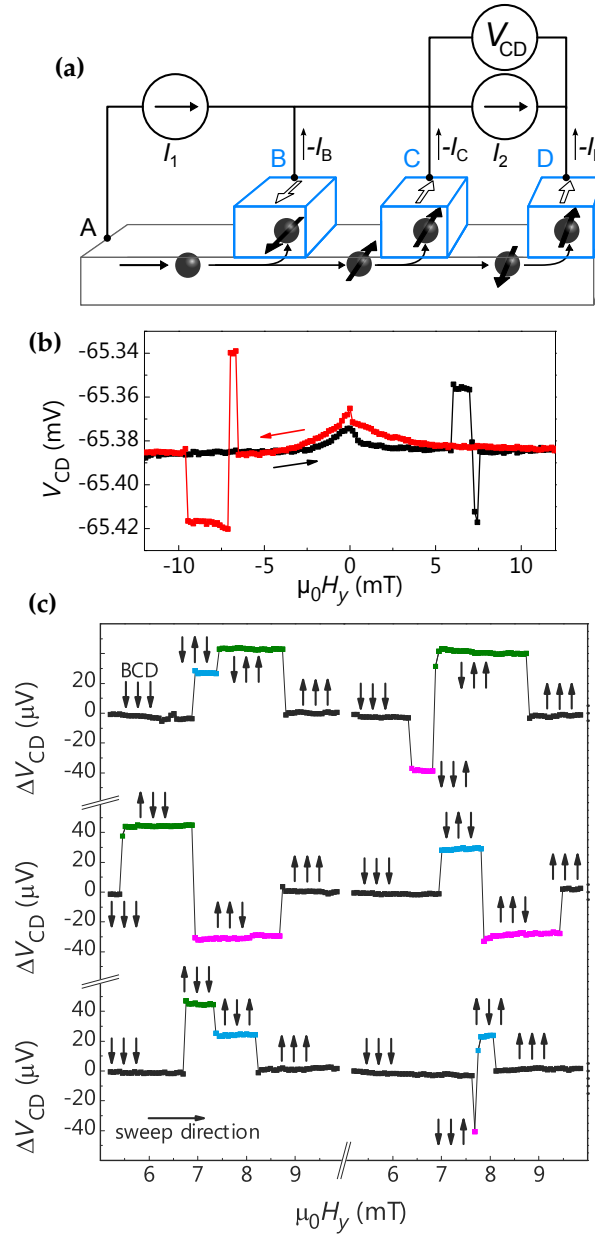


Figure 5.8: (a) Circuit schematic of a double extraction spin valve comprising two current sources. The output voltage V_{CD} upon sweeping H_y for sample 2 with $I_1 = 400 \mu\text{A}$ and $I_2 = 50 \mu\text{A}$ is depicted in (b). All six sequences of output voltage changes ΔV_{CD} measured in successive field sweeps are shown in (c). The corresponding magnetization configurations have been experimentally determined and are indicated by black arrows.

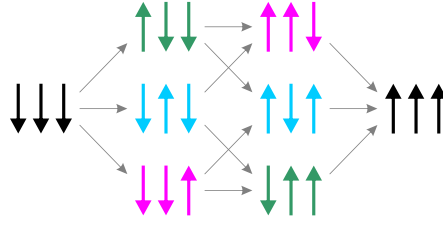


Figure 5.9: Illustration of the DESV switching sequences. The colored vertical arrows represent the magnetization orientations of the three ferromagnetic contacts B, C, and D in that order. The colors indicate the four different electrical output levels. Gray arrows represent the six possible sequences of single switching events, which lead to a complete reversal of the magnetization configuration.

As seen from Fig. 5.8(b), one can again access three output voltage levels by sweeping the field from negative to positive ferromagnetic saturation and vice versa with each voltage level corresponding to a particular magnetization configuration of contacts B, C, and D. From a series of successive measurements shown in Fig. 5.8(c) it becomes clear that not only the exact switching fields exhibit a randomness, as it was inferred from the different peak widths in the case of the ESV in Fig. 5.2(b), but the order of magnetization reversals also occurs in a stochastic manner. As a consequence, a variety of possible sequences of single switching events is observed that lead to a complete reversal of the magnetization configuration from $\downarrow\downarrow\downarrow$ to $\uparrow\uparrow\uparrow$. In total, six sequences and four unique output levels are observed, as indicated by the different colors.

Table 5.1: Numbers of ferromagnetic contacts, magnetization configurations, electrical output levels, and switching sequences in extraction spin valve devices. The ESV and the DESV correspond to the cases $m = 2$ and $m = 3$, respectively.

FM contacts	Magnetization configurations	Output levels	Sequences
2	4	2	2
3	8	4	6
m	2^m	2^{m-1}	$m!$

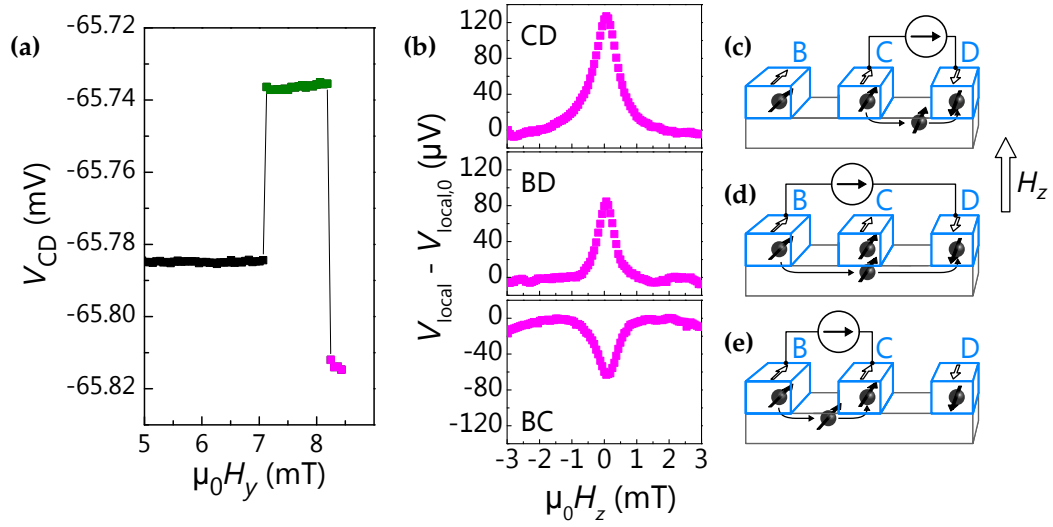


Figure 5.10: Exemplary local Hanle-effect measurements for the assignment of the magnetization configuration $\uparrow\uparrow\downarrow$ to the magenta output voltage level of the DESV (sample 2). An aborted measurement of V_{CD} upon sweeping $\mu_0 H_y$ in the DESV arrangement of Fig. 5.8 is shown in (a). Hanle voltages V_{local} as a function of the out-of-plane field $\mu_0 H_z$ in the local geometry for the indicated electrode pairs with a subtracted background voltage $V_{local,0}$ are depicted in (b). The corresponding measurement configurations are displayed in (c) – (e).

To illustrate the increase in device functionality which accompanies the addition of one more ferromagnetic output lead to the ESV, some observed features of the DESV are emphasized. The device comprises 3 ferromagnetic contacts, which lead to 8 different magnetization configurations. These configurations can be grouped into 4 pairs of 2 which are symmetrically equivalent (such as $\downarrow\downarrow\downarrow$ and $\uparrow\downarrow\uparrow$) and thus share a common output level. As a result, 4 unique output voltage levels are observed. In the experimental situation, where the magnetization reversal of the contacts occurs at a stochastic switching field, the sweeping of the external field allows for the observation of 6 different switching sequences. These correspond to all possible ways to get from $\downarrow\downarrow\downarrow$ to $\uparrow\uparrow\uparrow$ with single switching events, as illustrated in Fig. 5.9. In addition, an overview including a generalized approach for an extraction spin valve with multiple ferromagnetic contacts is given in Table 5.1. The richness of possible output levels stems from the fact that all but the first and

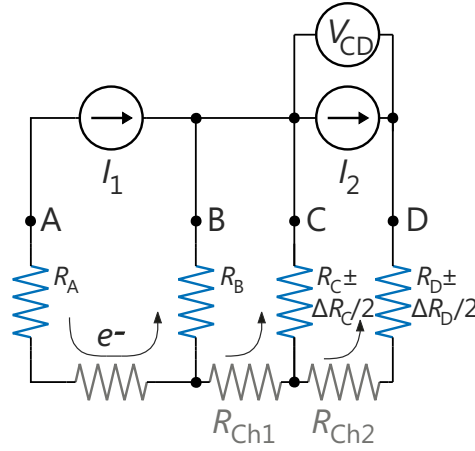


Figure 5.11: Model circuit for the double extraction spin valve of Fig. 5.8. All resistances in the circuit are approximated to be ohmic.

last of the ferromagnetic contacts act in a dual role as a spin generator and a spin detector so that m ferromagnetic contacts lead to 2^m magnetization configurations, $m!$ switching sequences, and 2^{m-1} unique output levels.

To assign the magnetization configurations of the DESV [denoted by the black arrows in Fig. 5.8(c)] to their corresponding output levels, spin precession and dephasing in the Hanle geometry is investigated for the local geometry and with a magnetic field applied out of the sample plane. This direction corresponds to the magnetic hard axis of the FM contacts, and thus the in-plane magnetization is maintained for the applied magnetic fields, as explained previously in section 4.4.2 for the non-local geometry and in section 5.3 for the ESV geometry. Examples of local Hanle measurements are shown in Fig. 5.10(b). To find the magnetization configurations, the procedure is as follows. First, the output level of interest is prepared by aborting a sweep of the in-plane magnetic field $\mu_0 H_y$ in the MESV configuration as shown in Fig. 5.10(a). Then, the local voltages for a constant applied current of 400 μA are measured in the LSV arrangement as a function of the out-of-plane field H_z for the denoted electrode pairs, see Fig. 5.10(b). Finally, the observed shapes of the Hanle curves allow for a mutual determination of the relative magnetizations of B, C, and D. More specifically, spin dephasing with increasing field leads to a peak (dip) at $H_z = 0$ for an antiparallel (a parallel) magnetization orientation of each pair of contacts. Consequently, the magnetization

Table 5.2: Experimental double extraction spin valve output levels ΔV_{CD} [compare Fig. 5.8(c)], spin-dependent contact resistances, and spin polarization values deduced from the model. The upper (lower) sign of S_C^{in} and S_D^{in} corresponds to the magnetization state \uparrow (\downarrow) of contact B.

Conf. (BCD)	$\uparrow\uparrow\uparrow, \downarrow\downarrow\downarrow$	$\uparrow\uparrow\downarrow, \downarrow\downarrow\uparrow$	$\uparrow\downarrow\uparrow, \downarrow\uparrow\downarrow$	$\uparrow\downarrow\downarrow, \downarrow\uparrow\uparrow$
ΔV_{CD} (exp.)	0 by def.	$(-34 \pm 4) \mu\text{V}$	$(27 \pm 3) \mu\text{V}$	$(43 \pm 2) \mu\text{V}$
ΔR_C	0.62Ω	0.62Ω	-0.62Ω	-0.62Ω
ΔR_D	0.68Ω	-0.68Ω	-0.32Ω	0.32Ω
S_C^{in}	$\pm 5.4\%$	$\pm 5.4\%$	$\pm 5.4\%$	$\pm 5.4\%$
S_D^{in}	$\pm 5.9\%$	$\pm 5.9\%$	$\mp 3.0\%$	$\mp 3.0\%$

configuration $\uparrow\uparrow\downarrow$ (BCD) is deduced for the aborted output level. All other magnetization configurations can be assigned to their corresponding voltage levels in the same way.

The output levels ΔV_{CD} in Fig. 5.8(c) can be explained quantitatively by regarding a spin transport model (explained in the next section) in conjunction with the simple model circuit shown in Fig. 5.11. In the first step, the spin-induced changes in the contact resistances are related to the measured output voltages for all configurations using Kirchhoff's laws,

$$V_{CD} = \frac{(R_C + \Delta R_C/2)((I_2 - I_1)R_B + I_2 R_{\text{Ch1}})}{R_B + R_C + \Delta R_C/2 + R_{\text{Ch1}}} + I_2(R_D + \frac{\Delta R_D}{2} + R_{\text{Ch2}}). \quad (5.2)$$

The contact and channel resistances are estimated to be $R_B = R_C = R_D = 825 \Omega$ and $R_{\text{Ch1}} = R_{\text{Ch2}} = 175 \Omega$ from pairwise measurements of current-voltage curves between all contacts of sample 2. The obtained values are presented in Table 5.2. The circuit model is consistent with the experimental data within the sensible restrictions that (a) the contact resistance of C is dependent on the relative orientation of the magnetizations of B and C (high for parallel, low for antiparallel) and (b) the spin dependence of the contact resistance of D is dominated by the relative magnetization orientation of C and D. In the next step, the changes in contact resistance are explained by the actual extraction-induced spin polarization in the semiconductor using a model for spin transport.

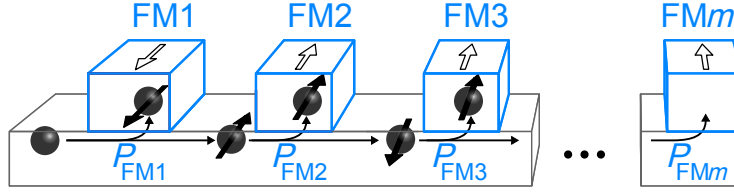


Figure 5.12: Schematic of a generalized multiple spin extraction device comprising m ferromagnetic electrodes. The circuit nodes are labeled P_{FMj} .

5.5 Spin transport model

To describe spin transport in the devices a simple model is developed for an extraction spin valve comprising multiple contacts. The special case of the DESV arises from this consideration, and a comparison of the measured values and the theory is performed.

5.5.1 Generalized form for multiple ferromagnetic contacts

In this section, a general extraction spin valve comprising m ferromagnetic output leads is considered as shown in Fig. 5.12. The illustrated structure is referred to as a multiple extraction spin valve (MESV). Figure 5.13 illustrates two subsequent ferromagnetic stripes j and $j + 1$ in a such a multi-stripe structure. The incoming electron current I_j^{in} at node P_j is characterized by the partial currents $\uparrow I_j^{\text{in}}$ and $\downarrow I_j^{\text{in}}$ of opposite spin polarization and the corresponding polarization S_j^{in} ,

$$I_j^{\text{in}} = \uparrow I_j^{\text{in}} + \downarrow I_j^{\text{in}}, \quad (5.3)$$

$$S_j^{\text{in}} = \frac{\uparrow I_j^{\text{in}} - \downarrow I_j^{\text{in}}}{\uparrow I_j^{\text{in}} + \downarrow I_j^{\text{in}}}. \quad (5.4)$$

The outgoing electron current I_j^{out} at P_j is assumed to be generated by a spin-dependent reflection at the ferromagnetic stripe j . The resulting spin extraction is given by the extraction coefficient η ,

$$\uparrow I_j^{\text{out}} = a(1 \pm \eta) \uparrow I_j^{\text{in}}, \quad (5.5)$$

$$\downarrow I_j^{\text{out}} = a(1 \mp \eta) \downarrow I_j^{\text{in}}, \quad (5.6)$$

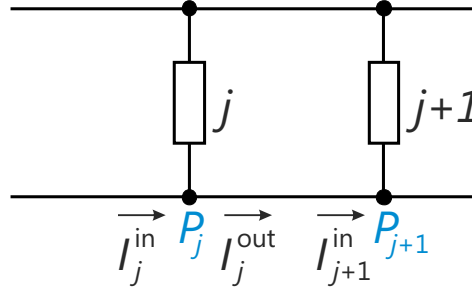


Figure 5.13: Current divider schematic for the spin transport model. See text for an explanation of the labels.

with the sign on the right side of the expression given by the relative orientation of the electron polarization and the magnetization orientation of stripe j . The factor a accounts for a change in the absolute value of the current. The electron polarization S_j^{out} of the outgoing current at P_j ,

$$S_j^{\text{out}} = \frac{\uparrow I_j^{\text{out}} - \downarrow I_j^{\text{out}}}{\uparrow I_j^{\text{out}} + \downarrow I_j^{\text{out}}} , \quad (5.7)$$

is subject to spin relaxation, which leads to a reduced spin polarization of the incoming electron current at P_{j+1} ,

$$S_{j+1}^{\text{in}} = S_j^{\text{out}} e^{-d_j/\lambda_S} , \quad (5.8)$$

where d_j is the distance between stripes j and $j+1$ and λ_S is the spin drift length. Normalizing the incoming electron current at P_{j+1} , the resulting partial currents are given by

$$\uparrow I_{j+1}^{\text{in}} = \frac{1}{2} (S_{j+1}^{\text{in}} + 1) , \quad (5.9)$$

$$\downarrow I_{j+1}^{\text{in}} = 1 - \uparrow I_{j+1}^{\text{in}} . \quad (5.10)$$

Note that dimensionless currents are regarded, because in the end only the spin polarizations are of interest. Finally, the resistance change at stripe $j+1$ is expected

5.6 Application examples

to be proportional to the polarization of the incoming electron current:

$$\Delta R_{j+1} = c S_{j+1}^{\text{in}}. \quad (5.11)$$

5.5.2 Three ferromagnetic contacts (double extraction spin valve)

The DESV constitutes the special case of an MESV with $m = 3$ output leads. Using the described model, one can connect the contact resistances ΔR_C and ΔR_D to the incoming spin polarizations S_C^{in} and S_D^{in} as shown in Table 5.2. Based on the non-local and local spin valve measurements on similar device structures in Ref. 64, $\eta^{\text{extr}} = 16\%$ and $\lambda_S = 11 \mu\text{m}$ are chosen as realistic parameters. Using a proportionality constant c of 11Ω , a very good agreement with the experimental data is achieved, which shows that the simple model serves as a good approximation for the double extraction spin valve.

Note that the observation $\Delta R_D > \Delta R_C$ for a parallel orientation of the magnetizations of B and C indicates an increased spin polarization induced by the cascade of two extraction events. The same relative change of the spin polarizations ($S_D^{\text{in}} > S_C^{\text{in}}$) is obtained by the transport model. This observation has implications regarding the potential application of MESVs as sources of highly spin-polarized drift currents. In the following section, application examples of multiple extraction spin valves will be discussed, in particular but not exclusively regarding their use as spin polarizers.

5.6 Application examples

Finally, examples for the use of multiple extraction spin valves in proposed devices are given. In contrast to the commonly used two-terminal spin valves, the multiple extraction scheme allows for the functional interplay of more than two ferromagnetic contacts in lateral device structures and thus enables novel types of non-volatile magneto-logic or magnetic memory applications.

5.6.1 Multiple extraction spin valves as spin polarizers

The model described in section 5.5 has implications concerning devices which rely on multiple spin extraction. In the case of the double extraction spin valve of Ta-

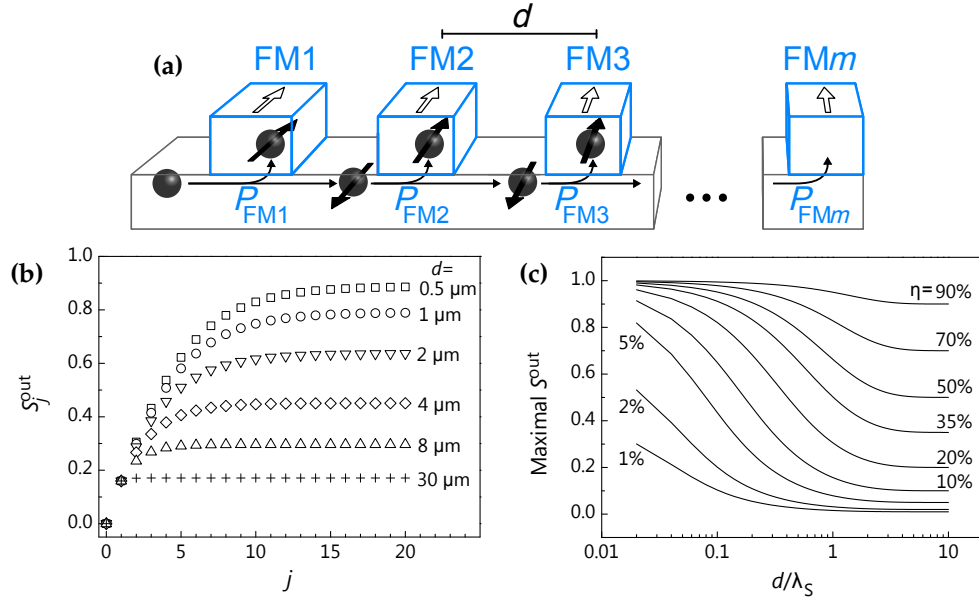


Figure 5.14: (a) Schematic of a generalized MESV with an all-parallel magnetization configuration and a uniform center-to-center contact spacing d . (b) Calculated output spin polarization S_j^{out} as a function of the FM stripe index j for different contact spacings. (c) Calculated saturation value of the MESV output spin polarization as a function of the ratio d/λ_S for different extraction efficiencies η .

ble 5.2, the model suggests that the spin polarization in the semiconducting channel can be increased by the second extraction event at contact C. This indication raises the question if the spin polarization of the conduction electrons in the channel of an MESV with an all-parallel magnetization configuration [as illustrated in Fig. 5.14(a)] can be significantly enhanced by a repeated removal of a particular spin orientation using spin extraction.

Figure 5.14(b) shows the calculated outgoing spin polarizations for an MESV consisting of 20 stripes as a function of the stripe number ($j = 0$ represents the incoming unpolarized electron current) assuming different spacings between the contacts d . The sample parameters, which resulted in a good agreement with the experiment for the DESV ($\eta = 16\%$, $\lambda_S = 11 \mu\text{m}$), are used for a parallel magnetization configuration. According to the model, it is evident that multiple spin extraction can indeed serve as a tool for the generation of an electron current with a spin polarization which considerably exceeds the extraction efficiency. However,

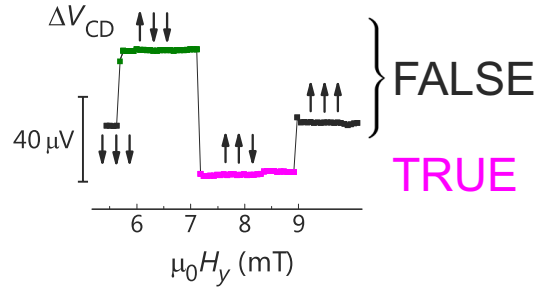


Figure 5.15: Visualization of the definition of the threshold voltage for the operation of the DESV as a binary magneto-logic gate. The upper three voltage levels correspond to a logical false value, while the lowest output voltage corresponds to true.

local detection of the generated spin polarization in the way depicted above could impose challenges on the measurement sensitivity in terms of an acceptable signal-to-noise ratio, because the usage of an increased number of output leads results in a decrease in current per contact and thus reduces the magnitude of the spin signal. Nevertheless, high degrees of spin polarization inside the semiconductor with values close to 0.89 after about 20 extraction events for a contact spacing of $0.5 \mu m$ are calculated.

The saturation polarization of such a spin extraction device is determined by the extraction efficiency and the ratio d/λ_S as shown in Fig. 5.14(c). Note that even for relatively moderate extraction efficiencies highly spin-polarized currents can be generated if the contact spacing is small with respect to the spin drift length. In fact, for a substantial enhancement of the spin polarization, spin relaxation requires the entire device size (from the first to the last ferromagnetic contact) to fall within a few spin drift lengths. Interestingly, for a given device the output spin polarization at the last stripe can be varied in sign and magnitude by using a magnetization configuration which differs from the completely parallel state.

5.6.2 Multiple spin extraction for magneto-logic gates

Generally, in an MESV non-volatile input magnetization states are used to control an output voltage or current, which can be measured in each of the output leads. For m ferromagnetic electrodes as binary inputs, one obtains 2^{m-1} output states.

Table 5.3: Exemplary magneto-logic operation of a double extraction spin valve. The magnetizations of B and C are regarded as inputs, while the magnetization state of D is used to program the logic functions NOR and AND.

In:	In:	Program:			In:	In:	Program:		
B	C	D	Out		B	C	D	Out	
↓	↓	↑	1	} NOR	↑	↑	↓	1	} AND
↑	↑	↑	0		↓	↓	↓	0	
↑	↓	↑	0		↓	↑	↓	0	
↓	↑	↑	0		↑	↓	↓	0	

Consequently, the concept of multiple spin extraction and detection opens up the possibility for multi-level logic functionality.

In particular, the described double extraction spin valve of Fig. 5.8 can be operated as a reconfigurable magneto-logic gate. In an exemplary approach, the multi-level output that was shown in Fig. 5.8(c) is reduced to a binary output by the assignment of the logical output value '1' or true to the lowest voltage level (magenta state) and the combination of all other voltage states into the logical output '0' or false as depicted in Fig. 5.15. Then, by associating the magnetizations of contacts B and C with binary inputs, the magnetization state of D can be used to program the gate to perform the logical operations NOR and AND. A corresponding logic truth table is given in Table 5.3. Several other logic functions can be realized by the double extraction spin valve in this way.

Note that logical cascading would demand the conversion of an electrical output signal to a magnetic input of a subsequent gate. Although conversion schemes from current to magnetization direction exist – such as switching by spin-transfer torque or switching by the magnetic field of a current carrying wire according to Ampère's law – it is fair to say that the comparably weak output signal limits the suitability of the scheme for practical computation.

5.6.3 Multiple extraction spin valves for memory read-out

Another potential application of the MESV is the read-out of magnetic data. The magnetization directions of the ferromagnetic electrodes can be regarded as an array of stored information. Since the electrical output state of an MESV reflects the magnetization configuration of the entire system, an array of magnetic bits can be read by performing only one measurement. This concept might allow for a comparably simple cell architecture and circuit design compared to conventional magnetoresistive random access memory (MRAM), where the read-out of individual cells demands a highly sophisticated cell architecture with the need for a stack of at least two magnetic layers per bit for magnetoresistance read-out and a transistor for the access of individual cells. Such as in conventional MRAM, writing of data in an MESV-based memory could be achieved using spin-transfer torque switching or an array of crossing word lines.

As for magneto-logic gates based on multiple spin extraction, it should be taken into consideration that an increased number of output electrodes results in a reduced spin signal in one particular contact. Hence, a scaled-up device with a large number of logical inputs/magnetic bits may impose challenges on the sensitivity of the detection. Furthermore, it should be considered that the symmetrically equivalent magnetization configurations share a common output level. Therefore, the unique assignment of an electrical output level to its corresponding magnetization configuration requires the knowledge of one input magnetization.

It is important to point out that while the spin polarizer demands that the entire array of FM contacts does not exceed the spin relaxation length for high efficiency, the described memory read-out relies on spin transport between neighboring contacts. Therefore, a scaling of the device to more ferromagnetic contacts should not degrade the device performance due to spin relaxation as long as a spacing of neighboring contacts within spin relaxation length is ensured.

5.7 Outlook

The results of this chapter can be regarded as a proof of principle of the extraction spin valve scheme and its extension to multiple extraction devices. Possible further experiments include all strategies which are suited to improve the magnitude

of the signals and the operating temperature range. As explained earlier, the most important system parameters that can be tuned are the extraction efficiency of the FM/SC interface, the spin relaxation length of the semiconductor, and the dimensions of the device. The operation temperature is inherently limited by the Curie temperature of the ferromagnetic metal, which drastically exceeds room temperature in the case of Co_2FeSi . However, the spin relaxation rate in semiconducting channels is known to increase with higher temperatures.²²

Note that the ESV scheme is generally applicable for any material combination as long as the channel and the contacts are conductive and the contacts are ferromagnetic. Thus, in addition to semiconductors, a wide range of materials – e.g., metals or low-dimensional systems such as graphene as the material of the non-magnetic channel – can be chosen to tune the material properties.

In addition, note that there has been some controversy about the prospect of the usage of the MESV as a spin polarizer. In fact, while the findings presented in section 5.5.2 indicate a slight enhancement of the spin polarization in the semiconductor by the second extraction event, further experiments on MESVs containing a larger number of stripes are needed to verify this prospect. However, in the all-electrical detection scheme described above, the spin polarizations are inferred indirectly from electrical measurements in conjunction with the spin transport model. To achieve a more direct insight into the spin density distributions, spatially resolved spin imaging can be a very useful tool. Available methods include the visualization of the out-of-plane spin component using scanning Kerr microscopy with the laser beam incident perpendicular to the sample plane. This technique requires spin precession in a perpendicular magnetic field to deduce in-plane polarizations, as described for example in Refs. 23 and 27. Another approach directly images the in-plane spin component also using the polar magneto-optical Kerr effect but on a cleaved edge of the sample.²⁸

Furthermore, while the model in section 5.5 describes the experimental results well, the assumptions made are rather crude. In particular, the efficiency of spin generation at a particular circuit node is intuitively expected to depend on the magnitude of the current which flows into the contact. If, for example, the resistance of a particular contact is very large so that no current flows into it, there will be no spin extraction and thus no generation of a spin accumulation. In the model,

5.7 Outlook

this behavior is described in terms of an empirical extraction efficiency, which contains the dependencies on all relevant parameters such as currents or local fields. However, the assumption of the same efficiency value for all contacts then potentially represents a simplification. For a more accurate description, a better model has to be developed to overcome the mentioned limitations.

CHAPTER 6

Conclusions and outlook

In this thesis, the electrical spin injection and extraction from ferromagnetic metals into n -type GaAs using lateral spin transport structures are studied. As an important result, the efficiency of spin generation from the ferromagnetic alloys Fe_3Si and Co_2Fe depends on the interface voltage, which is applied to the contact. In particular, the effective injection efficiency for Fe_3Si contacts decreases rapidly for increasing reverse bias as observed in non-local spin valve measurements. Furthermore, the employed Schottky tunnel contacts are strongly rectifying so that they demand high interface voltages for an appreciable current flow in the reverse direction as seen from the current-voltage characteristics. The combination of these two effects – a low injection efficiency at increased interface voltages and rectifying current-voltage curves – leads to adverse operational conditions for spin transport devices relying on spin injection. This behavior is explicitly demonstrated for the local spin valve, which operates only in a low-current regime. Similarly, the described problem can lead to inaccuracies when comparing the spin injection efficiencies deduced from electroluminescence polarization measurements of spin light-emitting diodes. In particular, the spin injection efficiency previously reported for Fe_3Si contacts to GaAs likely constitutes an underestimate of the true low-bias efficiency. These results emphasize the importance of the current-voltage characteristics when contacts for the efficient electrical spin generation are engi-

Chapter 6 Conclusions and outlook

neered.

As another result of this work, the realization and investigation of a novel spintronic device is presented using the Heusler alloy Co_2FeSi as the ferromagnetic contact material. It is shown experimentally that this extraction spin valve can be extended to two extraction events and that its behavior can be understood using a straight forward model of spin transport in the device. The extraction spin valve, especially in the form of the extended device comprising multiple extraction events, exhibits intriguing properties, which can potentially be used for multi-level logic devices. Furthermore, the multiple extraction scheme is potentially interesting for the read-out of a magnetic memory.

Lastly, a brief outlook for possible future work is given beyond the scope of the suggestions presented in sections 4.8 and 5.7, which are directly related to the results described in the corresponding chapters. The local spin valve geometry shares key challenges with a proposed spin-based transistor,^{15,31} i.e., both devices necessitate the electrical generation of a spin-polarized drift current, its transport, and its local detection. Albeit at low temperatures and with a small efficiency, these processes are shown experimentally in this work. Consequently, the main focus for future work can lie on the operation at room temperature and on an increase in the spin generation and detection efficiencies. In addition, for transistor operation, the challenge of manipulating the spin polarization during transport between the ferromagnetic contacts remains.

For practical purposes, it is of particular importance that the spin orientation in the semiconductor can be controlled without the need for external magnetic fields. As part of this work, spin manipulation via the Hanle effect using external magnetic fields is described. A similar but more practical approach would use spin precession in electrically controlled local magnetic fields that are induced using micro-coils¹⁵⁷ deposited on the spin transport channel. Alternatively, electrically controllable magnetic stray fields from ferromagnetic regions close to the channel have the potential to allow for a polarization reversal. Another frequently discussed approach¹⁵ makes use of the Rashba effect, where the spin-orbit coupling in the semiconductor enables the induction of a spin precession by application of a gate voltage.

Regarding the desired operation at non-cryogenic temperatures, note that room

temperature spin injection and detection has been reported for GaAs,^{17,18,102,103,158} Si,^{19,49,50,159} and Ge.⁵² With a further improvement of the room temperature operation as a goal, research aiming at the optimization of the spin injection efficiency at low temperatures constitutes a promising starting point. On the one hand, this strategy relates to the optimization of the electrical contact resistances as explained in detail in this work. On the other hand, further approaches include tailoring the spin-dependent band structure of the ferromagnetic metal¹⁵⁶ as well as using the spin filtering properties of tunneling oxides such as MgO.¹⁶⁰

All in all, the possibilities for using the spin of the electron in micro and nano-structured materials are versatile and remain an intriguing challenge for both basic and applied research in the future.

Bibliography

- ¹ G. E. Moore, Cramming more components onto integrated circuits, *Electronics* **38**, 114–117 (1965).
- ² G. E. Moore, Lithography and the future of Moore’s law, *In SPIE Proceedings, Advances in Resist Technology and Processing XII*, volume 2438, pages 2–17 (1995).
- ³ E. Vogel, Technology and metrology of new electronic materials and devices, *Nature nanotechnology* **2**, 25–32 (2007).
- ⁴ ITRS, The international technology roadmap for semiconductors: 2013, <http://www.itrs.net/Links/2013ITRS/Summary2013.htm>, web, accessed: 2014-11-12.
- ⁵ V. Zhirnov, R. Cavin, J. Hutchby, and G. Bourianoff, Limits to binary logic switch scaling—a gedanken model, *Proceedings of the IEEE* **9**, 1934–1939 (2003).
- ⁶ D. Hisamoto, W.-C. Lee, J. Kedzierski, H. Takeuchi, K. Asano, C. Kuo, E. Anderson, T.-J. King, J. Bokor, and C. Hu, FinFET—a self-aligned double-gate MOSFET scalable to 20 nm, *IEEE Transactions on Electron Devices* **47**, 2320–2325 (2000).
- ⁷ M. N. Baibich, J. M. Broto, A. Fert, F. N. Van Dau, F. Petroff, P. Etienne, G. Creuzet, A. Friederich, and J. Chazelas, Giant Magnetoresistance of

Bibliography

- (001)Fe/(001)Cr Magnetic Superlattices, *Physical Review Letters* **61**, 2472–2475 (1988).
- ⁸ G. Binasch, P. Grünberg, F. Saurenbach, and W. Zinn, Enhanced magnetoresistance in layered magnetic structures with antiferromagnetic interlayer exchange, *Physical Review B* **39**, 4828–4830 (1989).
- ⁹ Nobel Media AB, The nobel prize in physics 2007 – advanced information, http://www.nobelprize.org/nobel_prizes/physics/laureates/2007/advanced.html, web, accessed: 2014-11-12.
- ¹⁰ S. S. P. Parkin, N. More, and K. P. Roche, Oscillations in exchange coupling and magnetoresistance in metallic superlattice structures: Co/Ru, Co/Cr, and Fe/Cr, *Physical Review Letters* **64**, 2304–2307 (1990).
- ¹¹ J. H. Williams, NEWS FROM EPS/1997 Hewlett-Packard Europhysics Prize, *Physikalische Blätter* **53**, 607–610 (1997).
- ¹² J. S. Moodera, L. R. Kinder, T. M. Wong, and R. Meservey, Large magnetoresistance at room temperature in ferromagnetic thin film tunnel junctions, *Physical Review Letters* **74**, 3273–3276 (1995).
- ¹³ T. Miyazaki and N. Tezuka, Giant magnetic tunneling effect in Fe/Al₂O₃/Fe junction, *Journal of Magnetism and Magnetic Materials* **139**, L231–L234 (1995).
- ¹⁴ C. Chappert, A. Fert, and F. N. Van Dau, The emergence of spin electronics in data storage, *Nature materials* **6**, 813–823 (2007).
- ¹⁵ S. Datta and B. Das, Electronic analog of the electro-optic modulator, *Applied Physics Letters* **56**, 665–667 (1990).
- ¹⁶ J. Fabian, A. Matos-Abiague, C. Ertler, P. Stano, and I. Žutić, Semiconductor spintronics, *Acta Physica Slovaca* **57**, 565–907 (2007).
- ¹⁷ H. Zhu, M. Ramsteiner, H. Kostial, M. Wassermeier, H.-P. Schönherr, and K. Ploog, Room-Temperature Spin Injection from Fe into GaAs, *Physical Review Letters* **87**, 016601 (2001).

- ¹⁸ X. Jiang, R. Wang, R. Shelby, R. Macfarlane, S. Bank, J. Harris, and S. Parkin, Highly Spin-Polarized Room-Temperature Tunnel Injector for Semiconductor Spintronics using MgO(100), *Physical Review Letters* **94**, 056601 (2005).
- ¹⁹ S. P. Dash, S. Sharma, R. S. Patel, M. P. de Jong, and R. Jansen, Electrical creation of spin polarization in silicon at room temperature, *Nature* **462**, 491–494 (2009).
- ²⁰ Y. Zhou, W. Han, L.-T. Chang, F. Xiu, M. Wang, M. Oehme, I. A. Fischer, J. Schulze, R. K. Kawakami, and K. L. Wang, Electrical spin injection and transport in germanium, *Physical Review B* **84**, 125323 (2011).
- ²¹ S. Bandyopadhyay and M. Cahay, Electron spin for classical information processing: a brief survey of spin-based logic devices, gates and circuits, *Nanotechnology* **20**, 412001 (2009).
- ²² J. M. Kikkawa and D. D. Awschalom, Resonant Spin Amplification in *n*-Type GaAs, *Physical Review Letters* **80**, 4313–4316 (1998).
- ²³ S. A. Crooker, M. Furis, X. Lou, C. Adelmann, D. L. Smith, C. J. Palmström, and P. A. Crowell, Imaging spin transport in lateral ferromagnet/semiconductor structures, *Science* **309**, 2191–2195 (2005).
- ²⁴ R. Fiederling, M. Keim, G. Reuscher, W. Ossau, G. Schmidt, A. Waag, and L. W. Molenkamp, Injection and detection of a spin-polarized current in a light-emitting diode, *Nature* **402**, 787–790 (1999).
- ²⁵ Y. Ohno, D. K. Young, B. Beschoten, F. Matsukura, H. Ohno, and D. D. Awschalom, Electrical spin injection in a ferromagnetic semiconductor heterostructure, *Nature* **402**, 790–792 (1999).
- ²⁶ B. Jonker, Y. Park, B. Bennett, H. Cheong, G. Kioseoglou, and A. Petrou, Robust electrical spin injection into a semiconductor heterostructure, *Physical Review B* **62**, 8180–8183 (2000).
- ²⁷ Y. K. Kato, R. C. Myers, A. C. Gossard, and D. D. Awschalom, Observation of the spin Hall effect in semiconductors, *Science* **306**, 1910–1913 (2004).

Bibliography

- ²⁸ P. Kotissek, M. Bailleul, M. Sperl, A. Spitzer, D. Schuh, W. Wegscheider, C. H. Back, and G. Bayreuther, Cross-sectional imaging of spin injection into a semiconductor, *Nature Physics* **3**, 872–877 (2007).
- ²⁹ R. Farshchi, M. Ramsteiner, J. Herfort, A. Tahraoui, and H. T. Grahn, Optical communication of spin information between light emitting diodes, *Applied Physics Letters* **98**, 162508 (2011).
- ³⁰ M. Holub, J. Shin, D. Saha, and P. Bhattacharya, Electrical Spin Injection and Threshold Reduction in a Semiconductor Laser, *Physical Review Letters* **98**, 146603 (2007).
- ³¹ I. Žutić, J. Fabian, and S. Das Sarma, Spintronics: Fundamentals and applications, *Reviews of Modern Physics* **76**, 323–410 (2004).
- ³² A. Fert, J.-M. George, H. Jaffrès, and R. Mattana, Semiconductors Between Spin-Polarized Sources and Drains, *IEEE Transactions on Electron Devices* **54**, 921–932 (2007).
- ³³ A. Fert and H. Jaffrès, Conditions for efficient spin injection from a ferromagnetic metal into a semiconductor, *Physical Review B* **64**, 184420 (2001).
- ³⁴ G. Schmidt, D. Ferrand, L. Molenkamp, A. Filip, and B. van Wees, Fundamental obstacle for electrical spin injection from a ferromagnetic metal into a diffusive semiconductor, *Physical Review B* **62**, R4790–R4793 (2000).
- ³⁵ G. Schmidt and L. W. Molenkamp, Spin injection into semiconductors, physics and experiments, *Semiconductor Science and Technology* **17**, 310–321 (2002).
- ³⁶ R. Jansen, S. P. Dash, S. Sharma, and B. C. Min, Silicon spintronics with ferromagnetic tunnel devices, *Semiconductor Science and Technology* **27**, 083001 (2012).
- ³⁷ A. Baca, F. Ren, J. Zolper, R. Briggs, and S. Pearton, A survey of ohmic contacts to III-V compound semiconductors, *Thin Solid Films* **308-309**, 599–606 (1997).
- ³⁸ H. Jaffrès and A. Fert, Spin injection from a ferromagnetic metal into a semiconductor, *Journal of Applied Physics* **91**, 8111 (2002).

- ³⁹ E. I. Rashba, Theory of electrical spin injection: Tunnel contacts as a solution of the conductivity mismatch problem, *Physical Review B* **62**, R16267–R16270 (2000).
- ⁴⁰ R. Jansen, The spin-valve transistor: a review and outlook, *Journal of Physics D: Applied Physics* **36**, R289 (2003).
- ⁴¹ A. T. Hanbicki, B. T. Jonker, G. Itskos, G. Kioseoglou, and A. Petrou, Efficient electrical spin injection from a magnetic metal/tunnel barrier contact into a semiconductor, *Applied Physics Letters* **80**, 1240 (2002).
- ⁴² P. van Dorpe, V. F. Motsnyi, M. Nijboer, E. Goovaerts, V. I. Safarov, J. Das, W. van Roy, G. Borghs, and J. de Boeck, Highly Efficient Room Temperature Spin Injection in a Metal-Insulator-Semiconductor Light-Emitting Diode, *Japanese Journal of Applied Physics* **42**, L502–L504 (2003).
- ⁴³ M. Kohda, Y. Ohno, K. Takamura, F. Matsukura, and H. Ohno, A spin esaki diode, *Japanese Journal of Applied Physics* **40**, L1274 (2001).
- ⁴⁴ I. Appelbaum, B. Huang, and D. J. Monsma, Electronic measurement and control of spin transport in silicon, *Nature* **447**, 295–298 (2007).
- ⁴⁵ R. Dzhioev, K. Kavokin, V. Korenev, M. Lazarev, B. Meltser, M. Stepanova, B. Zakharchenya, D. Gammon, and D. Katzer, Low-temperature spin relaxation in *n*-type GaAs, *Physical Review B* **66**, 245204 (2002).
- ⁴⁶ X. Lou, C. Adelmann, M. Furis, S. Crooker, C. Palmstrøm, and P. Crowell, Electrical Detection of Spin Accumulation at a Ferromagnet-Semiconductor Interface, *Physical Review Letters* **96**, 176603 (2006).
- ⁴⁷ M. Tran, H. Jaffrès, C. Deranlot, J.-M. George, A. Fert, A. Miard, and A. Lemaître, Enhancement of the Spin Accumulation at the Interface between a Spin-Polarized Tunnel Junction and a Semiconductor, *Physical Review Letters* **102**, 036601 (2009).
- ⁴⁸ T. Saito, N. Tezuka, and S. Sugimoto, Temperature and Bias Voltage Dependencies of Spin Injection Signals for $\text{Co}_2\text{FeAl}_{0.5}\text{Si}_{0.5}/n\text{-GaAs}$ Schottky Tunnel Junction, *Materials Transactions* **53**, 641–644 (2012).

Bibliography

- ⁴⁹ C. H. Li, O. M. J. van 't Erve, and B. T. Jonker, Electrical injection and detection of spin accumulation in silicon at 500 K with magnetic metal/silicon dioxide contacts, *Nature Communications* **2**, 245 (2011).
- ⁵⁰ K.-R. Jeon, B.-C. Min, I.-J. Shin, C.-Y. Park, H.-S. Lee, Y.-H. Jo, and S.-C. Shin, Electrical spin accumulation with improved bias voltage dependence in a crystalline CoFe/MgO/Si system, *Applied Physics Letters* **98**, 262102 (2011).
- ⁵¹ O. M. J. van 't Erve, A. L. Friedman, E. Cobas, C. H. Li, J. T. Robinson, and B. T. Jonker, Low-resistance spin injection into silicon using graphene tunnel barriers, *Nature Nanotechnology* **7**, 737–742 (2012).
- ⁵² K.-R. Jeon, B.-C. Min, Y.-H. Jo, H.-S. Lee, I.-J. Shin, C.-Y. Park, S.-Y. Park, and S.-C. Shin, Electrical spin injection and accumulation in CoFe/MgO/Ge contacts at room temperature, *Physical Review B* **84**, 165315 (2011).
- ⁵³ H. Saito, S. Watanabe, Y. Mineno, S. Sharma, R. Jansen, S. Yuasa, and K. Ando, Electrical creation of spin accumulation in *p*-type germanium, *Solid State Communications* **151**, 1159–1161 (2011).
- ⁵⁴ A. Dankert, R. S. Dulal, and S. P. Dash, Efficient spin injection into silicon and the role of the Schottky barrier, *Scientific reports* **3**, 3196 (2013).
- ⁵⁵ R. Jansen, B. C. Min, S. P. Dash, S. Sharma, G. Kioseoglou, A. T. Hanbicki, O. M. J. van 't Erve, P. E. Thompson, and B. T. Jonker, Electrical spin injection into moderately doped silicon enabled by tailored interfaces, *Physical Review B* **82**, 241305 (2010).
- ⁵⁶ P. Bruski, S. C. Erwin, M. Ramsteiner, O. Brandt, K.-J. Friedland, R. Farshchi, J. Herfort, and H. Riechert, Disorder-induced reversal of spin polarization in the Heusler alloy Co₂FeSi, *Physical Review B* **83**, 140409 (2011).
- ⁵⁷ M. Johnson and R. H. Silsbee, Interfacial charge-spin coupling: Injection and detection of spin magnetization in metals, *Physical Review Letters* **55**, 1790–1793 (1985).
- ⁵⁸ M. Johnson, Spin accumulation in gold films, *Physical Review Letters* **70**, 2142–2145 (1993).

- ⁵⁹ F. J. Jedema, A. T. Filip, and B. J. van Wees, Electrical spin injection and accumulation at room temperature in an all-metal mesoscopic spin valve, *Nature* **410**, 345–348 (2001).
- ⁶⁰ F. J. Jedema, H. B. Heersche, A. T. Filip, J. J. A. Baselmans, and B. J. van Wees, Electrical detection of spin precession in a metallic mesoscopic spin valve, *Nature* **416**, 713–716 (2002).
- ⁶¹ F. J. Jedema, M. S. Nijboer, A. T. Filip, and B. J. van Wees, Spin injection and spin accumulation in all-metal mesoscopic spin valves, *Physical Review B* **67**, 085319 (2003).
- ⁶² X. Lou, C. Adelman, S. A. Crooker, E. S. Garlid, J. Zhang, K. S. M. Reddy, S. D. Flexner, C. J. Palmstrøm, and P. A. Crowell, Electrical detection of spin transport in lateral ferromagnet–semiconductor devices, *Nature Physics* **3**, 197–202 (2007).
- ⁶³ M. Ciorga, A. Einwanger, U. Wurstbauer, D. Schuh, W. Wegscheider, and D. Weiss, Electrical spin injection and detection in lateral all-semiconductor devices, *Physical Review B* **79**, 165321 (2009).
- ⁶⁴ P. Bruski, Y. Manzke, R. Farshchi, O. Brandt, J. Herfort, and M. Ramsteiner, All-electrical spin injection and detection in the Co₂FeSi/GaAs hybrid system in the local and non-local configuration, *Applied Physics Letters* **103**, 052406 (2013).
- ⁶⁵ S. Takahashi and S. Maekawa, Spin injection and detection in magnetic nanostructures, *Physical Review B* **67**, 052409 (2003).
- ⁶⁶ K. C. Hall and M. E. Flatté, Performance of a spin-based insulated gate field effect transistor, *Applied Physics Letters* **88**, 162503 (2006).
- ⁶⁷ M. Ciorga, C. Wolf, A. Einwanger, M. Utz, D. Schuh, and D. Weiss, Local spin valve effect in lateral (Ga,Mn)As/GaAs spin Esaki diode devices, *AIP Advances* **1**, 022113 (2011).

Bibliography

- ⁶⁸ P. Chen, J. Moser, P. Kotissek, J. Sadowski, M. Zenger, D. Weiss, and W. Wegscheider, All electrical measurement of spin injection in a magnetic p - n junction diode, *Physical Review B* **74**, 241302 (2006).
- ⁶⁹ T. Sasaki, T. Suzuki, Y. Ando, H. Koike, T. Oikawa, Y. Suzuki, and M. Shiraishi, Local magnetoresistance in Fe/MgO/Si lateral spin valve at room temperature, *Applied Physics Letters* **104**, 052404 (2014).
- ⁷⁰ F. Monzon, D. Patterson, and M. Roukes, Characterization of individual nanomagnets by the local Hall effect, *Journal of Magnetism and Magnetic Materials* **195**, 19–25 (1999).
- ⁷¹ F. Monzon and M. Roukes, Spin injection and the local Hall effect in InAs quantum wells, *Journal of Magnetism and Magnetic Materials* **198-199**, 632–635 (1999).
- ⁷² C. Gould, C. Rüster, T. Jungwirth, E. Girgis, G. Schott, R. Giraud, K. Brunner, G. Schmidt, and L. Molenkamp, Tunneling Anisotropic Magnetoresistance: A Spin-Valve-Like Tunnel Magnetoresistance Using a Single Magnetic Layer, *Physical Review Letters* **93**, 117203 (2004).
- ⁷³ P. Bruski, Hybridstrukturen bestehend aus der Heusler-Legierung Co_2FeSi und GaAs-Transportkanälen für die Realisierung von lateralen Spin-Ventilen, PhD thesis, Humboldt-Universität zu Berlin (2015).
- ⁷⁴ B. Dlubak, M.-B. Martin, C. Deranlot, B. Servet, S. Xavier, R. Mattana, M. Sprinkle, C. Berger, W. A. De Heer, F. Petroff, A. Anane, P. Seneor, and A. Fert, Highly efficient spin transport in epitaxial graphene on SiC, *Nature Physics* **8**, 557–561 (2012).
- ⁷⁵ B. Jenichen, J. Herfort, U. Jahn, A. Trampert, and H. Riechert, Epitaxial $\text{Fe}_3\text{Si}/\text{Ge}/\text{Fe}_3\text{Si}$ thin film multilayers grown on GaAs(001), *Thin Solid Films* **556**, 120–124 (2014).
- ⁷⁶ J. Herfort, H.-P. Schönherr, and K. H. Ploog, Epitaxial growth of $\text{Fe}_3\text{Si}/\text{GaAs}(001)$ hybrid structures, *Applied Physics Letters* **83**, 3912 (2003).

- ⁷⁷ J. Herfort, H.-P. Schönherr, K.-J. Friedland, and K. H. Ploog, Structural and magnetic properties of epitaxial Fe₃Si/GaAs(001) hybrid structures, *Journal of Vacuum Science & Technology B: Microelectronics and Nanometer Structures* **22**, 2073 (2004).
- ⁷⁸ M. Hashimoto, J. Herfort, H.-P. Schönherr, and K. H. Ploog, Epitaxial Heusler alloy Co₂FeSi/GaAs(001) hybrid structures, *Applied Physics Letters* **87**, 102506 (2005).
- ⁷⁹ M. Hashimoto, J. Herfort, A. Trampert, H.-P. Schönherr, and K. H. Ploog, Growth temperature dependent evolution of the interface structure in Co₂FeSi/GaAs(001) hybrid structures, *Journal of Vacuum Science & Technology B: Microelectronics and Nanometer Structures* **24**, 2004 (2006).
- ⁸⁰ V. Osipov and A. Bratkovsky, Spin accumulation in degenerate semiconductors near modified Schottky contact with ferromagnets: Spin injection and extraction, *Physical Review B* **72**, 115322 (2005).
- ⁸¹ O. M. J. van 't Erve, A. T. Hanbicki, M. Holub, C. H. Li, C. Awo-Affouda, P. E. Thompson, and B. T. Jonker, Electrical injection and detection of spin-polarized carriers in silicon in a lateral transport geometry, *Applied Physics Letters* **91**, 212109 (2007).
- ⁸² Y. Ando, K. Hamaya, K. Kasahara, Y. Kishi, K. Ueda, K. Sawano, T. Sadoh, and M. Miyao, Electrical injection and detection of spin-polarized electrons in silicon through an Fe₃Si/Si Schottky tunnel barrier, *Applied Physics Letters* **94**, 182105 (2009).
- ⁸³ G. Salis, S. F. Alvarado, and A. Fuhrer, Spin-injection spectra of CoFe/GaAs contacts: Dependence on Fe concentration, interface, and annealing conditions, *Physical Review B* **84**, 041307 (2011).
- ⁸⁴ Y. Ando, K. Kasahara, K. Yamane, Y. Baba, Y. Maeda, Y. Hoshi, K. Sawano, M. Miyao, and K. Hamaya, Bias current dependence of spin accumulation signals in a silicon channel detected by a Schottky tunnel contact, *Applied Physics Letters* **99**, 012113 (2011).

Bibliography

- ⁸⁵ M. Ramsteiner, O. Brandt, T. Flissikowski, H. Grahn, M. Hashimoto, J. Herfort, and H. Kostial, $\text{Co}_2\text{FeSi}/\text{GaAs}/(\text{Al,Ga})\text{As}$ spin light-emitting diodes: Competition between spin injection and ultrafast spin alignment, *Physical Review B* **78**, 121303 (2008).
- ⁸⁶ M. Ramsteiner, H. Hao, A. Kawaharazuka, H. Zhu, M. Kästner, R. Hey, L. Däweritz, H. Grahn, and K. Ploog, Electrical spin injection from ferromagnetic MnAs metal layers into GaAs, *Physical Review B* **66**, 081304 (2002).
- ⁸⁷ A. Kawaharazuka, M. Ramsteiner, J. Herfort, H.-P. Schönherr, H. Kostial, and K. H. Ploog, Spin injection from Fe_3Si into GaAs, *Applied Physics Letters* **85**, 3492 (2004).
- ⁸⁸ D. K. Schroder, Contact resistance and schottky barriers, In *Semiconductor Material and Device Characterization*, pages 127–184, John Wiley & Sons, Inc. (2005).
- ⁸⁹ H. Berger, Models for contacts to planar devices, *Solid-State Electronics* **15**, 145–158 (1972).
- ⁹⁰ B. Jenichen, V. Kaganer, J. Herfort, D. Satapathy, H. Schönherr, W. Braun, and K. Ploog, Long-range order in thin epitaxial Fe_3Si films grown on $\text{GaAs}(001)$, *Physical Review B* **72**, 075329 (2005).
- ⁹¹ F. Padovani and R. Stratton, Field and thermionic-field emission in Schottky barriers, *Solid-State Electronics* **9**, 695–707 (1966).
- ⁹² S. Sze and K. K. Ng, Metal-semiconductor contacts, In *Physics of Semiconductor Devices*, pages 134–196, John Wiley & Sons, Inc. (2006).
- ⁹³ S. Fernández-Garrido, K. U. Ubben, J. Herfort, C. Gao, and O. Brandt, Electrical characterization of all-epitaxial $\text{Fe}/\text{GaN}(0001)$ Schottky tunnel contacts, *Applied Physics Letters* **101**, 032404 (2012).
- ⁹⁴ R. T. Tung, The physics and chemistry of the Schottky barrier height, *Applied Physics Reviews* **1**, 011304 (2014).

- ⁹⁵ C. Awo-Affouda, O. M. J. van 't Erve, G. Kioseoglou, A. T. Hanbicki, M. Holub, C. H. Li, and B. T. Jonker, Contributions to Hanle lineshapes in Fe/GaAs non-local spin valve transport, *Applied Physics Letters* **94**, 102511 (2009).
- ⁹⁶ J. Shiogai, M. Ciorga, M. Utz, D. Schuh, T. Arakawa, M. Kohda, K. Kobayashi, T. Ono, W. Wegscheider, D. Weiss, and J. Nitta, Dynamic nuclear spin polarization in an all-semiconductor spin injection device with (Ga,Mn)As/*n*-GaAs spin Esaki diode, *Applied Physics Letters* **101**, 212402 (2012).
- ⁹⁷ A. Fuhrer, S. F. Alvarado, G. Salis, and R. Allenspach, Fast electrical switching of spin injection in nonlocal spin transport devices, *Applied Physics Letters* **98**, 202104 (2011).
- ⁹⁸ Y. S. Chen, J. Huang, A. Ludwig, D. Reuter, A. D. Wieck, and G. Bacher, Manipulation of nuclear spin dynamics in *n*-GaAs using an on-chip microcoil, *Journal of Applied Physics* **109**, 016106 (2011).
- ⁹⁹ M. Chan, Q. Hu, J. Zhang, T. Kondo, C. Palmstrøm, and P. Crowell, Hyperfine interactions and spin transport in ferromagnet-semiconductor heterostructures, *Physical Review B* **80**, 161206 (2009).
- ¹⁰⁰ G. Salis, A. Fuhrer, and S. Alvarado, Signatures of dynamically polarized nuclear spins in all-electrical lateral spin transport devices, *Physical Review B* **80**, 115332 (2009).
- ¹⁰¹ S. P. Dash, S. Sharma, J. C. Le Breton, J. Peiro, H. Jaffrès, J.-M. George, A. Lemaître, and R. Jansen, Spin precession and inverted Hanle effect in a semiconductor near a finite-roughness ferromagnetic interface, *Physical Review B* **84**, 054410 (2011).
- ¹⁰² G. Salis, A. Fuhrer, R. R. Schlittler, L. Gross, and S. F. Alvarado, Temperature dependence of the nonlocal voltage in an Fe/GaAs electrical spin-injection device, *Physical Review B* **81**, 205323 (2010).
- ¹⁰³ T. Uemura, T. Akiho, M. Harada, K.-I. Matsuda, and M. Yamamoto, Non-local detection of spin-polarized electrons at room temperature in Co₅₀Fe₅₀/GaAs Schottky tunnel junctions, *Applied Physics Letters* **99**, 082108 (2011).

Bibliography

- ¹⁰⁴ M. Furis, D. L. Smith, S. A. Crooker, and J. L. Reno, Bias-dependent electron spin lifetimes in n-GaAs and the role of donor impact ionization, *Applied Physics Letters* **89**, 102102 (2006).
- ¹⁰⁵ M. Flatté and J. Byers, Spin Diffusion in Semiconductors, *Physical Review Letters* **84**, 4220–4223 (2000).
- ¹⁰⁶ J. M. Kikkawa and D. D. Awschalom, Lateral drag of spin coherence in gallium arsenide, *Nature* **397**, 139–141 (1999).
- ¹⁰⁷ H.-L. Yu, X.-M. Zhang, P.-F. Wang, H.-Q. Ni, Z.-C. Niu, and T. Lai, Measuring spin diffusion of electrons in bulk n-GaAs using circularly dichromatic absorption difference spectroscopy of spin gratings, *Applied Physics Letters* **94**, 202109 (2009).
- ¹⁰⁸ B. Endres, M. Ciorga, R. Wagner, S. Ringer, M. Utz, D. Bougeard, D. Weiss, C. H. Back, and G. Bayreuther, Nonuniform current and spin accumulation in a 1 μm thick n-GaAs channel, *Applied Physics Letters* **100**, 092405 (2012).
- ¹⁰⁹ O. Brandt, M. Ramsteiner, T. Flissikowski, J. Herfort, and H. T. Grahn, Rate-equation model of spin dynamics and polarized light emission for spin light-emitting diodes, *Physical Review B* **81**, 115302 (2010).
- ¹¹⁰ P. van Dorpe, W. van Roy, J. de Boeck, G. Borghs, P. Sankowski, P. Kacman, J. Majewski, and T. Dietl, Voltage-controlled spin injection in a (Ga,Mn)As/(Al,Ga)As Zener diode, *Physical Review B* **72**, 205322 (2005).
- ¹¹¹ T. Akiho, J. Shan, H.-X. Liu, K.-I. Matsuda, M. Yamamoto, and T. Uemura, Electrical injection of spin-polarized electrons and electrical detection of dynamic nuclear polarization using a Heusler alloy spin source, *Physical Review B* **87**, 235205 (2013).
- ¹¹² K. Olejník, J. Wunderlich, A. C. Irvine, R. P. Campion, V. P. Amin, J. Sinova, and T. Jungwirth, Detection of Electrically Modulated Inverse Spin Hall Effect in an Fe/GaAs Microdevice, *Physical Review Letters* **109**, 076601 (2012).

- ¹¹³ T. Saito, N. Tezuka, M. Matsuura, and S. Sugimoto, Four-terminal nonlocal signals in lateral spin transport devices with variously ordered $\text{Co}_2\text{FeAl}_{0.5}\text{Si}_{0.5}$ full-Heusler alloy electrodes, *Applied Physics Letters* **103**, 122401 (2013).
- ¹¹⁴ T. Saito, N. Tezuka, M. Matsuura, and S. Sugimoto, Three-Terminal Hanle Signals in Schottky Tunnel Junctions with $\text{Co}_2\text{FeAl}_{0.5}\text{Si}_{0.5}$ Full-Heusler Alloy Electrodes Deposited at Various Temperatures, *Japanese Journal of Applied Physics* **52**, 063001 (2013).
- ¹¹⁵ S. Valenzuela, D. Monsma, C. Marcus, V. Narayanamurti, and M. Tinkham, Spin Polarized Tunneling at Finite Bias, *Physical Review Letters* **94**, 196601 (2005).
- ¹¹⁶ A. Chantis, K. Belashchenko, D. Smith, E. Tsymbal, M. van Schilfgaarde, and R. Albers, Reversal of Spin Polarization in $\text{Fe}/\text{GaAs}(001)$ Driven by Resonant Surface States: First-Principles Calculations, *Physical Review Letters* **99**, 196603 (2007).
- ¹¹⁷ B. Hamad, J. Khalifeh, I. Abu Aljarayesh, C. Demangeat, H.-B. Luo, and Q.-M. Hu, The electronic structure and spin polarization of $\text{Fe}_{3-x}\text{Mn}_x\text{Si}$ and $\text{Fe}_{3-y}\text{MnSi}_y$ alloys, *Journal of Applied Physics* **107**, 093911 (2010).
- ¹¹⁸ Y. Song and H. Dery, Spin transport theory in ferromagnet/semiconductor systems with noncollinear magnetization configurations, *Physical Review B* **81**, 045321 (2010).
- ¹¹⁹ K. Hamaya, Y. Baba, G. Takemoto, K. Kasahara, S. Yamada, K. Sawano, and M. Miyao, Qualitative study of temperature-dependent spin signals in n -Ge-based lateral devices with $\text{Fe}_3\text{Si}/n^+\text{-Ge}$ Schottky-tunnel contacts, *Journal of Applied Physics* **113**, 183713 (2013).
- ¹²⁰ M. Wu, J. Jiang, and M. Weng, Spin dynamics in semiconductors, *Physics Reports* **493**, 61–236 (2010).
- ¹²¹ Y. Song and H. Dery, Spin relaxation of hot electrons in the Gamma-valley of zinc-blende semiconductors, *arXiv:0909.3124* (2009).

Bibliography

- ¹²² P. van Dorpe, W. van Roy, V. F. Motsny, G. Borghs, and J. de Boeck, Efficient electrical spin injection in GaAs: A comparison between AlO_x and Schottky injectors, *Journal of Vacuum Science & Technology A: Vacuum, Surfaces, and Films* **22**, 1862 (2004).
- ¹²³ M. Hickey, S. Holmes, T. Meng, I. Farrer, G. Jones, D. Ritchie, and M. Pepper, Strongly bias-dependent spin injection from Fe into *n*-type GaAs, *Physical Review B* **75**, 193204 (2007).
- ¹²⁴ S. Saikin, M. Shen, and M.-C. Cheng, Spin dynamics in a compound semiconductor spintronic structure with a Schottky barrier, *Journal of Physics: Condensed Matter* **18**, 1535–1544 (2006).
- ¹²⁵ L.-T. Chang, W. Han, Y. Zhou, J. Tang, I. A. Fischer, M. Oehme, J. Schulze, R. K. Kawakami, and K. L. Wang, Comparison of spin lifetimes in *n*-Ge characterized between three-terminal and four-terminal nonlocal Hanle measurements, *Semiconductor Science and Technology* **28**, 015018 (2013).
- ¹²⁶ A. Jain, L. Louahadj, J. Peiro, J. C. Le Breton, C. Vergnaud, A. Barski, C. Beigné, L. Notin, A. Marty, V. Baltz, S. Auffret, E. Augendre, H. Jaffrès, J. M. George, and M. Jamet, Electrical spin injection and detection at Al_2O_3 /*n*-type germanium interface using three terminal geometry, *Applied Physics Letters* **99**, 162102 (2011).
- ¹²⁷ A. Jain, C. Vergnaud, J. Peiro, J. C. Le Breton, E. Prestat, L. Louahadj, C. Portemont, C. Ducruet, V. Baltz, A. Marty, A. Barski, P. Bayle-Guillemaud, L. Vila, J.-P. Attané, E. Augendre, H. Jaffrès, J.-M. George, and M. Jamet, Electrical and thermal spin accumulation in germanium, *Applied Physics Letters* **101**, 022402 (2012).
- ¹²⁸ R. Jansen, A. M. Deac, H. Saito, and S. Yuasa, Injection and detection of spin in a semiconductor by tunneling via interface states, *Physical Review B* **85**, 134420 (2012).
- ¹²⁹ I. Martin, Spin-drift transport and its applications, *Physical Review B* **67**, 014421 (2003).

- ¹³⁰ M. Furis, D. L. Smith, S. Kos, E. S. Garlid, K. S. M. Reddy, C. J. Palmstrøm, P. A. Crowell, and S. A. Crooker, Local Hanle-effect studies of spin drift and diffusion in n:GaAs epilayers and spin-transport devices, *New Journal of Physics* **9**, 347 (2007).
- ¹³¹ B. Endres, F. Hoffmann, C. Wolf, A. Einwanger, M. Utz, D. Schuh, G. Woltersdorf, M. Ciorga, D. Weiss, C. H. Back, and G. Bayreuther, Bias dependence of spin injection into GaAs from Fe, FeCo, and (Ga,Mn)As contacts, *Journal of Applied Physics* **109**, 07C505 (2011).
- ¹³² Q. O. Hu, E. S. Garlid, P. A. Crowell, and C. J. Palmstrøm, Spin accumulation near Fe/GaAs (001) interfaces: The role of semiconductor band structure, *Physical Review B* **84**, 085306 (2011).
- ¹³³ Y. Ando, K. Kasahara, S. Yamada, Y. Maeda, K. Masaki, Y. Hoshi, K. Sawano, M. Miyao, and K. Hamaya, Temperature evolution of spin accumulation detected electrically in a nondegenerated silicon channel, *Physical Review B* **85**, 035320 (2012).
- ¹³⁴ M. Ramsteiner, Spin injection from epitaxial ferromagnetic films into GaAs, *Microelectronic Engineering* **63**, 3–9 (2002).
- ¹³⁵ S. Wurmehl, G. Fecher, H. Kandpal, V. Ksenofontov, C. Felser, H.-J. Lin, and J. Morais, Geometric, electronic, and magnetic structure of Co₂FeSi: Curie temperature and magnetic moment measurements and calculations, *Physical Review B* **72**, 184434 (2005).
- ¹³⁶ R. J. Soulen, J. M. Byers, M. S. Osofsky, B. Nadgorny, T. Ambrose, S. F. Cheng, P. R. Broussard, C. T. Tanaka, J. Nowak, J. S. Moodera, A. Barry, and J. M. D. Coey, Measuring the spin polarization of a metal with a superconducting point contact, *Science* **282**, 85–88 (1998).
- ¹³⁷ R. Panguluri, G. Tsoi, B. Nadgorny, S. Chun, N. Samarth, and I. Mazin, Point contact spin spectroscopy of ferromagnetic MnAs epitaxial films, *Physical Review B* **68**, 201307 (2003).
- ¹³⁸ A. Ionescu, C. Vaz, T. Trypiniotis, C. Gürtler, H. García-Miquel, J. Bland, M. Vickers, R. Dalgliesh, S. Langridge, Y. Bugoslavsky, Y. Miyoshi, L. Cohen,

Bibliography

- and K. Ziebeck, Structural, magnetic, electronic, and spin transport properties of epitaxial Fe₃Si/GaAs(001), *Physical Review B* **71**, 094401 (2005).
- ¹³⁹ P. Bruski, private communication.
- ¹⁴⁰ M. Ogawa and T. Baba, Heavily Si-Doped GaAs and AlAs/n-GaAs Superlattice Grown by Molecular Beam Epitaxy, *Japanese Journal of Applied Physics* **24**, L572–L574 (1985).
- ¹⁴¹ J. P. Silveira and F. Briones, Low temperature growth of highly doped GaAs:Si by atomic layer molecular beam epitaxy, *Applied Physics Letters* **65**, 573 (1994).
- ¹⁴² B.-C. Min, K. Motohashi, C. Lodder, and R. Jansen, Tunable spin-tunnel contacts to silicon using low-work-function ferromagnets, *Nature materials* **5**, 817–822 (2006).
- ¹⁴³ Y. Manzke, R. Farshchi, P. Bruski, J. Herfort, and M. Ramsteiner, Nonvolatile reconfigurable current divider based on spin extraction in lateral ferromagnet/nonmagnet transport structures, *Physical Review B* **87**, 134415 (2013).
- ¹⁴⁴ Y. Manzke, R. Farshchi, P. Bruski, J. Herfort, and M. Ramsteiner, Multiple Extraction Spin Valves for Spintronic Circuits, *IEEE Transactions on Magnetics* **49**, 4367–4370 (2013).
- ¹⁴⁵ M. Ramsteiner, Y. Manzke, P. Bruski, R. Farshchi, and J. Herfort, Nonlocal, local, and extraction spin valves based on ferromagnet/semiconductor hybrid structures consisting of the Heusler alloy Co₂FeSi on GaAs, In H.-J. Drouhin, J.-E. Wegrowe, and M. Razeghi, editors, *SPIE Proceedings*, volume 8813, page 88130R (2013).
- ¹⁴⁶ C. Ciuti, J. McGuire, and L. Sham, Spin Polarization of Semiconductor Carriers by Reflection off a Ferromagnet, *Physical Review Letters* **89**, 156601 (2002).
- ¹⁴⁷ R. K. Kawakami, K. McCreary, and Y. Li, Fundamentals of Spintronics in Metal and Semiconductor Systems, In A. Korkin and F. Rosei, editors, *Nanoelectronics and Photonics: From Atoms to Materials, Devices, and Architectures*, chapter 5, pages 59–114, Springer, New York (2008).

- ¹⁴⁸ H. Dery and L. Sham, Spin Extraction Theory and Its Relevance to Spintronics, *Physical Review Letters* **98**, 046602 (2007).
- ¹⁴⁹ T. Hentschel, B. Jenichen, A. Trampert, and J. Herfort, Ferromagnetic Heusler alloy Co_2FeSi films on GaAs(110) grown by molecular beam epitaxy, *Journal of Physics D: Applied Physics* **45**, 055002 (2012).
- ¹⁵⁰ M. Hashimoto, A. Trampert, J. Herfort, and K. H. Ploog, Atomic ordering and interlayer diffusion of Co_2FeSi films grown on GaAs(001) studied by transmission electron microscopy, *Journal of Vacuum Science & Technology B: Microelectronics and Nanometer Structures* **25**, 1453 (2007).
- ¹⁵¹ P. Bruski, K.-J. Friedland, R. Farshchi, J. Herfort, and M. Ramsteiner, Spatial distribution of structural disorder in Co_2FeSi films studied by anisotropic magnetoresistance, *Solid State Communications* **152**, 1131–1134 (2012).
- ¹⁵² B. Jenichen, J. Herfort, K. Kumakura, and A. Trampert, Long-range order and thermal stability of thin Co_2FeSi films on GaAs(111)B, *Journal of Physics D: Applied Physics* **43**, 285404 (2010).
- ¹⁵³ B. Jenichen, J. Herfort, T. Hentschel, A. Nikulin, X. Kong, A. Trampert, and I. Žižak, Residual disorder and diffusion in thin Heusler alloy films, *Physical Review B* **86**, 075319 (2012).
- ¹⁵⁴ B. Jenichen, T. Hentschel, J. Herfort, X. Kong, A. Trampert, and I. Žižak, Characterization of $L2_1$ order in Co_2FeSi thin films on GaAs, *Journal of Physics: Conference Series* **471**, 012022 (2013).
- ¹⁵⁵ R. Farshchi, P. Bruski, M. Ramsteiner, J. Herfort, O. Brandt, Y. Manzke, K.-J. Friedland, and H. Grahn, Multi-channel magnetotransport in $\text{Co}_2\text{FeSi}/(\text{Al,Ga})\text{As}$ spin-LEDs, *Solid State Communications* **151**, 436–439 (2011).
- ¹⁵⁶ R. Farshchi and M. Ramsteiner, Spin injection from Heusler alloys into semiconductors: A materials perspective, *Journal of Applied Physics* **113**, 191101 (2013).

Bibliography

- ¹⁵⁷ J. Kim, J. Puls, Y. S. Chen, G. Bacher, and F. Henneberger, Electron-nuclear spin control in charged semiconductor quantum dots by electrical currents through micro-coils, *Applied Physics Letters* **96**, 151908 (2010).
- ¹⁵⁸ T. Manago and H. Akinaga, Spin-polarized light-emitting diode using metal/insulator/semiconductor structures, *Applied Physics Letters* **81**, 694 (2002).
- ¹⁵⁹ T. Suzuki, T. Sasaki, T. Oikawa, M. Shiraishi, Y. Suzuki, and K. Noguchi, Room-Temperature Electron Spin Transport in a Highly Doped Si Channel, *Applied Physics Express* **4**, 023003 (2011).
- ¹⁶⁰ S. S. P. Parkin, C. Kaiser, A. Panchula, P. M. Rice, B. Hughes, M. Samant, and S.-H. Yang, Giant tunnelling magnetoresistance at room temperature with MgO (100) tunnel barriers, *Nature materials* **3**, 862–867 (2004).

List of figures

2.1	Schematic representation of the spin injection process in ferromagnetic metal/semiconductor contacts	6
2.2	Spin relaxation time as a function of the donor concentration in GaAs at low temperatures	10
2.3	Measurement geometries for spin transport measurements	13
2.4	Ferromagnetic metal/semiconductor Schottky contact and three-terminal Hanle curve	14
2.5	Spin-dependent density of states in non-local spin valve measurements	16
2.6	Magnetoresistance ratio of a ferromagnetic metal (FM)/insulator (I)/semiconductor/I/FM structure	20
3.1	Layer sequence of spin transport devices grown by molecular beam epitaxy	24
3.2	Image of a processed sample surface	25
3.3	Pieces of a processed sample and sample on a chip carrier	26
3.4	Experimental setup for spin transport measurements	27
4.1	X-ray diffraction curves for samples of chapter 4	32
4.2	Schematic diagram of a spin transport device	33

List of figures

4.3	Geometry for the measurement of current-voltage characteristics and calculated potential distribution below contact	34
4.4	Current density as a function of interface bias	36
4.5	Schematic of a forward-biased Schottky contact	37
4.6	Forward and reverse current-voltage characteristics	38
4.7	Temperature dependence of current-voltage characteristics	39
4.8	Non-local spin valve arrangement and non-local voltage as a function of magnetic field	41
4.9	Non-local voltage as a function of spin transport length	42
4.10	Non-local voltage as a function of current	43
4.11	Non-local Hanle curves	45
4.12	Schematic diagram explaining spin relaxation in an interface proximity region	47
4.13	Non-local spin valve signal as a function of interface bias	48
4.14	Current-voltage characteristics for different contact widths	51
4.15	Current and interface bias dependence of non-local spin valve signal for different contact widths	52
4.16	Non-local spin resistance as a function of interface bias for different contact widths	53
4.17	Three-terminal measurement geometry and three-terminal Hanle curve	54
4.18	Three-terminal spin signal and spin lifetime as a function of interface bias	56
4.19	Three-terminal Hanle and inverted Hanle curves	57
4.20	Specific contact resistivity as a function of current	60
4.21	Geometry of a local spin valve measurement and local resistance as a function of magnetic field	61
4.22	Calculated magnetoresistance of a local spin valve	62
4.23	Local spin valve signal as a function of current and interface voltage	63
4.24	Comparison of local spin valve signal with effective injection efficiency as a function of interface voltage	64
5.1	Optical micrograph of sample 1	72

List of figures

5.2	Extraction spin valve geometry and output current as a function of magnetic field	73
5.3	Output current of the extraction spin valve as a function of magnetic field for different output leads	74
5.4	Output current of the extraction spin valve as a function of an out-of-plane magnetic field	75
5.5	Extraction spin valve signal as a function of total current	76
5.6	Local spin valve resistance of sample 1 as a function of magnetic field and corresponding measurement geometry	78
5.7	Double extraction spin valve geometry and output current as a function of magnetic field	79
5.8	Double extraction spin valve with two current sources, output current as a function of magnetic field, and switching sequences	80
5.9	Illustration of double extraction spin valve switching sequences . .	81
5.10	Local Hanle effect measurements for determination of magnetization configurations leading to different double extraction spin valve output levels	82
5.11	Model circuit of the double extraction spin valve	83
5.12	Schematic of a multiple extraction spin valve	85
5.13	Current divider schematic for the spin transport model	86
5.14	Multiple extraction spin valve as a spin polarizer	88
5.15	Assignment of double extraction spin valve levels to binary outputs	89

List of tables

4.1	Sample parameters for chapter 4	31
5.1	Parameters of extraction spin valve devices	81
5.2	Output levels, contact resistances, and spin polarization values of the double extraction spin valve	84
5.3	Magneto-logic operation of a double extraction spin valve	90